Pacific Northwest
NATIONAL LABORATORY

PNNL-36488

Advanced Manufacturing Techniques and Compositions of High Entropy Alloys for Nuclear Applications

August 2024

Mohan Sai Kiran Kumar Yadav Nartu, Subhashish Meher, Isabella van Rooyen, David Garcia, Tianhao Wang, Jorge F Dos Santos, Shalini Tripathi, Nathan Canfield

M4CT-24PN1304053

U.S. DEPARTMENT OF ENERGY

Prepared for the U.S. Department of Energy
under Contract DE-AC05-76RL01830

DISCLAIMER

PACIFIC NORTHWEST NATIONAL LABORATORY
operated by
BATTELLE
for the
UNITED STATES DEPARTMENT OF ENERGY
under Contract DE-AC05-76RL01830

Printed in the United States of America

Available to DOE and DOE contractors from
the Office of Scientific and Technical Information,
P.O. Box 62, Oak Ridge, TN 37831-0062
www.osti.gov
ph: (865) 576-8401
fox: (865) 576-5728
email: reports@osti.gov

Available to the public from the National Technical Information Service
5301 Shawnee Rd., Alexandria, VA 22312
ph: (800) 553-NTIS (6847)
or (703) 605-6000
email: info@ntis.gov
Online ordering: http://www.ntis.gov

Advanced Manufacturing Techniques and Compositions of High Entropy Alloys for Nuclear Applications

August 2024

Mohan Sai Kiran Kumar Yadav Nartu, Subhashish Meher, Isabella van Rooyen, David Garcia, Tianhao Wang, Jorge F Dos Santos, Shalini Tripathi, Nathan Canfield

M4CT-24PN1304053

Prepared for
the U.S. Department of Energy
under Contract DE-AC05-76RL01830

Pacific Northwest National Laboratory
Richland, Washington 99354

Summary

In line with the objectives of the Department of Energy, Office of Nuclear Energy, Advanced Materials and Manufacturing Technologies (AMMT) program, this work focuses on new materials development and qualification research and development for next-generation, high-temperature nuclear reactors. While the currently qualified nuclear materials have demonstrated significant irradiation resistance at high temperatures, the community is still interested in materials that can sustain the harsh environments found in nuclear reactors for temperatures up to 1,000°C for nearly 100,000 h. High entropy alloys (HEAs) have the potential to serve in these extreme environments of next-generation nuclear reactors because of their unique phase transformation pathways and nanoscale and mesoscale microstructures. The current work focuses on understanding such nuclear-energy-relevant HEAs through a detailed literature survey, selected experimental work, and developing a decision matrix with criteria for the identification of HEAs that may have the most impact and value for further examination.

The HEA classification used in this study and the elaborate literature survey provide insights into the processing, microstructure, and properties of several reported HEAs targeting different applications. Six HEAs were identified as promising for the nuclear industry, focusing on high-temperature properties, with Co as an alloying element in two of these alloys [$(Ni_2Co_2FeCr)_{92}Al_4Nb_4$; $Al_{0.3}Ti_{0.2}Co_{0.7}CrFeNi_{1.7}$]. GRX-810 (Co-33%, Cr-29%, Re-1.5%, Al-0.3%, Ti-0.25%, Nb-0.75%, W-3%, C-0.05%, Ni-Balance), developed by the National Aeronautics and Space Administration (NASA), shows creep performance 2–3 orders of magnitude better than that of current high-temperature alloys. It is best classified as a medium entropy alloy or an oxide dispersion strengthened (ODS) alloy because of the presence of Y_2O_3 particles; therefore, we recommend pursuing this material as part of a different AMMT work package. Although the decision matrix is not yet fully developed for the six candidate HEAs, the literature survey provides technical justification to down-select two HEAs ($Al_{0.3}Ti_{0.2}Co_{0.7}CrFeNi_{1.7}$ and $Al_{10}Cr_{12}Fe_{35}Mn_{23}Ni_{20}$) for detailed experimental work. An advanced processing route was evaluated for fabricating functionally graded HEAs using directed energy deposition (DED) and off-the-shelf metal alloy powders. This advanced processing methodology for functionally graded HEAs would open avenues for rapidly assessing new HEA compositions at significantly cheaper costs.

Most of the reviewed HEA research used arc (73%) and vacuum (15%) melting processes as a fabrication method, with only 11% of the reviewed papers using laser-based additive manufacturing processes. Solid-state manufacturing processes were only reported in less than 5% of the instances. The literature survey shows the opportunity to explore solid-phase processes as a manufacturing technique because of the grain refinement and decreased segregation properties during these processes. Therefore, friction surface layer deposition (FSLD) was included for the two down-selected HEAs ($Al_{0.3}Ti_{0.2}Co_{0.7}CrFeNi_{1.7}$ and $Al_{10}Cr_{12}Fe_{35}Mn_{23}Ni_{20}$) because of its unique processing conditions that resulted in finer microstructures with compositionally homogenous grains that would potentially enhance mechanical properties. In addition, the effect of solid-phase processing on the mechanical properties of these HEAs can provide valuable information and potentially more economical routes to HEA adoption to market.

The temperature-dependent (from room temperature [RT] to 500°C) nanoindentation behavior of the DED- and selective laser melting (SLM)-processed $Al_{0.3}Ti_{0.2}Co_{0.7}CrFeNi_{1.7}$ HEA was investigated in the as-deposited (AD) and one-step annealed conditions for this study. The hierarchically heterogeneous microstructures obtained via simple one-step annealing of the

DED- and SLM-processed HEAs exhibited significantly better performance than the nearly homogeneous microstructures in the AD state. The one-step annealed specimens showed a less than 6.6% reduction in hardness at 500°C compared to that at RT, while the AD specimens showed a greater than 18% reduction in hardness between RT and 500°C. The HEAs fabricated under one-step annealed conditions also exhibited a significantly higher hardness than those under the AD conditions owing to the multiphase (FCC+$L1_2$) microstructures with a substantial fraction of ordered $L1_2$ precipitates. Furthermore, serrated yielding (Portevin–Le Chatelier [PLC] effect) indicative of microstructural instability was observed during nanoindentation deformation (at 500°C) for both SLM- and DED-processed specimens but not after one-step annealing. The nanoindentation results demonstrate the stability of these hierarchically heterogeneous microstructures developed via single-step annealing, exploiting the residual stresses in the additively manufactured $Al_{0.3}Ti_{0.2}Co_{0.7}CrFeNi_{1.7}$ HEA. Overall, the observed results are promising. However, applying this HEA in high-temperature nuclear reactors would require a more detailed assessment of other properties. This HEA is expected to have high-temperature stability up to ~1100°C.

In contrast, the FSLD processing of this HEA was challenging because of its multiphase microstructure in the as-received (AR) state. Hence, a meticulous process parameter optimization study was performed to process this HEA. Further, detailed microstructural characterization using scanning electron microscopy (SEM) was carried out to analyze the differences in the microstructure due to FSLD processing. FSLD processing led to the homogenization of this HEA, resulting in the formation of a single-phase face-centered cubic (FCC) microstructure. Despite the single-phase character, the FSLD-processed HEA exhibited a significantly high hardness of 325 HV, providing scope for further enhancement of the hardness via heat treatments and process parameter optimization.

Similar to $Al_{0.3}Ti_{0.2}Co_{0.7}CrFeNi_{1.7}$, cast rods of the $Al_{10}Cr_{12}Fe_{35}Mn_{23}Ni_{20}$ HEA procured from Sophisticated Alloys, Inc. were processed using FSLD, and FSLD processing was performed to produce single- and multilayer deposits of the $Al_{10}Cr_{12}Fe_{35}Mn_{23}Ni_{20}$ HEA. A detailed process parameter–property optimization study was performed by depositing several single layers of the HEA by varying the forging force (*F*) and traverse speed (*Tr*). Further, a multilayer deposit was successfully fabricated using the optimized processing conditions (*F* = 40 kN, Tr = 200 mm/min), demonstrating the potential for FSLD to fabricate tall specimens. A detailed microstructural evaluation of the AR and FSLD-processed specimens was carried out using SEM, electron backscatter diffraction (EBSD), energy-dispersive spectroscopy (EDS), and transmission electron microscopy (TEM). The AR specimen exhibited a coarser triple-phase FCC+BCC+B2 microstructure with a soft FCC matrix phase, a hard body-centered cubic (BCC) dendritic phase, and a harder B2 phase as precipitates within the hard BCC dendrites. All three phases pursued drastically different microstructural evolution pathways during FSLD processing. The FCC matrix underwent continuous dynamic recrystallization, forming finer equiaxed grains due to shearing deformation. At the same time, the BCC dendrites fractured into several finer fragments, and in some regions, these BCC fragments tended to grow, changing their morphology from arbitrary to hourglass-like. Among the three phases, B2 is the only phase that likely dissolved during processing and reprecipitated as finer precipitates in the BCC fragments during continuous cooling post-FSLD. In a manuscript submitted to *Additive Manufacturing*, these complex mechanisms are clearly illustrated using a schematic. The microstructure of the triple-phase HEA changed significantly with the changes in the processing conditions, providing scope for tuning the process parameters further to attain desired microstructures and mechanical properties. To conclude, in addition to the significant enhancement in the hardness (from 177 HV to 278 HV), FSLD processing led to substantially finer grains/precipitates, which increase the number of interfaces, potentially enhancing the sink

strength of the $Al_{10}Cr_{12}Fe_{35}Mn_{23}Ni_{20}$ HEA, making it an ideal candidate for future nuclear applications.

The microstructures of compositionally graded HEAs fabricated via DED using off-the-shelf common alloy powders were characterized. The results reveal homogenous compositions in each build layer. However, the graded HEAs formed dendritic and interdendritic microstructures mainly due to the presence of heavier elements such as Nb. Few regions contained unmelted 316 L powder with sparsely distributed nanoscale Cr-rich precipitates. Additionally, Ti oxide particles were observed in the HEA matrix. While the microstructural examination indicates the successful fabrication of graded materials, further investigation is needed to optimize the process parameters to reduce porosity and undesired brittle intermetallic phases and ensure complete melting of the metal alloy powders.

The collaboratively determined decision matrix is briefly discussed with preliminary ratings of the selected HEAs. However, the finalization of the ratings in the decision matrix will continue, as the full battery of experimental work is in process, which may influence the final decision based on the determined ratings. The $Al_{10}Cr_{12}Fe_{35}Mn_{23}Ni_{20}$ HEA performed marginally better than the $Al_{0.3}Ti_{0.2}Co_{0.7}CrFeNi_{1.7}$ HEA, with a rating of 63 versus 55.5.

The research performed as part of this study resulted in three conference presentations, one accepted journal publication, and two manuscripts under preparation.

Acknowledgments

The research presented here was supported by the Advanced Materials and Manufacturing Technology (AMMT) program of the U.S. Department of Energy (DOE), Office of Nuclear Energy. Pacific Northwest National Laboratory (PNNL) is a multiprogram national laboratory operated for the DOE by Battelle Memorial Institute under Contract No. DE-AC05-76RL01830. The authors would like to thank Luis Nunez and Calvin Downey from Idaho National Laboratory for fabrication of the alloys and the discussion in Section 4.3.

Acronyms and Abbreviations

AD	As-deposited
AM	Additive manufacturing
AMMT	Advanced Materials and Manufacturing Technology
APT	Atom probe tomography
AR	As-received
BCC	Body-centered cubic
BCT	Body-centered tetragonal
DED	Directed energy deposition
DOE	U.S. Department of Energy
EBAM	Electron beam additive manufacturing
EBM	Electron beam melting
EBSD	Electron backscatter diffraction
EDM	Electric discharge machine
EDS	Energy-dispersive spectroscopy
FCC	Face-centered cubic
FEG	Field emission gun
FIB	Focused ion beam
FSLD	Friction surface layer deposition
FY	Fiscal year
GB	Grain boundary
HCP	Hexagonal close-packed
HEA	High entropy alloy
HIP	Hot isostatic pressing
ICME	Integrated computational materials engineering
INL	Idaho National Laboratory
IPF	Inverse pole figure
LANL	Los Alamos National Laboratory
LDRD	Laboratory Directed Research and Development
LENS	Laser engineered net shaping
LPBF	Laser powder bed fusion
NASA	National Aeronautics and Space Administration
NRC	U.S. Nuclear Regulatory Commission
ODS	Oxide dispersion strengthened
OM	Optical microscopy
ORNL	Oak Ridge National Laboratory
PLC	Portevin–Le Chatelier

PNNL	Pacific Northwest National Laboratory
RHEA	Refractory high entropy alloy
RIP	Radiation-induced precipitation
RIS	Radiation-induced segregation
RT	Room Temperature
SC	Supercritical
SCC	Stress corrosion cracking
SEBM	Selective electron beam melting
SEM	Scanning electron microscopy
SFP	Stationary friction processing
ShAPE	shear-assisted processing and extrusion
SLM	Selective laser melting
SPS	Spark plasma sintering
SS	Stainless steel
STEM	Scanning transmission electron microscopy
TEM	Transmission electron microscopy
TRIP	Transformation induced plasticity
TRL	Technology readiness level
TWIP	Twinning induced plasticity
UTS	Ultimate tensile strength
VLM	Vacuum levitation melting
WAAM	Wire arc additive manufacturing
YS	Yield strength

Contents

Summary 2
Acknowledgments 5
Acronyms and Abbreviations 6
Contents 8
1.0 Introduction 12
1.1 Background 12
1.2 PNNL HEA Work Scope and Objectives 13
1.3 Report Content 14
2.0 Decision Criteria Matrix 15
3.0 Literature Survey of High Entropy Alloys 18
3.1 What are HEAs? 18
3.2 Current Fabrication Techniques Used for HEAs 18
3.2.1 Solid-State Processing 18
3.2.2 Conventional Liquid-State Processing 19
3.2.3 Liquid-State Additive Manufacturing 20
3.3 Classification of HEAs 20
3.4 Stable HEAs 21
3.4.1 Single-Phase HEAs 21
3.4.2 Dual-Phase HEAs 27
3.4.3 Composite HEAs (Precipitate/Dispersion Strengthened) 31
3.5 Metastable HEAs 37
3.5.1 TRIP/TWIP HEAs 37
3.6 Survey of Prior HEA Research for Nuclear Applications 40
3.7 Promising HEA Candidates for Nuclear Applications Based on All Surveyed HEAs 48
4.0 Experimental Work 50
4.1 Down-Selected HEA: $Al_{0.3}Ti_{0.2}Co_{0.7}CrFeNi_{1.7}$ 50
4.1.1 Background 50
4.1.2 Materials and Methods 51
4.1.3 Results and Discussion 52
4.1.4 Summary 64
4.2 Down-Selected HEA: $Al_{10}Cr_{12}Fe_{35}Mn_{23}Ni_{20}$ 65
4.2.1 Background and Summary of Experimental Work 65
4.3 Graded High Entropy Alloys 66
4.3.1 Background 66
4.3.2 Materials and Methods 66
4.3.3 Results and Discussion 67

4.3.4 Summary 70
5.0 Research Outcomes 71
6.0 Preliminary Decision Matrix Ratings of the Two Down-Selected HEAs 72
6.1 Justification of Ratings 73
6.1.1 $Al_{0.3}Ti_{0.2}Co_{0.7}CrFeNi_{1.7}$ 73
6.1.2 $Al_{10}Cr_{12}Fe_{35}Mn_{23}Ni_{20}$ 75
7.0 Conclusion and Recommendations 77
8.0 References 79

Figures

Figure 1. PNNL work scope including a literature survey and experimental work. 14

Figure 2. Classification of HEAs. 21

Figure 3. Low-, medium-, and high-magnification SEM backscatter images for (a–c) DED(AD) and (d–f) DED(HT or AD+800°C) specimens of the DED-processed $Al_{0.3}Ti_{0.2}Co_{0.7}CrFeNi_{1.7}$ HEA. 53

Figure 4. Low-, medium-, and high-magnification SEM backscatter images for (a–c) SLM(AD) and (d–f) SLM(HT or AD+800°C) specimens of the SLM-processed $Al_{0.3}Ti_{0.2}Co_{0.7}CrFeNi_{1.7}$ HEA. 54

Figure 5. Hardness versus temperature plots comparing (a) DED(AD) and DED(HT) specimens, (b) SLM(AD) and SLM(HT) specimens, (c) DED(AD) and SLM(AD) specimens, and (d) DED(HT) and SLM(HT) specimens of the AM-processed $Al_{0.3}Ti_{0.2}Co_{0.7}CrFeNi_{1.7}$ HEA. 56

Figure 6. Representative load versus displacement (*P*–*h*) curves as a function of temperature comparing (a) DED(AD) and DED(HT) specimens, (b) SLM(AD) and SLM(HT) specimens, (c) DED(AD) and SLM(AD) specimens, and (d) DED(HT) and SLM(HT) specimens of the $Al_{0.3}Ti_{0.2}Co_{0.7}CrFeNi_{1.7}$ HEA. 57

Figure 7. SEM backscatter images revealing $L1_2$ precipitation post-nanoindentation deformation at 500°C for (a, b) DED(AD) and (c, d) SLM(AD) specimens of the AM-processed HEA. 58

Figure 8. Phase fraction versus temperature plot for the $Al_{0.3}Ti_{0.2}Co_{0.7}CrFeNi_{1.7}$ HEA generated using Thermo-Calc software. 58

Figure 9. (a) Optical image and (b–f) SEM backscatter images revealing the microstructure of the AR $Al_{0.3}Ti_{0.2}Co_{0.7}CrFeNi_{1.7}$ HEA along the radial direction. 59

Figure 10. High-magnification SEM backscatter images obtained from (a–c) Region 1 and (d–f) Region 2 in Figure 9(a). 60

Figure 11. (a) IPF and (b) phase map obtained from an AR specimen of the $Al_{0.3}Ti_{0.2}Co_{0.7}CrFeNi_{1.7}$ HEA. 60

Figure 12. Hardness values plotted along the radial direction of the AR HEA. 61

Figure 13. Machine data for various FSLD processes for Run Numbers (a) 2024-04-25-0004, (b) 2024-04-25-0005, (c) 2024-04-25-0006, and (d) 2024-04-25-0007 61

Figure 14. Appearance of the surfaces of FSLD-processed specimens for Run Numbers (a) 2024-04-25-0004, (b) 2024-04-25-0005, (c) 2024-04-25-0006, and (d) 2024-04-25-0007. 62

Figure 15. Cross-section OM images: (a) Condition 2, (b) Condition 1, (c) Condition 3, and (d) Condition 8. 62

Figure 16. (a) Optical image of the transverse section of an FSLD-processed HEA for Condition 8. (b–e) Low- and (f–g) high-magnification SEM backscatter images obtained along the build height from the region marked in (a) 64

Figure 17. (a) Schematic of the compositionally graded HEA on a 316L substrate using DED; (b) fabricated graded material on the substrate, marked by

the yellow dashed line; (c) optical image of the graded material; (d) SEM images showing the continuous variation of Fe, Co, and Cr with deposition thickness; and (e) enlarged optical image showing the area of interest and the region marked as “5” in (c). The approximate area of the TEM lift-out has been marked in the green box. 67
Figure 18. (a) FIB lift-out showing the area of interest and the unmelted steel powder on the left side, (b) STEM image showing the same area of interest with the interface between the HEA and the unmelted steel powder particle, and (c) Co elemental map showing the interface between the two phases. The Ti map in (e) shows the Ti-rich region in the HEA region, and (f) shows the Cr-rich region in the unmelted steel powder particle. 68
Figure 19. (a) STEM image showing the morphology of the Ti oxide precipitate in the HEA region. The chemical maps of the HEA region highlight the presence of Ti and O in the form of precipitates in (b–d). 68
Figure 20. (a) STEM image showing the morphology of the Cr-rich particle in the unmelted steel. (b–d) Elemental distributions in the Cr-rich region. 69
Figure 21. (a–b) SEM and STEM images showing the dendritic and interdendritic region formation in the HEA region. (c–g) Chemical maps obtained with STEM-EDS showing the strong presence of Nb and the absence of Fe, Ni, Cr, and Co in the interdendritic regions. 69

Tables

Table 1. Decision criteria matrix. 15
Table 2. Literature review of various single-phase HEAs. 21
Table 3. Literature review of various dual-phase HEAs. 27
Table 4. Literature review of various composite HEAs. 31
Table 5. Literature review of various metastable HEAs. 37
Table 6. Literature review of various HEAs for nuclear applications. 41
Table 7. Completed experimental work. 50
Table 8. Chemical composition of the SS304 substrate and HEA feed rods. 52
Table 9. Nanoindentation hardness (in GPa) for all four conditions of AM-processed $Al_{0.3}Ti_{0.2}Co_{0.7}CrFeNi_{1.7}$ HEA. 55
Table 10. Critical parameters for the FSLD runs conducted in this study. 61
Table 11. Critical parameters for the runs conducted in this study and their related defects. 63
Table 12. Preliminary decision matrix ratings. 72

1.0 Introduction

The goals of the Advanced Materials and Manufacturing Technologies (AMMT) program are to develop cross-cutting technologies in support of a broad range of nuclear reactor technologies and to maintain U.S. leadership in materials and manufacturing technologies for nuclear energy applications. The overarching vision of the AMMT program is to accelerate the development, qualification, demonstration, and deployment of advanced materials and manufacturing technologies to enable reliable and economical nuclear energy. Through advanced manufacturing techniques, new materials can be created for many applications in nuclear reactors. These materials can further the development of advanced reactors, where properties such as improved high-temperature strength, improved corrosion resistance, or improved radiation tolerance are needed. Achieving this can provide a safety improvement through larger safety margins, an economic benefit for higher efficiency during operation, and a cost reduction through more cost-effective manufacturing processes and less waste.

1.1 Background

Recently, there has been significant effort in developing new structural materials such as bulk metallic glasses [1–4], oxide dispersion strengthened (ODS) steels [5–7], ceramics [8–12], nanolayered composites [13–17], and high entropy alloys (HEAs) [18] for next-generation nuclear reactor applications. The AMMT program initiated a multilab effort by Oak Ridge National Laboratory (ORNL) (work package CT-23OR130406), Los Alamos National Laboratory (LANL) (work package CT-23LA130403), and Pacific Northwest National Laboratory (PNNL) (work package CT-23PN130408) to evaluate and focus on advanced manufacturing techniques applied for new material development of ODS nuclear materials, refractory composites and alloys, and HEAs, respectively. By performing this work, an opportunity is created to explore recent advances in these material groups, due to the promise of high-temperature performance, corrosion, and irradiation tolerance. In addition to specific microstructural challenges for each material group, the need for upscaled manufacturing techniques is still one of the biggest hurdles in advancing the technology readiness level (TRL) of these material groups. The execution of this multilab research effort will provide the AMMT program with a merit-based feasibility study identifying an accelerated development path for these materials. This merit-based decision matrix was developed through collaboration between ORNL, LANL, and PNNL. A comparison between these three material types was made and collaboratively reported in the September 2023 M2 milestone (Preliminary feasibility studies of new materials for advanced manufacturing) led by ORNL.

Structural materials need to sustain against creep and void swelling and exhibit a reasonably high mechanical strength and fracture toughness under irradiation at high temperatures (>300°C). There are commonly three main strategies for improving the radiation tolerance in materials: (a) designing radiation-resistant matrix phases, (b) immobilizing the vacancies and interstitials, and (c) enhancing the sink strength of the material [19]. Among the new materials, HEAs have been shown to address all three design strategies [1] and thus form an integral part of the advanced materials development portfolio and provide a reason for further exploration under the current work package.

HEAs with a significantly higher configurational entropy than those of conventional alloys exhibit unusual lattice distortion and sluggish diffusion, which could potentially immobilize the radiation-induced defects and result in undesired swelling and segregation; this is detrimental to

mechanical and functional properties [2–10]. The high levels of transmutation in conventional alloys may already produce compositionally complex alloys locally resembling HEAs [1,11,12].

While strategies (a) and (b) mentioned previously can only augment the radiation resistance of the HEAs to a limited extent, strategy (c) can provide a multifold improvement in the radiation resistance [13–15]. One of the ways to improve the sink strength of HEAs is to have multiple interfaces either by secondary-phase precipitation or by a multimodal distribution of grain sizes, including nanostructured grains. HEAs offer significant potential for inducing such microstructural heterogeneities, but conventional casting is tedious and time-consuming [13,16–18]. For instance, the microstructure of a transformation-induced plasticity (TRIP)-enabled HEA has been innovatively engineered by Agrawal et al. for enhanced radiation resistance [13]. The processing route involved a preliminary homogenization annealing of the cast HEA followed by hot rolling to eliminate the cast defects. The rolled HEA was eventually descaled, heat-treated at 500°C (desired phase field), and then warm-rolled to obtain a massively interfaced alloy.

Considering this, additive manufacturing (AM) methods like directed energy deposition (DED) and selective laser melting (SLM) [19–22] can be beneficial, as materials with significantly better properties than those of conventionally cast counterparts can be obtained [23–27]. Moreover, straightforward one-step annealing approaches can be designed by exploiting the residual stresses in alloys produced by these AM techniques to successfully engineer microstructures with multiple interfaces desired for nuclear applications [28,29]. The DED process can also enable the fabrication of functionally graded materials that possess applications across different industries, including nuclear. Additionally, these functionally graded materials can rapidly assess the material's properties [19–22,30–33], reducing the overall cost of down selection in a given compositional space, especially HEAs [34,35]. Friction surface layer deposition (FSLD) is another recently developed solid-state processing technique that produces parts with significantly finer and compositionally homogenous microstructures that result in enhanced functional and mechanical properties [36]. Therefore, it is worthwhile for the nuclear industry to investigate novel HEAs via advanced manufacturing processes.

1.2 PNNL HEA Work Scope and Objectives

The overall objective of the PNNL HEA work scope is to evaluate the current manufacturing techniques applied for HEAs, addressing the challenges and needs for upscaling current manufacturing processes, and to identify HEAs relevant to the nuclear industry. To reach this goal, the specific work scope is shown in Figure 1 and includes the following:

1. A comprehensive literature survey of current manufacturing techniques applied for HEAs will be performed, along with the current HEAs explored in research communities. HEAs specifically relevant to nuclear applications will be identified.
2. Down-selected HEA compositions will be characterized and their properties measured to aid decision-making criteria.
3. Bulk manufacturing experiments will be carried out using both liquid- and solid-state manufacturing processes to determine the effectiveness of advanced techniques.
4. Finally, all information will be contributing towards the completion of the decision matrix for HEAs for nuclear applications with recommendations for future work to increase the technical readiness of bulk HEAs.

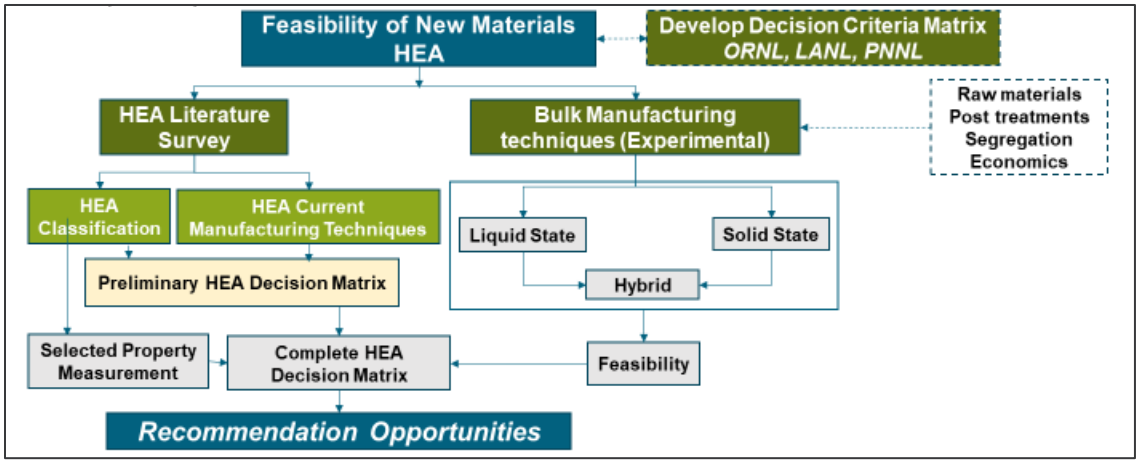

Figure 1. PNNL work scope including a literature survey and experimental work.

1.3 Report Content

This report provides a comprehensive summary of the current HEA literature pertaining manufacturing methods used for research studies, the HEA classification (type), and selected characterization and property measurements. The collaboratively determined decision matrix is briefly discussed with preliminary ratings of the selected HEAs. However, the finalization of the decision matrix will continue, as the full battery of experimental work is in process (due to the project's start date due to funding availability), which may influence the final decision based on the rating. Finally, an outlook of the work to follow is provided with preliminary conclusions based on the work performed to date.

2.0 Decision Criteria Matrix

Creating an objective decision criteria matrix for diverse new materials is challenging, especially considering the wide range of compositionally different materials that can be created. Moreover, certain materials like ODS alloys require unique and sophisticated processing routes; therefore, new criteria reflecting such complexities must be incorporated into the decision criteria matrix. A decision criteria matrix is developed in collaboration with ORNL and LANL and is presented in Table 1. This decision criteria matrix for new and diverse materials will be used to evaluate the potential of HEAs for nuclear reactor applications.

Table 1. Decision criteria matrix.

Category	Criteria	What is being evaluated?	Notes
Application Space	Applicability to different reactor types	Whether a material can be used in multiple types of reactors.	
	Other Industry Experience	The interest in and use of a material by other industries.	
	Data Availability	The availability and comprehensiveness of data associated with a given material.	Pertinent data include radiation resistance, elemental transmutation, high-temperature oxidation, stress corrosion cracking (SCC), thermal performance, creep, fatigue, tensile properties, etc.
	Code and Standards Availability	The availability of codes and standards that govern the production, material quality/standards, and implementation of a material.	Technically six areas (3 codes + 3 standards) - facets of material implementation.
	Component Versatility	The potential for a material to be used for different types of components in a nuclear reactor or power plant.	The types of components include cladding, in-core structural, out-of-core structural, and balance of plant components.
Environmental Compatibility	Radiation Resistance	The ability of a material to maintain its shape, size, and properties after exposure to radiation.	Evaluating things like a material's resistance to swelling, void formation, and embrittlement.
	Elemental Transmutation	Elemental stability of a material and impact of transmutation.	Does the material transmute to an undesirable element with detrimental properties? Does the material become activated, leading to increased dose?
	High-Temperature Oxidation Resistance	The ability of a material to resist oxidation at high temperatures.	It would perhaps be ideal to specify an oxidation rate (mm h^{-1} or g cm^{-2} h^{-1}), but this will inevitably vary with temperature. Possibly a normalization of temperature could address this.
	Neutronics Compatibility	The degree to which a material impacts the neutron economy of reactors.	Zr thermal capture cross section ~2 b, fast capture cross section ~10×10^{-2} b.
	Coolant Compatibility and	The relative stability and compatibility of a material in	Types of coolants include water (normal or supercritical [SC]), gas

Category	Criteria	What is being evaluated?	Notes
	Corrosion Resistance	coolants used in the next generation of reactors, including its resistance to corrosion, erosion, and other chemical reactions.	(CO_2, He), liquid metals (Pb, Pb–Bi, Na, NaK), and molten salts (FLiBe).
Physical and Mechanical Properties	Thermal Conductivity	Capability of a material (with high thermal conductivity) to increase the thermal efficiency of an energy system and reduce transitional thermal stress in the components.	
	Thermal Capacity	General thermal capacity, such as melting point, softening point, and phase stability, across a temperature range.	Considered steels in fast reactors at ~0.5T_M.
	Tensile Properties	High-temperature tensile properties, including strength, ductility, and type of failure.	Tensile strength and ductility can represent many other relevant properties, such as fatigue limit, fracture toughness, irradiation resistance, etc.
	Creep Performance	Risk of losing dimensional stability in long-term service.	Operation temperatures in most reactors will be well below the temperatures where creep mechanisms become active.
	Fatigue	Risk of component failure due to crack growth by cyclic loading.	New candidate materials are general high-strength materials, and components might be designed to be operated below their fatigue limits.
	Fracture Toughness	Capability to avoid the most probable failure mode with aging and degradation.	Most nanostructured and refractory materials have high crack sensitivity, but it has been ignored.
	Microstructure Dependency	The sensitivity of a material's properties to its microstructure.	If we make the material wrong, it fails. Need a high degree of expertise in materials selection and design.
	Scope for Microstructural Enhancement	The possibility of enhancing material properties by microstructural engineering through feasible processing routes.	We can enhance the microstructure to improve properties.
Manufacturability	Reproducibility/ Consistency	How reproducibly and consistently the manufacturing route for a material can fabricate components from that material.	Key factor: number of process variables that need to be carefully monitored. Highest score will be assigned to processing techniques that produce consistent microstructures and properties irrespective of the feedstock.
	Process Complexity	The number of processing steps required to produce a component from a given material.	Post- and preprocessing treatments (thermomechanical treatment, surface finishing, machining). At times, this metric can change drastically based on the type of alloy; for instance, ODS alloys needing additional

Category	Criteria	What is being evaluated?	Notes
			preprocessing will be assigned a lower score irrespective of the manufacturing route employed.
	Cost	Relative overall cost for production of components from a given material.	Considering the costs of the raw material, labor, and fabrication including post-processing. We may want to assume the final part is inevitably complex for comparison purposes.
	Scalability	The ability to increase the overall number of components being produced with a certain material and the ability to produce dimensionally larger components.	Production volume and dimensions: any scale could be chosen based on the application; for the most part, production volume is considered.
	Production Method Technology Readiness Level	The technology readiness level of common production methods used to produce components from a material.	
	Raw Material Supply	Precursor availability in the United States.	Depending on the type of process considered, the raw material supply rank must change.
	Flexibility of Manufacturing	Number of methods that can be used to manufacture material.	If a material type can potentially be manufactured via all available techniques irrespective of whether it has been done, it will be given a 5.
	Conventional Machining	The ability and need to drill, cut, or otherwise subtract material; perform bending, milling, or use computer numerical control; or use joining techniques (such as welding) to manufacture a component from the given material.	The ability to manufacture a full component using the considered processing technique.
	Near Net Shaping (Complexity of Shape)	The availability of manufacturing routes to form near net shape components from a material and the degree of complexity of that shape.	AM will be given a 5, and conventional casting techniques will be ranked lower.

3.0 Literature Survey of High Entropy Alloys

This section defines HEAs and current manufacturing techniques applied during research and provides the classification of alloys, with a review of alloy compositions and a summary of the observed properties.

3.1 What are HEAs?

HEAs are defined as alloys with five or more principal elements. The concentration of each principal element is 5%–35% [37]. In addition to the principal elements, HEAs may contain other elements in minor quantities, below 5 at%. The entropy of mixing multiple principal elements is much more pronounced in HEAs than that for conventional alloys, which possibly facilitates the formation of solid solution phases with less complicated crystal structures as compared to those in conventional alloys. However, the presence of multiple principal elements of different groups increases the propensity for the formation of multiphase microstructures in HEAs. A high mechanical strength [38], an exceptional wear resistance [39], good high-temperature properties [40], and outstanding corrosion and oxidation resistance [41,42] are commonly observed in HEAs because of their unique multi-principal-element compositions.

3.2 Current Fabrication Techniques Used for HEAs

The current state-of-the-art fabrication techniques that are employed to fabricate HEAs to date are discussed below.

3.2.1 Solid-State Processing

This route includes a preliminary step for producing (via atomization or high energy ball milling) either prealloyed HEA powders or individual elemental powders, which are later mixed using a ball mill or roller mixers to obtain the desired HEA compositions.

3.2.1.1 Cold Uniaxial Pressing and Sintering

The mixed/prealloyed HEA powders are placed inside a die (typically made of tool steel, H13 steel, EN steel) and cold-pressed by two punches (from top and bottom) for a green compact. This green compact is then sintered below its melting point to achieve a dense compact [43,44].

3.2.1.2 Hot Pressing

Hot pressing combines both cold pressing and sintering into a single step. Axial loads are applied to the heated powders so that high-density compacts can be obtained [45–47]. Advanced hot pressing, known as hot isostatic pressing (HIP), is also available for compacting HEA powders [48].

3.2.1.3 Spark Plasma Sintering

Spark plasma sintering (SPS) is an advanced sintering process that is also known as pulsed electric current sintering and is used to compact powders significantly faster than the conventional sintering process. The fewer procedural steps make this process cost, time, and energy efficient. Further, high-density parts with limited grain growth can be obtained with this process [49–52].

3.2.1.4 ShAPE/Friction Stir Additive Processing

Friction stir additive processing is a cost-effective deformation-based processing method that has recently been utilized to fabricate HEAs [53]. Shear-assisted processing and extrusion (ShAPE) is a novel technology that can potentially manufacture HEA tubes directly from powders. While HEAs have not yet been processed using this technology, Al alloy tubes with significantly higher densities have been processed from gas-atomized prealloyed powders using this technique [36].

3.2.2 Conventional Liquid-State Processing

HEAs are commercially manufactured through melting and casting techniques. One of the main drawbacks of liquid-state processing techniques is the evaporation of the low-melting-point elements. Further, slow cooling rates lead to the formation of dendritic/heterogenic microstructures, thereby requiring a post-fabrication homogenization heat treatment prior to application [54,55].

3.2.2.1 Arc Melting Process

Bulk ingots with higher densities (close to the theoretical density) can be produced via arc melting. Another advantage of the arc melting process is the low energy consumption. However, as mentioned above, arc melting produces undesired heterogenous microstructures [54].

3.2.2.2 Vacuum Induction Melting Process [56,57]

The only difference between arc melting and vacuum induction melting is that vacuum induction melting involves heating via electromagnetic induction as opposed to an electric arc in the arc melting process. The heating and cooling rates can be accurately controlled for nearly homogenous microstructures using this process as compared to those using the arc melting process [58–60]. One of the main disadvantages of this method is the poor surface finish of the solidified products, which may need post-processing in some cases.

3.2.2.3 Vacuum Levitation Melting Process

Vacuum levitation melting (VLM) uses a novel induction melting furnace where the raw metals are levitated in a crucible and alloyed by convective mixing by stirring while under a levitating force. VLM eliminates the contamination from the crucible, and the ingot retains a more uniform microstructure than that when using the traditional arc melting technique [61–64].

3.2.2.4 Directional Solidification Process

In the directional solidification process, the melt is solidified along a narrow passage in a constrained manner to promote columnar grains, identical grain boundaries, and homogeneous microstructures. This process may even be employed after arc melting/vacuum induction melting to obtain uniformly columnar microstructures for specific applications [15,65]. The processing parameters, such as the downward velocity, have been shown to impact the yield strength (YS) of the product and thus can be tuned for enhanced mechanical performance [66].

3.2.2.5 Infiltration Process

The infiltration process falls under the category of squeeze casting and has the advantage of producing components having complex shapes with relatively lower porosities. This process has mainly been employed to fabricate HEA–oxide composites [67].

3.2.2.6 Electromagnetic Stirring

Electromagnetic stirring can produce high-quality ingots with minimal defects and porosity [68,69]. It is achieved by surrounding crucibles containing the conducting metals/alloy melt with magnetic field coils (electromagnetic stirrer). Three different stirring modes—vertical, horizontal, and helical—can be attained by controlling the electromagnetic field strengths [70].

3.2.3 Liquid-State Additive Manufacturing

In addition to the typical advantages, such as design freedom, direct implementation of monolithic structures, eliminating the need for riveting/welding/joining and post-processing, minimal failure risk, low wastage, etc., AM processing results in alloys with superior mechanical properties when compared to those of conventionally processed counterparts [23,24,71,72]. Several different AM techniques are available for fabricating HEAs; however, powder bed fusion and DED are the most widely used techniques for manufacturing HEAs.

3.2.3.1 Powder Bed Fusion

Powder bed fusion techniques include SLM and selective electron beam melting (SEBM). In powder bed fusion, parts are printed on a powder bed with a substrate underneath. The supporting effect of powder enables complex structures to be printed, such as cantilever structures, hollow structures, and complex arrays. The parts manufactured by SLM and SEBM exhibit very high dimensional accuracy with negligible surface roughness. While SLM equipment is simple and works in an argon environment, it is quite sophisticated and needs a vacuum environment [73–76]. In most cases, the powder bed in SEBM is heated to avoid charging due to the electron beam, which reduces the cooling rates. On the other hand, cooling rates of up to 10^4–10^5 K s^{-1} can be achieved in SLM as opposed to less than 100 K s^{-1} in conventional casting techniques. Thus, parts with significantly finer grain and subgrain features [77,78] and enhanced mechanical properties can be produced via SLM [79].

3.2.3.2 Directed Energy Deposition

Laser engineered net shaping (LENS; [24,28]), wire arc additive manufacturing (WAAM) [80–83], and electron beam additive manufacturing (EBAM) are the most popular DED techniques used for processing HEAs. While LENS is a powder-fed technique, WAAM and EBAM are wire-fed techniques. Also, LENS utilizes a laser beam in contrast to electron beam in EBAM and an electric arc in WAAM. DED techniques typically produce parts with poor surface finish, low dimensional accuracies, and low design complexities compared to those produced with powder bed fusion techniques. However, most DED-processed HEAs exhibit better mechanical properties than those of conventionally cast counter parts.

3.3 Classification of HEAs

HEAs can be classified based on their phase stability and mode of deformation; stable HEAs deform via dislocation slip, and metastable HEAs via TRIP and/or twinning-induced plasticity

(TWIP) upon mechanical/thermal damage. Stable HEAs can be further classified based on the type of phases that constitute the microstructure (See Figure 2 for classification). Moreover, the scope for the application of HEAs across various industries is mainly determined by the mechanical properties and secondly by the mode of deformation that forms the basis for this classification. A detailed literature review of HEAs summarizing different aspects such as the microstructure, phase constitution, and primary and post-processing methods employed, including a summary of findings reported in the articles, is presented in Sections 3.4 and 3.5.

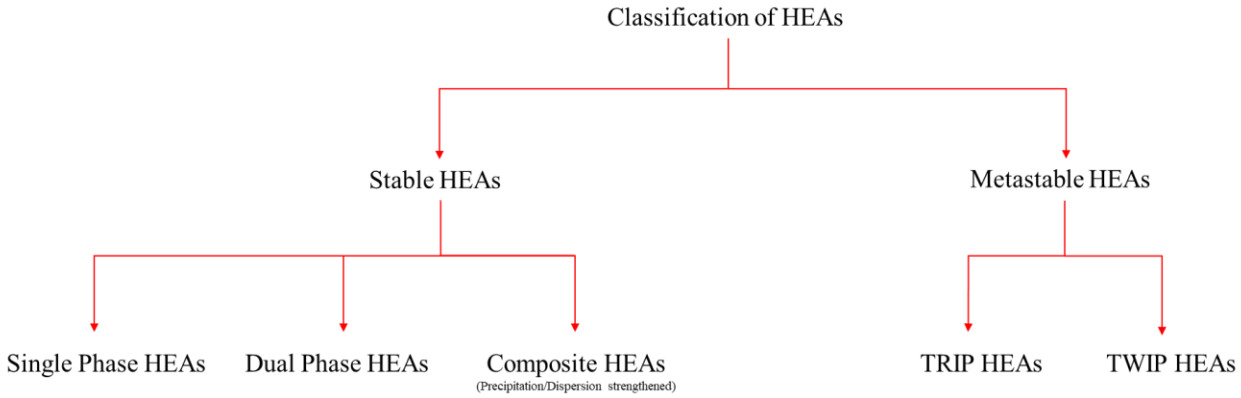

Figure 2. Classification of HEAs.

3.4 Stable HEAs

Stable HEAs are further classified as single-phase, dual-phase, and composite HEAs and are discussed in the following sub-subsections.

3.4.1 Single-Phase HEAs

A total of 75 single-phase HEAs were reviewed, and a summary is presented in Table 2. Out of the 75 HEAs listed, 61 were manufactured via arc melting, 6 via laser AM methods, 2 via SPS, and 5 via vacuum induction melting and other processes.

Table 2. Literature review of various single-phase HEAs.

Composition	Phases	Primary Processing Method	Post-Processing Method	Comments
$Al_{0.3}CoCrCu_{0.3}FeNi$	Face-centered cubic (FCC)	Arc Melting	Homogenized at 1,100°C for 6 h, followed by annealing at 900–1,100°C for 1 h	Fundamental understanding of recrystallization kinetics, Al addition to improve solid solution strengthening [84]
CoCrFeMnNi	FCC			
$Al_{0.2}CoCrFeMnNi$	FCC			
AlCoCrFeMn	Body centered cubic (BCC)	Arc Melting	None	Al-dependent phase stability; first-principles prediction [85]

Composition	Phases	Primary Processing Method	Post-Processing Method	Comments
AlCoCrFeNi	BCC	Arc Melting	None	Magnetocaloric values are comparable to those of Fe-based metallic glasses, such as Fe–Tm–B–Nb and Fe–Zr–B–Co alloys, with a similar transition near room temperature (RT) [86]
$Al_{0.3}CoCrFeNi$	FCC	Arc Melting/Floating Zone Method [87]/Single Crystal [88]	Homogenized at 1,250°C	Fundamental study on deformation mechanisms
$Al_{0.3}CoCrFeNi$	FCC	DED	None	Better mechanical properties than conventionally processed counterparts [24]
$Al_{0.3}CoCrFeNi$	FCC	SLM	None	Significantly better mechanical properties than conventionally processed counterparts [89]
$Al_{0.5}Co_{1.5}CrFeNi_{1.5}$	FCC	Arc Melting	Homogenized at a temperature of 1,150°C for 6 h	The heterogeneous microstructure containing multiple length scales of B2 ppts results in a 400% increase in yield stress when compared to the single-phase FCC condition [90]
$Al_{0.5}CoCrFeNi_{0.5}$ $Al_{0.25}CoCrFeNi_{0.75}$	BCC FCC	Arc Melting	None	Pressure-induced phase transformations from BCC/FCC to hexagonal close-packed (HCP) [91]
AlCoCrFeNiV	B2	Arc Melting	None	High-temperature *in situ* X-ray diffraction in the range of 25–800°C [92]
$Al(Co_{0.2}Cu_{0.2}Fe_{0.2}Mn_{0.2}Ni_{0.2})$ $Al(Co_{0.25}Cu_{0.25}Fe_{0.25}Ni_{0.25})$	B2	SPS	Homogenized at 1,100°C for 10 h	Single-phase intermetallic, improved hardness and low thermal conductivities [93]
$AlCoFeNiSm_{0.1}TiV_{0.9}$ $AlCoFeNiSm_{0.1}V_{0.9}$	FCC	SLM	None	Excellent corrosion resistance and hardness [94]

Composition	Phases	Primary Processing Method	Post-Processing Method	Comments
$Al_{0.075}Cr_{0.06}Fe_{0.404}Mn_{0.348}Ni_{0.113}$ + 1.1 at% C	FCC	Arc Melting	None	Substantial increase in strength, but also an increase in ductility and work-hardening rate [95]
$Co_{1.7}CrCu_{0.1}FeMo_{0.3}Ni$ $CoCrCu_{0.1}Fe_{1.7}Mo_{0.3}Ni$ $CoCrCu_{0.1}FeMo_{0.3}Ni_{1.7}$	FCC	Arc Melting	None	Phase selection studies based on atomic radius ratio, valence electron concentration, mixing entropy ΔS [96]
CoCrFeMn	FCC	Arc Melting	None	Fundamental studies [97]
$Co_{0.10}Cr_{0.15}Fe_{0.35}Mn_{0.05}Ni_{0.25}V_{0.10}$	FCC	Vacuum Induction Melting	Homogenized at 1100°C for 6 h followed by cold rolling (~70%), and then annealed above 900°C	Improved cryogenic mechanical properties [98]
CrFeCoNiPd	FCC	Arc Melting	None	Significantly higher strength and strain hardenability compared to those of CoCrFeMnNi, increased stacking fault energy [99]
CoCrMnNi	FCC	Arc Melting	None	Binary Gibbs free energy to design HEAs: fundamental study [100]
$Co_{10}Cu_{20}Mn_{30}Ni_{40}$	FCC	Vacuum Induction Melting	Homogenized at 1,100°C for 6 h, followed by cold rolling (~70%), and then annealed above 600°C	First Cu-based single-phase HEA designed by Thermocalc; improved cryogenic mechanical properties via grain refinement [101]
CoFeMnNi CoCrFeNi FeNiCoMn NiCoCrMn FeNiCo FeNiCr FeNiMn NiCoCr NiCoMn	FCC	Arc Melting	Homogenized at 1,100–1,200°C for 24 h	CoCrNi is the hardest of all the alloys in this series [102]

Composition	Phases	Primary Processing Method	Post-Processing Method	Comments
FeCoNi	FCC	DED	None	Higher YS than those of conventionally processed counterparts [23]
CuIrNiPdPtRh	FCC	Arc Melting	Annealed at 1,400°C for 2 h	Compressive strength of 1,839 MPa [103]
$Cu_2MnNiZn$ $Cu_2MnNiSn_{0.2}Zn$	FCC	Metallic Mold Casting	None	Brass HEAs: addition of Sn to $Cu_2ZnMnNi$ brass HEA reduced the ductility despite the significant hardening of the ingots [104]
$Fe_{0.267}Ga_{0.156}Mn_{0.20}Ni_{0.267}Si_{0.11}$	BCC	Arc Melting	Annealed at 973°C	HEA without rare earths: Alloy design based on literature studies [105]
TiZrHfNb $TiZrHfNb_{0.8}$	BCC BCC	DED DED	None None	The TiZrHfNb refractory HEA (RHEA) exhibits a tensile YS of ~1034 MPa and a ductility of ~18.5% at RT. Furthermore, for TiZrHfNb, the high tensile YS mainly originates from solid solution strengthening, and the large ductility results from multiple dislocation interactions promoted by the local chemical fluctuations [106]
$Ti_{40}Zr_{25}Nb_{25}Ta_{10}$ $Ti_{45}Zr_{25}Nb_{25}Ta_5$	BCC	Arc Melting	None	YS: ~910 MPa, ultimate tensile strength (UTS): ~1040 MPa YS: ~790 MPa, UTS: ~910 MPa, high corrosion resistance and good biocompatibility [107]
DyErGdHoTb	HCP	Arc Melting	None	Rare-earth HEA with giant magnetocaloric effect [108]
DyErGdHoLuScTbY DyGdHoLaTbY	HCP HCP	Arc Melting Arc Melting	None None	To explore the magnetocaloric effect [109]

Composition	Phases	Primary Processing Method	Post-Processing Method	Comments
DyGdHoTbY	HCP	Vacuum Induction Melting	None	Fundamental study: observation of single phase [110]
DyGdLuTbTm	HCP	Arc Melting	Annealed at 1173 K	Thermodynamic data from binary phase diagrams to design single-phase HEAs [111]
DyGdLuTbY	HCP	Arc Melting	None	
ErGdHoLaTbY	HCP	Arc Melting	None	To explore the magnetocaloric effect [112]
GdHoLaTbY	HCP	Arc Melting	None	The strengthening effect from the configurational entropy is not found in the alloy [113]
Al_0/$Al_{0.25}$/$Al_{0.5}$/$Al_{0.75}$/Al_1/$Al_{1.5}$ NbTiMoV	BCC	Arc Melting	None	$Al_{0.5}$NbTiMoV has the highest YS (1,625 MPa): High melting point, low weight criteria [114]
$Al_{0.4}Hf_{0.6}$NbTaTiZr	BCC	Arc Melting	HIP at 1,200°C and 207 MPa for 2 h and then annealed at 1,200°C for 24 h	Complete substitution of Cr with Al in $CrMo_{0.5}NbTa_{0.5}TiZr$ reduced the density by 10.1%, increased RT hardness and YS by ~12%. Noticeably improved RT ductility and considerably increased, by more than 50%, high-temperature strength in the temperature range of 1,073–1,473 K [115]
$(NiCoCr)_{92}Al_6Ta_2$	FCC	Arc Melting	Homogenization treatment at 1,225°C for 24 h followed by cold rolling to a sheet thickness reduction of 70%. Cold-rolled sheets rapidly heated to 1,150°C within ~20 s and dwelled for 3 min	Testing temperature from 298 K down to 77 K, the YS, ultimate strength, and tensile ductility are increased from ~600 to ~800 MPa, from ~1.0 to ~1.35 GPa, and from ~52% to ~90% [116]

Composition	Phases	Primary Processing Method	Post-Processing Method	Comments
NbTiVZr	BCC	Arc Melting	HIP at 1,200°C and 207 MPa for 2 h and then annealed at 1,200°C for 24 h	At 1,273 K, this HEA had a strength of 58 MPa [117]
MoCrTiAl	BCC	Arc Melting	Homogenized at 1,200°C for 24 h [118].	High creep and oxidation resistance: Fundamental studies on phase stability [118]
NbMoCrTiAl	BCC	Arc Melting	Homogenized at 1,300°C for 24 h	
NbMoTiAl	BCC	Arc Melting	Homogenized at 1,500°C for 24 h	
TaMoCrTiAl	BCC	Arc Melting	Homogenized at 1,500°C for 24 h	
$Al_x(HfNbTiZr)_{100-x}$ (x = 0, 3, 5, 7, 10, and 12 in atomic percent)	BCC	Arc Melting	Annealed at 1,000°C for 30 min	All HEAs were stable at 1,273 K. $Al_5(HfNbTiZr)_{95}$ exhibits excellent RT mechanical properties with a combination of fracture strength and elongation of 915.2 MPa and 31.5%, respectively [119]
$AlNb_{1.5}Ta_{0.5}Ti_{1.5}Zr_{0.5}$	BCC	Arc Melting	HIP at 1,400°C and 207 MPa for 2 h, and then annealed at 1,400°C for 24 h	A new strategy for developing low-density high-performance RHEAs: 6.9 g/cm^3 to 9.1 g/cm^3
$Al_{0.4}Hf_{0.6}NbTaTiZr$	BCC	Arc Melting	HIP at 1,200°C and 207 MPa for 2 h, and then annealed at 1,200°C for 24 h	Ta and Hf with "low-density" refractory elements (Nb, V, and Zr) and with Ti and Al [120]
$Al_{0.3}NbTa_{0.8}Ti_{1.4}V_{0.2}Zr_{1.3}$	BCC	Arc Melting		
$Ni_{38}Cr_{21}Fe_{20}Ru_{13}Mo_6W_2$	FCC	Arc Melting	Homogenized at 1,250°C for 120 h	Integrated computational materials engineering (ICME) approach for designing this HEA; exceedingly high corrosion resistance [121]
$Mo_5Nb_{10}Ta_{35}V_{15}W_{35}$	BCC	Arc Melting	Homogenized at 1,000°C in an argon-filled, vacuum-sealed quartz tube for 24 h and water-quenched	ICME approach to explore equiatomic and nonequiatomic single-phase BCC RHEAs: RHEAs exhibit microhardness and elastic modulus
$Mo_5Nb_{25}Ta_{30}V_5W_{35}$	BCC			
$Mo_5Nb_{30}Ta_{35}V_{15}W_{15}$	BCC			
$Mo_5Nb_{35}Ta_{15}V_{10}W_{35}$	BCC			
$Mo_{10}Nb_{35}Ta_{25}V_5W_{25}$	BCC			
$Mo_{15}Nb_{35}Ta_{35}V_5W_{10}$	BCC			

Composition	Phases	Primary Processing Method	Post-Processing Method	Comments
$Cr_{20}Mo_{20}Re_{20}V_{20}W_{20}$	BCC			comparable to that of existing RHEAs [122]
$Cr_5Mo_5Re_{20}V_{35}W_{35}$	BCC			
$Ti_2ZrHfV_{0.5}Mo_{0.2}$	BCC	Arc Melting	None	Excellent irradiation resistance; no irradiation hardening and abnormal lattice constant reduction after helium-ion irradiation [123]
$Re_{0.56}Nb_{0.11}Ti_{0.11}Zr_{0.11}Hf_{0.11}$	HCP	Arc Melting	None [124]	Superconducting HEAs
$(Ti_{20}Zr_{20}Hf_{23})Nb_{21}Re_{16}$	BCC	Arc Melting	None [125]	
MoReRhRu	HCP	Arc Melting	None [126]	
$(MoReRhRu)_{0.9}Ti_{0.1}$	HCP			

3.4.2 Dual-Phase HEAs

A total of 35 dual phase HEAs were reviewed, and a summary is presented in Table 3. Out of the 35 HEAs listed, 26 were manufactured via arc melting, 2 via laser AM methods, 4 via vacuum induction melting, and 3 via other processes.

Table 3. Literature review of various dual-phase HEAs.

Composition	Phases	Primary Processing Method	Post-Processing Method	Comments
$Al_{15}(CuFeMn)_{85}$	FCC+BCC	Vacuum Induction Melting	Homogenization 800°C for 6 h followed by cold rolling and annealing at 800°C for 1 h	A new strategy for designing immiscible medium entropy alloys with excellent tensile properties [127]
$Al_{15}Co_{35}Cu_{35}Mn_{15}$	FCC+B2	Vacuum Induction Melting	Homogenization 800°C for 12 h	Aluminum, a strong B2 former, and Mn, a solid solution strengthener, are added to immiscible Co–Cu alloy [128]
CoCrFeNiCuAl	FCC+BCC	Arc Melting	None	Compressive YS of 1.82 GPa and plasticity of 20.7% [129]
$Al_{0.3}CrFe_{1.5}MnNi_{0.5}$	B2+BCC	Arc Melting	Homogenized at 1100°C for 4 h	This alloy at 700°C hardens via TRIP, BCC to tetragonal sigma phase [130]
AlCoCrNi	BCC+B2	Arc Melting	None	AlCoCrNi HEA presented superior strength at high

Composition	Phases	Primary Processing Method	Post-Processing Method	Comments
				temperatures up to 873 K, which was much higher than that of commercial Ni-based superalloys. [131]
AlCoCrFeNi	FCC+B2	Arc Melting	None	A series of uniaxial compression tests were performed at target temperatures ranging from 300 to 1173 K with a strain rate of 1×10^{-3} s^{-1}. YS at 1,173 K was 201 MPa with >50% plasticity [40]
AuPdAgPtCuNi	FCC+FCC	Arc Melting	None	Reasonable strength and ductility under compression [103]
AlCrFeCoNiNb	BCC+hexagonal C14 Laves	Arc Melting	Homogenized at 1,273 K for 1 h followed by high-pressure torsion at 6 GPa	Ultrahigh hardness of 1030 Hv due to the formation of nanograins with an average size of 10 nm [132]
FeRhIrPdPt	FCC+FCC	Arc Melting	None	Magnetic behavior fundamentals [133]
$Al_{0.5}CoCrCuFeNi$	FCC+FCC	Arc Melting	None	YS: ~1250 MPa, ductility: 7.6% [134]
$Fe_{49.5}Mn_{30}Co_{10}Cr_{10}C_{0.5}$	FCC+HCP	Vacuum Induction Melting	None	Lower strength and ductility due to inhomogeneity in microstructure [135]
$CrFeCoNiAl_{0.7}$	FCC+B2	Electromagnetic Induction Melting	None	Excellent RT tensile properties with a high YS of 578 MPa, and UTS of 1015 MPa and a large elongation to fracture of ~12% [136]
$(AlCoCrFeNi)_{99.95}Y_{0.05}$	BCC+B2	Arc Melting	None	YS: ~1336 MPa, UTS: 2402 MPa [137]
$Fe_{50}Mn_{30}Co_{10}Cr_{10}$	FCC+HCP	Arc Melting	None	Corrosion behavior in H_2SO_4 exhibited lower corrosion resistance and passive film stability than did the CoCrFeMnNi single-phase HEA [138,139]
MoNbTaTiZr	BCC+BCC	Arc Melting	Stationary Friction	SFP to reduce heterogeneity; SFP

Composition	Phases	Primary Processing Method	Post-Processing Method	Comments
			Processing (SFP)	alloy showed nearly six times lower corrosion rate in simulated body fluid than as cast [140]
CoCrCuFeNi/Al layers	FCC+BCC	Magnetron Sputtering	Annealed at 550°C for 1 h	Remarkably high hardness of 10.4 GPa in nanoindentation [141]
$Fe_{1.125}Ni_{1.06}CrAl$ $Fe_{1.125}Ni_{1.125}CrAl$ FeNiCrAl	BCC+BCC	Arc Melting	None	$Fe_{1.125}Ni_{1.06}CrAl$ I_{corr} of 9.262×10^{-9} A/cm^2 and E_{corr} of −0.228 V, implying promising corrosion properties for industrial applications [142]
FeCrCuTiV	FCC+BCC	Arc Melting and DED	None	Grain size and Cu-rich (FCC) phase volume fraction of HEA prepared by DED is smaller and hence has better corrosion resistance [143]
AlFeCoNiCu	FCC+BCC	Arc Melting	Homogenized at 1273 K for 1 h, followed by high-pressure torsion at 6 GPa	The capability of the material to store lattice defects enhances the hardness to 495 Hv and provides an explanation for the reported high compressive strength and good plasticity [144]
$CoCrFeNiAl_xMn_{(1-x)}$ x = 0.2 to 0.8	FCC+BCC	Laser Cladding	None	Best corrosion resistance with maximum impedance (25,016.228 Ω/cm^2) and the minimum corrosion rate (0.0464 g/m^{2}h) when x = 0.8 [145]
$AlCoCrFeNi_{2.1}$	FCC+BCC	Arc Melting	None	$AlCoCrFeNi_{2.1}$ EHEA showed superior molten salt corrosion resistance than DS2205 stainless steel (SS), including higher Ni content in EHEA and sacrificial role of Al in reducing outward diffusion of

Composition	Phases	Primary Processing Method	Post-Processing Method	Comments
				Cr, Fe, and Ni in $AlCoCrFeNi_{2.1}$ and the different reactivity of formation of chlorides, as well as enrichment of Co and Ni in the corrosion layer [146]
$Fe_{47}Mn_{30}Co_{10}Cr_{10}B_3$	FCC+HCP	Arc Melting	Homogenized at 1,000°C for 12 h, followed by cold rolling and annealing at 1,000°C for 1–5 min	Fundamental work: First, boride enhances the load-bearing capacity of individual interfaces through an increase in grain boundary (GB) cohesion, thereby reducing the probability of occurrence of catastrophic interface failure. Second, interface solute decoration and the reduced GB energy introduce an enhanced GB drag effect and a reduced Gibbs–Thomson force during recrystallization, leading to grain refinement [147]
$Al_{0.5}CoCrFeNiSi_{0.25}$	FCC+BCC	Vacuum Induction Melting	None	Tensile strength of 1267.8 MPa; fracture toughness of 34.4% [148]
$Fe_{42}Mn_{28}Co_{10}Cr_{15}Si_5$	FCC+HCP	Vacuum Induction Melting	None	Exceptional superplastic elongation at relatively higher strain rates [149]
$AlCrCuFeNi_x$ (x = 2.0, 2.5, 2.75, 3.0)	FCC+BCC	SLM (self-developed LSNF-1 SLM)	None	Deformation nanotwins, stacking faults, and strain-activated B2-to-FCC phase transition are discovered in BCC phase [150]
NiAlCoFeNb $Ni_{30}Al_{30}Co_{20}Fe_{15}Nb_5$ $Ni_{25}Al_{25}Co_{20}Fe_{20}Nb_{10}$	B2+hexagonal Laves phase	Arc Melting	None	Ultrahigh hardness of 818 Hv for NiAlCoFeNb: Laves-phase-reinforced

Composition	Phases	Primary Processing Method	Post-Processing Method	Comments
				alloys generally exhibit high thermal stability and excellent high-temperature mechanical properties [151]
$Fe_{36}Mn_{21}Cr_{18}Ni_{15}Al_{10}$	BCC/B2+FCC	Arc Melting	None	YS: 750 and 990 MPa in compression and tension, respectively at RT. At 600°C, tensile and compression YS are 310 and 360 MPa, respectively [152]
$(AlCoCrFeNi)_{100-x}Sc_x$ HEAs (x = 0, 0.5, 1 and 2, at%)	B2+BCC	Arc Melting	None	With an increase of Sc, the YS exhibits an improvement from ~1293 to ~1441 MPa [153]
$AlMo_{0.5}NbTa_{0.5}TiZr$	BCC+BCC	Arc Melting	HIP at 1,400°C and 207 MPa for 2 h, and then annealed at 1400°C for 24 h	Two BCC phases were intertwined, resulting in a basketweave microstructure.
$Al_{0.3}NbTaTi_{1.4}Zr_{1.3}$				
$Al_{0.5}NbTa_{0.8}Ti_{1.5}V_{0.2}Zr$			HIP at 1,200°C and 207 MPa for 2 h, and then annealed at 1200°C for 24 h	$AlMo_{0.5}NbTa_{0.5}TiZr$ shows a YS of ~745 MPa with >50% plasticity in compression at 1,000°C [154]

3.4.3 Composite HEAs (Precipitate/Dispersion Strengthened)

A total of 33 composite HEAs were reviewed, and a summary is presented in Table 4. Out of the 33 HEAs listed, 16 were manufactured via arc melting, 10 via laser AM methods, 3 via vacuum induction melting, and 4 via other processes.

Table 4. Literature review of various composite HEAs.

Composition	Phases	Primary Processing Method	Post-Processing Method	Comments
$Al_{0.3}Ti_{0.2}Co_{0.7}CrFeNi_{1.7}$	FCC+$L1_2$	Arc Melting	Solution treated at 1,200°C for 1 h followed by cold rolling (to 80% reduction)	Low-cost alloy with an extremely high specific strength of 218 MPa/g/cm^3, as compared to specific strengths of Ni-based

Composition	Phases	Primary Processing Method	Post-Processing Method	Comments
			and annealing at 600°C for 50 h	alloys (<150 MPa/g/cm^3) and most steels (<200 MPa/g/cm^3) [155]
$Al_{0.3}Ti_{0.2}Co_{0.7}CrFeNi_{1.7}$	FCC+$L1_2$	DED	None	Mechanical properties identical to those of conventional counterparts, as-deposited (AD) microstructure contained residual stresses [28]
$Al_{10}Nb_{15}Ta_5Ti_{30}Zr_{40}$	B2+BCC	SLM (PROX200 (California, U.S.))	None	Low density, high YS: the compressive YS at RT was found to be ~1400 MPa with a plasticity greater than 45% (did not fail) [156]
$Al_{0.3}$CoCrFeNi	FCC+$L1_2$	DED	Annealed at 620°C for 5 h	Significantly high YS of 600 MPa with 20% ductility at RT [24]
$Al_{0.3}$CoCrFeNi	FCC+$L1_2$	Arc Melting	Homogenization at 1150°C followed by annealing at 620°C for 50 h	Significantly high YS of 650 MPa with 45% ductility at RT [38]
$Al_{0.2}Co_{1.5}CrFeNi_{1.5}Ti_{0.3}$	FCC+$L1_2$	Arc Melting	Homogenized at 1,200°C for 48 h, followed by hot rolling, solution annealing at 1,150°C for 3 h, and low-temp annealing at 700°C, 800°C, 900°C, and 1,000°C for 1 h	The optimized mechanical properties, YS of 745 MPa, UTS of 1160 MPa, and elongation to fracture of ~42%, are realized in the HEA aged at 700°C or 800°C for 1 h [157]
$Al_{0.3}$CoCrFeNi	FCC+B2 +sigma	Arc Melting	Homogenization at 1,150°C followed by cold rolling and annealing at 620°C for 50 h	Direct annealing for reducing the energy barriers for B2 precipitation [38]
$Al_{0.3}$CoCrFeNi	FCC+B2+ BCC+sigma	Arc Melting	Homogenization at 1,150°C followed by cold rolling and	Direct annealing for reducing the energy barriers for B2 precipitation [38]

Composition	Phases	Primary Processing Method	Post-Processing Method	Comments
			annealing at 550°C for 24 h	
$AlCoCrFeNb_{0.25}Ni$	BCC+ (Laves+BCC)	Arc Melting	None	$AlCoCrFeNb_{0.5}Ni$ exhibited the highest YS of ~2500 MPa and 4.1% plasticity under compression [158]
$AlCoCrFeNb_{0.5}Ni$	BCC+ (Laves+BCC)			
$AlCoCrFeNb_{0.75}Ni$	Laves+ (Laves+BCC)			
$Al_{0.5}Co_{1.5}CrFeNi_{1.5}$	FCC+B2	Arc Melting	Homogenized at a temperature of 1,150°C for 6 h, followed by cold rolling and annealing at 750°C for 50 h	The heterogeneous microstructure containing multiple length scales of B2 ppts results in a 400% increase in yield stress when compared to the single-phase FCC condition [159]
$Al_{0.5}Co_{1.5}CrFeNi_{1.5}$	FCC+$L1_2$		Homogenized at a temperature of 1,150°C for 6 h followed by annealing at 750°C for 50 h	
$Al_{0.3}CoCrFeNi$	FCC+B2	Vacuum Induction Melting	Homogenization at 1,150°C for 1 h, followed by cold rolling and annealing at 800°C for 50 h	Excellent strength–ductility combination by embedding hierarchical B2 precipitates into a heterogeneous grain structure: YS: ~702 MPa and 30% ductility under tension [160]
$(Ni_2Co_2FeCr)_{92}Al_4Nb_4$	FCC+$L1_2$	Arc Melting	Homogenization was conducted at 1,200°C for 2 h followed by cold rolling into thin sheets with a total thickness reduction of ~66%. The cold-rolled sheets were	This alloy exhibits the highest tensile strength, with UTS of ~1232 MPa and YS of ~ At 600°C; the YS and UTS of this alloy were measured to be ~681 MPa and ~991 MPa, respectively. YS anomalies at 760°C

Composition	Phases	Primary Processing Method	Post-Processing Method	Comments
			subsequently recrystallized at 1,200°C for 1.5 min, followed by oil quenching, and finally aged at 800°C with different durations	with a YS of ~720 MPa and a UTS as high as ~900 MPa, 850 MPa at RT [161].
$Al_{0.3}Cu_{0.5}CrFeNi_2$ + 0.073 at% C	FCC+$L1_2$ +$M_{23}C_6$	Vacuum Induction Melting	Cold rolled then annealed at 1,000°C for 3 h and subsequently at 1,200°C for 0.5 h. Three sets of samples were isothermally aged at 550°C for 150 h (A550), 700°C for 50 h (A700), and 900°C for 20 h (A900), respectively	The synergistic strengthening effects of $L1_2$ phase and $M_{23}C_6$ carbides in the aged samples rendered the improved strength, accompanied by the maintenance of a high elongation at RT [162]
FeCoCrNiMn +1.3 at% C	FCC+$M_{23}C_6$	Arc Melting with Electromagnetic Stirring	Homogenized at 1,220°C for 6 h, then the cold rolled followed by annealed for 1 h at temperatures ranging from 700°C to 1000°C	~1040 MPa with total elongation of ~12% has been achieved in the HEA after annealing at 700°C [163]
$Cr_{19.68}Mn_{19.68}Fe_{19.68}Co_{19.68}Ni_{19.68}Nb_{0.8}C_{0.8}$	FCC+NbC	Arc Melting	Homogenized first at 1,473 K for 24 h and then at 1523 K for another 2 h	The YS and UTS of the microalloyed HEA are increased significantly to 732 and 911 MPa, respectively, while retaining a high elongation of 32% [164]
$FeCoCrNiMnTi_{0.3}C_{0.3}$	FCC+TiC+ $M_{23}C_6$+M_7C_3	Mechanical Alloying Followed by Vacuum Hot pressing	None	Compression YS: ~1445 MPa, plastic strain 11.5%, and compression strength 1999 Pa [165]
$CoCrFeNiMnC_{0.2}$	FCC+M_7C_3	Arc Melting	None	YS: ~700 MPa, plasticity 10% [166]

Composition	Phases	Primary Processing Method	Post-Processing Method	Comments
$(Fe_{40}Mn_{40}Co_{10}Cr_{10})_{3.2}C_{6.8}$	FCC+$M_{23}C_6$	Arc Melting	None	YS: ~620 MPa, ductility 26.5% [167]
CoCrFeMnNi +1.84 at% C	FCC+$M_{23}C_6$ +M_7C_3	Arc Melting	Homogenized for 24 h at 1,050°C followed by cold rolling and annealing at 900°C for 1 h	YS: ~527 MPa, ductility 40% [168]
$Fe_{19.84}Mn_{19.84}Ni_{19.84}Co_{19.84}Cr_{19.84}C_{0.8}$	FCC+$M_{23}C_6$	Vacuum Induction Melting	Hot-rolled at 950°C followed by homogenization at 1,200°C for 3 h followed by cold rolling and annealing at 900°C in Ar for 3 min	YS of ~1030 MPa and UTS of ~1170 MPa with uniform elongation of ~11% [169]
FeCoCrNiMn + 1.0 at% C	FCC+$M_{23}C_6$	Arc Melting	Homogenization annealed at 1,100°C for 12 hours, followed by cold rolling and annealing at 800°C for 1 h	YS: ~638 MPa, ductility 30% [170]
$Fe_{40.4}Ni_{11.3}Mn_{34.8}Al_{7.5}Cr_6$ + 1.1 at% C	FCC+B2+ M_7C_3+$M_{23}C_6$	Arc Melting	Cold rolled and annealed at 1073 K for 8 h, 1173 K for 8 h, 1273 K for 1 h, 1273 K for 8 h, and 1373 K for 4 h	YS: ~557 MPa, ductility 25% [171]
$CoCrFeNiV_{0.5}C_x$ (x = 0.01, 0.02, 0.03 and 0.04)	FCC+M_7C_3	Arc Melting	Hot rolled to a 20% reduction in thickness, followed by homogenized at 1,200°C for 3 h, followed by water cooling treatment. After that, amount of cold rolling was 70%, followed by annealing 600°C for 1 h, 700°C for 1 h,	The YSs(σ_y) of $CoCrFeNiV_{0.5}C_{0.02}$ and $CoCrFeNiV_{0.5}C_{0.03}$ alloys annealed at 700°C are 1339.7 and 1264.6 MPa, respectively, with excellent performance [172]

Composition	Phases	Primary Processing Method	Post-Processing Method	Comments
			and 800°C for 1 h.	
CoCrFeMnNi + 5 wt% NbC	FCC+Nb segregation at dislocation cell boundaries	SLM	Few specimens are annealed at 800°C for 2 h	YS: ~870 MPa at RT and 420 MPa at 800°C: the dislocation cells in this HEA are stable, and a superior combination of thermal stability and strength is achieved through the addition of NbC nanoparticles [173]
CoCrFeMnNi + 5 wt% TiB_2	FCC+TiB_2	DED	None	TiB_2 acts as nucleation sites and promotes the formation of grain-refined and dislocation-populated microstructures. YS of ~600 MPa at RT. Self-lubricating wear resistance [174]
$Co_{1.5}CrFeNi_{1.5}Ti_{0.5}Mo_{0.1}$	FCC+$L1_2$	SLM (EOSINT M280, EOS Corporation) and Electron Beam Melting (EBM; Arcam A2X, Arcam AB)	Solution-treated at 1393 K for 3 h	The solution-treated SLM (1400 MPa) and EBM (1300 MPa) specimens exhibited higher tensile strengths than those of conventional high-corrosion-resistant alloys in harsh, corrosive environments, such as duplex stainless steels (Duplex stainless steel: 655 MPa, Super duplex stainless steel: 750–800 MPa, and Ni-based superalloys (Alloy C276: 690 MPa, Alloy 718: 1275 MPa) [175]
$TiZrHfNb_{0.6}$	BCC+omega	DED	None	Poor mechanical properties; embrittlement due to omega precipitation [176]

Composition	Phases	Primary Processing Method	Post-Processing Method	Comments
CrMnFeCoNi + 1.5 at% C (C-HEA)	FCC+$Cr_{23}C_6$	SLM (Concept Laser Mlab Cusing)	Annealed at 650°C for 1 h	Microstructural evolution did not occur, even in crept sample at a creep strain of 7% under applied stress of 325 MPa at 500°C [177]
GRX 810 (Developed by NASA) (Co-33%, Cr-29%, Re-1.5%, Al-0.3%, Ti-0.25%, Nb-0.75%, W-3%, C-0.05%, Ni-Balance) all in wt%	FCC+carbides +Y_2O_3	SLM (EOS M280)	None	The best material for creep, oxidation, and strength at higher temperatures [178]
NiCoCr + 1 wt% Y_2O_3	FCC+Y_2O_3	SLM (EOS M280)	None	This new processing technique employed resonant acoustic mixing to coat an equiatomic NiCoCr powder with nanoscale yttrium oxides [179]

3.5 Metastable HEAs

3.5.1 TRIP/TWIP HEAs

A total of 21 metastable HEAs were reviewed, and a summary is presented in Table 5. Out of the 21 HEAs listed, 16 were manufactured via arc melting, and 5 via vacuum induction melting.

Table 5. Literature review of various metastable HEAs.

Composition	Phases	Primary Processing Method	Post-Processing Method	Comments
49.5Fe–30Mn–10Co–10Cr–0.5C (at%)	FCC	Arc Melting	Hot rolling followed by homogenization at 1,200°C for 2 hours, then cold rolled and annealed at 400, 650 and 750°C	Nanotwin/ nanograined engineered FCC microstructure exhibited 1.3 GPa; the FCC grains transformed to hcp martensite [180]
$Co_{35}Cr_{20}Mn_{15}Ni_{15}Fe_{15}$	FCC	Arc Melting	Homogenized at 1473 K for 5 h, subsequently forged	TWIP; YS: 231 MPa, UTS: 688 MPa [181]

Composition	Phases	Primary Processing Method	Post-Processing Method	Comments
$Co_{35}Cr_{25}Mn_{15}Ni_{15}Fe_{10}$			at 1473 K to a 50% reduction in thickness. The forged samples were aged at 1273 K for 10 min by RT rolling to a 40% reduction in thickness. Finally, the samples were aged at 1273 K for 6 min	TRIP; YS: 305 MPa, UTS: 806 MPa [181]
$Fe_{40}Mn_{10}Co_{20}Cr_{20}Ni_{10}$	FCC	Vacuum Induction Melting	Hot-rolled at 900°C, followed by homogenization at 1200°C for 2 h. After homogenization, the HEA was cold-rolled, subsequently annealed at 800°C for 30 min, followed by water quenching	YS: ~375 MPa UTS: ~785 MPa Ductility: 77.5% FCC → HCP [182]
$Cr_{20}Mn_{24}Fe_{30}Co_{20}Ni_{6}$	FCC+sigma	Vacuum Induction Melting	Hot-rolled at 900°C, followed by homogenization at 1250°C for 2 h. After homogenization, the HEA was cold-rolled, subsequently annealed at 800°C for 5–10 min, followed by water quenching	TRIP: high strength but low ductility [183]
$Cr_{20}Mn_{15}Fe_{34}Co_{20}Ni_{11}$	FCC			TWIP: better combination of strength and ductility [183]
$Fe_{50}Mn_{25}Ni_{10}Cr_{15}$	FCC	Arc Melting with Electromagnetic Stirring	Cold rolling followed by homogenization at 1173 K for 10 min	Tensile strength of ~0.98 GPa and ductility of ~83% at 77 K, TRIP and TWIP [184]
$(NiCoCr)_{92}Al_6Ta_2$	FCC	Arc Melting	Homogenization treatment at 1,225°C for 24 h, followed by cold rolling to a sheet with a thickness reduction of 70%. Finally, the cold-rolled sheets were rapidly heated to 1,150°C within ~20 s and dwelled for 3 min	Testing temperature from 298 down to 77 K, the YS, ultimate strength, and tensile ductility are increased from ~600 to ~800 MPa, from ~1.0 to ~1.35 GPa, and from ~52% to ~90% [185]

Composition	Phases	Primary Processing Method	Post-Processing Method	Comments
$Fe_{50}Mn_{30}Co_{10}Cr_{10}$	FCC+HCP	Vacuum Induction Melting	Hot-rolled at 900°C, followed by homogenization at 1,200°C for 2 h. For various grain sizes and phase fractions, the homogenized alloy was cold-rolled and subsequently annealed at a furnace temperature of 900°C in Ar for 3–60 min	FCC γ to HCP ε, formation of stacking faults & dislocation slip in the FCC γ phase. At later stages of deformation, additional mechanical twinning, dislocation slip, and formation of stacking faults in HCP ε phase are also activated as important deformation mechanisms. This shows that the HCP ε phase also partitions a certain portion of the imposed load. YS: 305 MPa and UTS: 830 MPa [186]
$Cr_{20}Mn_6Fe_{34}Co_{34}Ni_6$	FCC+HCP	Vacuum Induction Melting	Hot-rolled at 900°C, followed by homogenization at 1,200°C for 3 h; the homogenized alloy was cold-rolled and subsequently annealed at a furnace temperature of 800°C for 1 h	YS: 600 MPa, UTS: 1000 MPa [187]
$Ti_{60}Mo_{10}V_{10}Cr_{10}Zr_{10}$	BCC	Arc Melting	None	Compressive YS: ~1298 MPa, UTS: ~2000 MPa, plasticity 33.4% [189]
$Ti_{35}Zr_{27.5}Hf_{27.5}Nb_5Ta_5$	BCC	Arc Melting	The structure and grain size were controlled by cold rolling with a 60% and 70% reduction in thickness, followed by a 30 min solution treatment in helium at 900°C and 800°C, respectively	YS: ~540 MPa, UTS: ~995 MPa, ductility ~23% BCC → orthorhombic [190]
$Ti_{55-x}Zr_{20}Hf_{15}Al_{10}Nb_x$ (x = 5–8 at%)	BCC	Arc Melting	None	YS: ~735 MPa, UTS: ~1051 MPa

Composition	Phases	Primary Processing Method	Post-Processing Method	Comments
				BCC → orthorhombic [191]
$Ti_{35}Zr_{27.5}Hf_{27.5}Nb_5Ta_5$	BCC	Arc Melting	None	YS: ~121 MPa, UTS: 574 MPa
$Ti_{38}Zr_{25}Hf_{25}Ta_{10}Sn_2$				YS: ~407 MPa, UTS: 925 MPa
$Ti_{38}Zr_{25}Hf_{25}Ta_7Sn_5$				YS: ~232 MPa, UTS: 409 MPa BCC → HCP [192]
$Ti_{40}Zr_{25}Nb_{25}Ta_{10}$	BCC	Arc Melting	None	YS: ~910 MPa, UTS: 1040 MPa
$Ti_{45}Zr_{25}Nb_{25}Ta_5$				High corrosion resistance and good biocompatibility [192]
$Ti_{48}Zr_{20}Hf_{15}Al_{10}Nb_7$	BCC	Arc Melting	Cold-rolled into sheets with 30% reduction in thickness and then annealed at 800°C and 900°C for 30 min	UTS: ~900 MPa, YS: ~700 MPa BCC → orthorhombic [193]
Fe–20Mn–20Co–15Cr–5Si–1.5Cu	FCC	Vacuum Induction Melting	Homogenized (1,100°C) in the γ-FCC region for 2 h to obtain maximum γ-FCC and then rolled at 900°C (γ-FCC domain) to a final thickness of ~6.5 mm to get rid of the casting defects. The rolled sheet was then descaled and heated to 500°C and then warm-rolled to a final thickness of ~3.15 mm.	σ body-centered tetragonal (BCT) phase in the higher combination of dpa and temperature, the extreme case of 100 dpa/500°C. Resistant to void formation and swelling. Reversing the irradiation-induced transformation by temperature-induced transformation and thus minimizing degradation due to irradiation [194]

3.6 Survey of Prior HEA Research for Nuclear Applications

This section discusses the HEAs that were specifically developed targeting nuclear applications. A total of 40 HEAs were reviewed, and a summary is presented in Table 6. Out of the 40 HEAs listed, 20 were composite HEAs, 19 were single-phase HEAs, and 1 was a dual-phase HEA. Since the literature survey identifies the potential in both single and composite HEAs, we have

down-selected HEAs in both categories for further investigation, and the experimental results are presented in Section 4.0.

Table 6. Literature review of various HEAs for nuclear applications.

Composition	Phases	Primary Processing Method	Post-Processing Method	Comments
				Compression YS: ~224 MPa @900°C, ~346 MPa @800°C
$V_{35}Ti_{35}Fe_{15}Cr_{10}Zr_5$ Classification: Dual-Phase HEAs	BCC+BCC dendritic microstructure	Vacuum Arc Melting	Annealed at 1,000°C for 3 h for comparison	Design: Fe, Cr, Ti, V, and Zr low activation elements for fusion and Zr for solid solution strengthening. No irradiation was performed [195]
$W_xTaTiVCr$ (x = 0.3–0.9) Classification: Composite HEAs	BCC+TiC+ C15 Laves	SPS	None	x = 0.32–0.63 The compressive strength (~2000 MPa) is two-fold higher than those of pure W and W-containing HEAs. Low activation elements [196]
				Low activation elements
TiVNbTa Classification: Single-Phase HEAs	BCC	Vacuum Arc Melting	None	The difference in the hardness values before and after irradiation is negligible: <5%. No radiation-induced hardening [197]
TiVZrTa Classification: Composite HEAs	BCC+BCC+ BCC	Vacuum Arc Melting	None	Low activation elements The difference in the hardness values before and after irradiation is negligible: <5% No radiation-induced hardening [197]; NiCoCr shows significantly less defect clustering compared to Ni and NiFe alloys [198]
TiVCrTa Classification: Composite HEAs	BCC+Laves			
NiCoCr Classification: Single-Phase HEAs	FCC			

Composition	Phases	Primary Processing Method	Post-Processing Method	Comments
$Al_{0.1}CoCrFeNi$ Classification: Single-Phase HEAs	FCC	VLM	none	The volume swelling of FCC is the least among the three: 1.25% @ 50 dpa and RT. The volume swelling in AlxCoCrFeNi alloys in ascending order is FCC < FCC + BCC < BCC, while the order is BCC < FCC for conventional nuclear materials. The irradiation-induced volume swellings in AlxCoCrFeNi HEAs are significantly lower than those of conventional nuclear materials under similar irradiation dosages [199]
$Zr_{32}Hf_{30}Nb_{38}$ Classification: Single-Phase HEAs	BCC (nanocrystalline)	Sputter Deposition (1 mm thick)	None	High-intensity electron beam of 2 MeV: the structure remained unchanged up to 12 dpa at 298 K (25°C) and up to 40 dpa at 103 K (−170°C) Atomic-level strains are principal mechanism for radiation resistance [200]
HfTaTiVZr Classification: Single-Phase HEAs	BCC	Arc Melting	None	There is no change in hardness up to 750°C Increase in hardness and YS for the HEA was ~20% and for SS304 was ~50% under identical irradiation conditions Better irradiation resistance of the HEA was attributed to its self-healing ability. Sluggish diffusion of atoms in the HEA reduced effective

Composition	Phases	Primary Processing Method	Post-Processing Method	Comments
				interstitial and vacancy mobility and limited irradiation-induced damage [201]
$W_{38}Ta_{36}Cr_{15}V_{11}$ Classification: Single-Phase HEAs	BCC, bimodal grain size distribution with ~70% of the grains with sizes in the nanocrystalline regime (≤100 nm) and some regions of ultrafine grain sizes (100 to 500 nm)	Magnetron Sputtering Deposition	None	Concurrent transmission electron microscopy (TEM) and atom probe tomography (APT) analyses demonstrate the existence of a second phase rich in Cr and V, first forming lamella-like regions to transform to quasi-spherical precipitates after irradiation Irradiation at 800°C at 8 dpa did not reveal any dislocation loops, but precipitation at the nanoscale occurred. Slight hardening is also observed [202]
CoCrFeMnNi–5 wt% NbC Classification: Composite HEAs	FCC+Nb segregation at dislocation cell boundaries	SLM	Few specimens are annealed at 800°C for 2 h	YS: ~870 MPa at RT and 420 MPa at 800°C: the dislocation cells in this HEA are stable, and a superior combination of thermal stability and strength is achieved through the addition of NbC nanoparticles [203]
$(Ni_2Co_2FeCr)_{92}Al_4Nb_4$ Classification: Composite HEAs	FCC+$L1_2$	Arc Melting	Homogenization was conducted at 1,200°C for 2 h, followed by cold rolling into thin sheets with a total thickness reduction of ~66%. The cold-rolled sheets were subsequently recrystallized at 1,200°C for	This alloy exhibits the highest tensile strength, with UTS of ~1232 MPa and YS of ~ At 600°C, the YS and UTS of this alloy were measured to be ~681 MPa and ~991 MPa, respectively. YS anomalies at 760°C with a YS of ~720 MPa and a UTS as high as ~900 MPa, 850 MPa at RT [161]

Composition	Phases	Primary Processing Method	Post-Processing Method	Comments
			1.5 min, followed by oil quenching, and finally aged at 800°C for 24 h	
$NbTiVZr_{0.5}$ Classification: Composite HEAs NbTiVZr Classification: Composite HEAs $NbTiVZr_2$ Classification: Composite HEAs	BCC+HCP	Arc Melting	Homogenized at 1,200 ± 10°C (1473 ± 10 K) for 100 h, followed by annealing at 700°C for 100 h	Whilst the neutron cross sections of the alloys are markedly higher than that of Zr, the combination of properties required for future advanced nuclear reactors operating at increased temperatures may be advantageous. Low neutron cross section elements [204]
MoNbCrVTi Classification: Single-Phase HEAs MoNbCrZrTi Classification: Composite HEAs	BCC BCC+Laves	Vacuum Arc Melting	None	Low thermal neutron cross section elements. The MoNbCrVTi alloy exhibits a hardness of 494.4 ± 7.7 Hv, a high YS of 1281 MPa, and fractured at a strain of 9.4% at RT [205]
$Ti_2ZrHfV_{0.5}Mo_{0.2}$ Classification: Single-Phase HEAs	BCC	Vacuum Arc Melting	None	Ti: good corrosion resistance. Mo and V elements: good high-temperature performance. Hf and Zr elements: good neutron-penetrating properties Lattice constant decreases after irradiation; first to report the abnormal X-ray diffraction phenomenon of metallic alloys after irradiation Almost no hardening after irradiation [206]
MoNbTaW Classification: Single-Phase HEAs	BCC	Vacuum Arc Melting	Solution-Treated at	(MoNbTaW: 550 Hv, MoNbTaTi: 420 Hv, MoNbTaTiW: 479 Hv)

Composition	Phases	Primary Processing Method	Post-Processing Method	Comments
MoNbTaTi Classification: Single-Phase HEAs			1,200°C/ 1,500°C	Irradiation hardening of MoNbTaTiW is less than that of MoNbTaTi, possibly because of the high entropy effect There is no noticeable irradiation hardening of MoNbTaW At a depth of 350 nm, the irradiation hardening of MoNbTaTi and MoNbTaTiW was less than that of pure W [207]
MoNbTaTiW Classification: Single-Phase HEAs				
$Mo_{0.5}VNbTiCr_x$ (x = 0, 0.25, 0.5, 0.75, 1.0, 1.5, and 2.0) Classification: Composite HEAs	BCC+FCC+ Laves	HIP	None	Cr0, Cr0.25, Cr0.5, and Cr0.75-single-phase BCC Cr1.0, Cr1.5, and Cr2.0-BCC+C15 Laves phase+FCC (TiC/N) The YS increases from 1135 MPa for the Cr0 alloy to 2311 MPa for the Cr2.0 alloy Mo0.5VNbTi and Mo0.5VNbTiCr0.25 alloys exhibit superior corrosion resistance than that of the Zr-4 alloy in superheated steam at 400°C and 10.3 MPa [208]
$Fe_{38}Mn_{40}Ni_{11}Al_4Cr_7$ Classification: Single-Phase HEAs	FCC	VLM	Annealed at 530°C for 4 h	Interstitial carbon can inhibit the irradiation hardening of HEAs The hardening rate of the C0 sample is 65.56%, whereas those of the C0.2, C0.5, and C1.0 samples are 34.8%, 43.6%, and 24.92%, respectively [63]

Composition	Phases	Primary Processing Method	Post-Processing Method	Comments
$Ti_{48.2}V_{44}Cr_{3.6}Al_{4.2}$ Classification: Single-Phase HEAs	BCC	VLM	None	YS: ~800 MPa with 35% ductility at RT [209]
$Al_{20}Be_{20}Fe_{10}Si_{15}Ti_{35}$ Classification: Composite HEAs	Ordered hexagonal+ minor intermetallics (Ti,Fe)Al_2 and Ti_5Si_3	Vacuum Arc Melting	None	Density of 3.91 g cm^{-3} and exhibits a high hardness of HV 911. Excellent oxidation resistance at 700°C and 900°C, which is much better than that of Ti–6Al–4V. Therefore, the present alloy is promising for high-temperature applications requiring lightweight, wear-resistant, and oxidation-resistant components [210]
$W_{29.4}Ta_{42}Cr_{5.0}V_{16.1}Hf_{7.5}$ Classification: Single-Phase HEAs	BCC	Magnetron Sputtering Deposition	None	Showed only approximately 10 nm change in grain size after ~8.45 at% He implantation Grain refinement observed during dual-beam irradiation Depletion of Hf from grain boundaries during irradiation, which can be attributed to the inverse Kirkendall effect and/or ballistic mixing during irradiation. No loop formation, and the total change in volume is ~0.3 % after 8.45 dpa and higher percentage of implanted He [211]
$Zr_{35}Ti_{30}Nb_{20}Al_{10}Ta_5$ Classification: Composite HEAs $Zr_{35}Ti_{30}Nb_{20}Al_{10}V_5$ Classification: Composite HEAs	BCC+B2	Vacuum Arc Melting	None	Low neutron absorption cross sections. Tensile YS of ~850 MPa/~848 MPa with elongation of

Composition	Phases	Primary Processing Method	Post-Processing Method	Comments
				~25%/~16% at RT [212]
$AlCrFeNiTi_x$ (x = 0, 0.5, 1) Classification: Composite HEAs	BCC+B2	Argon Levitation Melting	None	Size of dislocation loops in the BCC phase was smaller than that in the B2 phase for AlCrFeNi Small size and large density of dislocation loops formed in Ti0.5, especially in B2 phase. Ti nanoparticles in B2 caused a high entropy effect that hinders the movement of defects, showing the relatively excellent radiation resistance compared to that for BCC [213]
CrNbTaVW Classification: Composite HEAs $CrNbTaVW_{1.7}$ Classification: Composite HEAs	BCC+other minor phases	Upgraded Field-Assisted Sintering	None	Effect of irradiation was more severe in CrNbTaVW1.7 when compared to CrNbTaVW, evidencing swelling in all surfaces [214].
NiCoCrFePd Classification: Single-Phase HEAs	FCC	Vacuum Arc Melting	1,200°C for 24 h	Resistance against irradiation hardening behavior at high fluence under 1.05 MeV Xe^{+3} ion irradiation. Simultaneous recrystallization and recombination of point defects lead to the softening effect in the mechanical behavior at higher fluence, which is a good sign of resistance towards mechanical failure [215]
(3.1-Cr, 5.9-Nb, 21.7-Ta, 3.3-Ti, 21.7-W)-44.3 at% C [HEC] Classification: Single-Phase HEAs	FCC	Direct-Current Magnetron Sputtering	None	HEC and HEA have not displayed any local chemical instabilities (such as radiation-induced segregation [RIS] and radiation-

Composition	Phases	Primary Processing Method	Post-Processing Method	Comments
				induced precipitation [RIP]) because of atomic collisions with their microstructures.
1.8-Cr, 9-Nb, 46-Ta, 1.1Ti, 42.1-W [HEA] Classification: Single-Phase HEAs	BCC			Surprisingly, amorphization did not occur for HEC up to 10 dpa at the temperatures of relevance for light-water reactors. HEC has a slightly higher radiation tolerance than HEA [216]
$CrFeNi_{2.5}Mo$ Classification: Composite HEAs	FCC+FCC+sigma	Arc Melting and Copper Mold Suction Casting	None	Co- and Cu-free HEAs $Al_{1.0}CrFeNi_{2.5}$ alloy exhibits excellent mechanical properties with a UTS, elongation, and hardness of 1090 MPa, 16.8%, and 336 HV The E_{corr}, I_{corr}, and I_{pass} results indicate that $Al_{0.5}Mo_{0.5}$ possesses excellent comprehensive corrosion resistance in 3.5 wt% NaCl with the lowest I_{corr} and I_{pass} as well as a more positive E_{corr} [217]
$Al_{1.0}CrFeNi_{2.5}$ Classification: Composite HEAs	FCC+BCC+BCC			
$Al_{0.5}CrFeNiMo_{0.5}$ Classification: Composite HEAs	FCC+FCC+BCC+sigma			
$Al_{0.2}CrFeNiMo_{0.8}$ Classification: Composite HEAs	FCC+FCC+sigma			
$Al_{0.8}CrFeNiMo_{0.2}$ Classification: Composite HEAs	FCC+BCC+sigma			
$Nb_{25}Mo_{25}Ta_{25}W_{25}$ Classification: Single-Phase HEAs	BCC	Vacuum Arc Melting	None	RT to 1,600°C compression properties RT: 1100 MPa, peak strain 2% 800°C: 552 MPa, ductility >22% 1000°C: 548 MPa 1,600°C: 405 MPa [218]

3.7 Promising HEA Candidates for Nuclear Applications Based on All Surveyed HEAs

The HEAs that can be recommended based on the literature surveys presented in previous sections are as follows:

1. $Al_{0.3}Cu_{0.5}CrFeNi_2$, $Al_5Cr_{12}Fe_{35}Mn_{28}Ni_{20}$, and $Al_{10}Cr_{12}Fe_{35}Mn_{23}Ni_{20}$ are face-centered cubic (FCC)-based HEAs suggested by the U.S. Nuclear Regulatory Commission (NRC) report titled “Use of High Entropy Alloys (HEAs) in Future Nuclear Applications” published in January 2023. All three alloys exhibit good mechanical properties at RT.
2. $(Ni_2Co_2FeCr)_{92}Al_4Nb_4$ is a precipitation-strengthened HEA exhibiting a YS of ~500 MPa with a ductility of ~6% at 870°C. It is one of the few HEAs that exhibit remarkable high-temperature mechanical properties.
3. GRX-810 is an ODS alloy recently developed by the National Aeronautics and Space Administration (NASA) with high-temperature (at 1093°C) creep performance 2–3 orders of magnitude better than that of current high-temperature alloys. Since GRX-810 is mainly a three-component NiCoCr-based alloy with minor additions of other elements such as Al, Ti, Nb, W, and C, it may not be strictly classified as an HEA. However, this material can be best classified as a medium entropy alloy or an ODS alloy because of the presence of Y_2O_3 particles. ***Therefore, we recommend pursuing this material under a different work package under the AMMT program.***
4. $Al_{0.3}Ti_{0.2}Co_{0.7}CrFeNi_{1.7}$ is a precipitation-strengthened FCC HEA reported to exhibit a yield strength of ~1630 MPa and a good tensile ductility of ~15% at room temperature, which is significantly higher than most stainless steels (SSs). This HEA is also expected to have high-temperature stability up to ~1100 °C.

4.0 Experimental Work

The primary objective of this work is to conduct advanced manufacturing feasibility studies on the down-selected promising HEAs based on the elaborate literature survey presented in Section 3.0. This provides information to evaluate the benefits (if any) of advanced manufacturing methods that enable bulk economic manufacturing routes and may additionally further enhance the properties of the selected HEAs. The advanced manufacturing routes include both liquid- and solid-state manufacturing approaches. Table 7 summarizes the experimental work executed to date in fiscal year (FY) 2023 and the work in progress. FSLD is considered for two down-selected HEAs ($Al_{0.3}Ti_{0.2}Co_{0.7}CrFeNi_{1.7}$ and $Al_{10}Cr_{12}Fe_{35}Mn_{23}Ni_{20}$) because of their unique processing conditions that result in finer microstructures with compositionally homogenous grains that would potentially enhance mechanical properties. In addition, the effect of solid-phase processing on the mechanical properties of a single-phase HEA can also provide valuable information and potentially more economical routes to HEA adoption in the market. The technical details of the completed work are provided in the following sections.

Table 7. Completed experimental work.

HEA	Tasks Completed
$Al_{0.3}Ti_{0.2}Co_{0.7}CrFeNi_{1.7}$ Classification: Composite HEA (See Section 4.1)	1. Microstructural characterization of laser powder bed fusion (LPBF) and DED samples (as-processed and annealed conditions). 2. Nanoindentation testing from RT to 500°C of LPBF and DED samples (as processed & annealed conditions) 3. Process parameter optimization for FSLD processing 4. Room-temperature hardness and microstructural characterization of the optimized FSLD conditions
$Al_{10}Cr_{12}Fe_{35}Mn_{23}Ni_{20}$ Classification: Composite HEA (See Section 4.2)	1. Procured cast rods 2. Process parameter optimization for FSLD processing and scanning electron microscopy (SEM) characterization
Compositionally Graded HEA SS316 to $CoCrNiFe_{0.5}$ (with trace amounts of Ta, Ti, Mo, Si, and Nb) **Classification:** Single-Phase HEA (See Section 4.3)	1. Samples manufactured by DED 2. Microstructural characterization at the interface between the substrate (SS316) and base layer of the graded HEA 3. Microstructural characterization at the interface between the matrix (HEA) and the unmelted powder particles (SS316)

4.1 Down-Selected HEA: $Al_{0.3}Ti_{0.2}Co_{0.7}CrFeNi_{1.7}$

4.1.1 Background

The $Al_{0.3}Ti_{0.2}Co_{0.7}CrFeNi_{1.7}$ HEA is a precipitation-strengthened alloy reported to exhibit a YS of ~1600 MPa with decent ductility at room temperature (RT) and is expected to have high-

temperature stability up to ~1100°C [16]. This HEA was fabricated via two different AM techniques: DED and SLM. The evolution of the heterogeneous microstructures in the as-deposited (AD) and subsequently annealed conditions and their tensile properties at RT has been reported previously [29,219]. However, the temperature-dependent mechanical behavior essential for nuclear applications was not yet investigated. This report provides a discussion of the microstructural differences and the temperature-dependent (from RT to 500°C) nanoindentation behavior of the heterogeneous microstructures obtained via one-step annealing, post-DED, and SLM processing of the $Al_{0.3}Ti_{0.2}Co_{0.7}CrFeNi_{1.7}$ HEA. The differences in the nanoindentation behavior between the AD and one-step annealed conditions of the DED- and SLM-processed conditions are determined. The work presented in Section 4.1 has been accepted for publication in a peer-reviewed journal [220].

4.1.2 Materials and Methods

This study used the Optomec LENS-750 system equipped with an IPG YLS-1500 fiber laser system (with a maximum power output of 1500 W) for DED and the Trumpf TruPrint 1000 laser powder bed fusion (LPBF) system used for SLM. Prealloyed powders of $Al_{0.3}Ti_{0.2}Co_{0.7}CrFeNi_{1.7}$ procured from TOSOH, SMD were used for both DED and SLM processing. The samples were provided by the University of North Texas.

The AD specimens from DED [referred to as DED(AD)] and SLM [referred to as SLM(AD)] were sectioned using the KENT USA (WSI-200) electric discharge machine (EDM). Sections from DED(AD) and SLM(AD) specimens were then individually encapsulated in a quartz tube backfilled with argon for the heat treatments (800°C for 5 h, followed by water quenching). These conditions will be hereafter referred to as DED(HT) and SLM(HT).

Scanning electron microscopy (SEM) imaging was performed on all four conditions using an FEI-Quanta Nova-Nano SEM 230. Nanoindentation tests (Hysitron Inc., Minneapolis, MN, USA) were performed at RT, 250°C, and 500°C using a Sapphire Berkovich tip. The tests were carried out at a load of 1000 mN with a loading time of 5 s, a hold time of 2 s, and unloading time of 5 s. The spacing between indents was 50 µm to avoid overlap of plastic zones from adjacent indents. The high-temperature indentations were done in an $Ar+H_2$ atmosphere to minimize oxidation of the samples, and the system was allowed to stabilize at each temperature for at least 15 min before performing the indentations. A minimum of 25 good indents were used for hardness calculations for statistics.

Vacuum induction melted cylindrical bars of $Al_{0.3}Ti_{0.2}Co_{0.7}CrFeNi_{1.7}$ were procured from Sophisticated Alloys, Inc. The 25.4-mm-diameter and 152.4-mm-length feed rods were sectioned from the as-received (AR) HEA bars for FSLD. A commercially available plate of SS304 was used as a substrate for deposition. The nominal compositions of the HEA rods and the SS304 plate, as per the certification provided by the vendors, are listed in Table 8. A Transformation Technologies, Inc., machine was used for FSLD of the HEA. The AR HEA and the FSLD-processed HEA specimens were polished using standard metallographic procedures for microstructural characterization and hardness measurements.

Table 8. Chemical composition of the SS304 substrate and HEA feed rods.

	Elements (wt%)								
Materials	Fe	Cr	Co	Ni	Mn	Al	Ti	Si	C
SS304 (substrate)	Bal.	18.18	-	8.03	1.87	-	-	0.28	0.03
HEA (feed rod)	20.95	19.50	15.47	37.43	-	3.03	3.59	-	-

An OLYMPUS BX51M microscope was used for low-magnification optical microscopy (OM). A JEOL 7600 field emission gun (FEG) scanning electron microscope equipped with energy-dispersive spectroscopy (EDS) and electron backscatter diffraction (EBSD) detectors was used for imaging, phase identification, and compositional analysis. Elemental maps, inverse pole figure (IPF) maps, and phase maps were generated using Aztec Crystal software from the EBSD scans. The microhardness measurements were performed using a CLARK CM-802AT automatic hardness tester, and a load of 500 gf and a dwell time of 10 s were used.

The phase fraction versus temperature plot for the $Al_{0.3}Ti_{0.2}Co_{0.7}CrFeNi_{1.7}$ HEA was simulated using Thermo-Calc 2020b software (with the TCHEA3 database).

4.1.3 Results and Discussion

The SEM backscatter images for the as-deposited [DED(AD)] and one-step annealed conditions (DED(HT)) of the DED-processed $Al_{0.3}Ti_{0.2}Co_{0.7}CrFeNi_{1.7}$ HEA are shown in Figure 3(a–c) and Figure 3(d–f), respectively. The DED(AD) specimen shows a single-phase (FCC) microstructure with reasonably large, peculiarly shaped [23] grains often with jagged grain boundaries. Additionally, some grains also exhibit solidification cells, presumably arising from compositional segregation due to the high solidification rates involved in DED processing. However, the possible formation of early-stage nanoscale $L1_2$ precipitates within the FCC matrix of the DED(AD) specimen was previously observed in high-energy synchrotron X-ray diffraction results [219]. The annealing heat treatment (800°C for 5 h) conducted on the DED-processed HEA led to the partial recrystallization of FCC grains and significant growth of the non-recrystallized FCC grains. The grain size of the non-recrystallized grains increased from ~81 μm in DED(AD) to ~159 μm in DED(HT) [219]. The annealing heat treatment also resulted in the formation of $L1_2$ precipitates with two different morphologies within the FCC matrix. The SEM images in Figure 3(d–e) reveal the rod-like $L1_2$ precipitates in the recrystallized FCC grains, while the SEM image in Figure 3(f) shows *equiaxed*/near-spherical $L1_2$ precipitates in the non-recrystallized grains. The precipitation mechanism fundamentally differs between the two kinds of grains: continuous precipitation in the non-recrystallized grains and discontinuous precipitation in the recrystallized grains, leading to different morphologies for the $L1_2$ precipitates [219].

The SEM backscatter images for the as-deposited [SLM(AD)] and the one-step annealed conditions [SLM(HT)] of the SLM-processed $Al_{0.3}Ti_{0.2}Co_{0.7}CrFeNi_{1.7}$ HEA are shown in Figure 4(a–c) and Figure 4(d–f), respectively. The SLM(AD) specimen exhibits elongated, possibly growing epitaxially, FCC grains with a significant fraction of solidification cells involving substantial compositional segregation [Figure 4(a–b)]. Unlike the DED(AD) specimen, the intercellular walls in the SLM(AD) specimen exhibited a BCC+B2 microstructure [29]. The high-magnification SEM image of the intercellular region in Figure 4(c) clearly shows the fine-scale

B2 precipitates in the darker BCC phase inside the cell wall. The SLM(AD) specimen also showed early-stage nanoscale $L1_2$ precipitates within the FCC matrix [29]. The microstructures of the SLM(HT) specimen in Figure 4(d–f) appear to be identical to those of the DED(HT) specimen [Figure 3(d–f)]. However, the $L1_2$ precipitates in the SLM(HT) specimen are marginally more refined than those in the DED(HT) specimen. The grain sizes in the AD (~50 μm) and one-step annealed (~20 μm) specimens are also lower for the SLM-processed alloy compared to the DED-processed alloy.

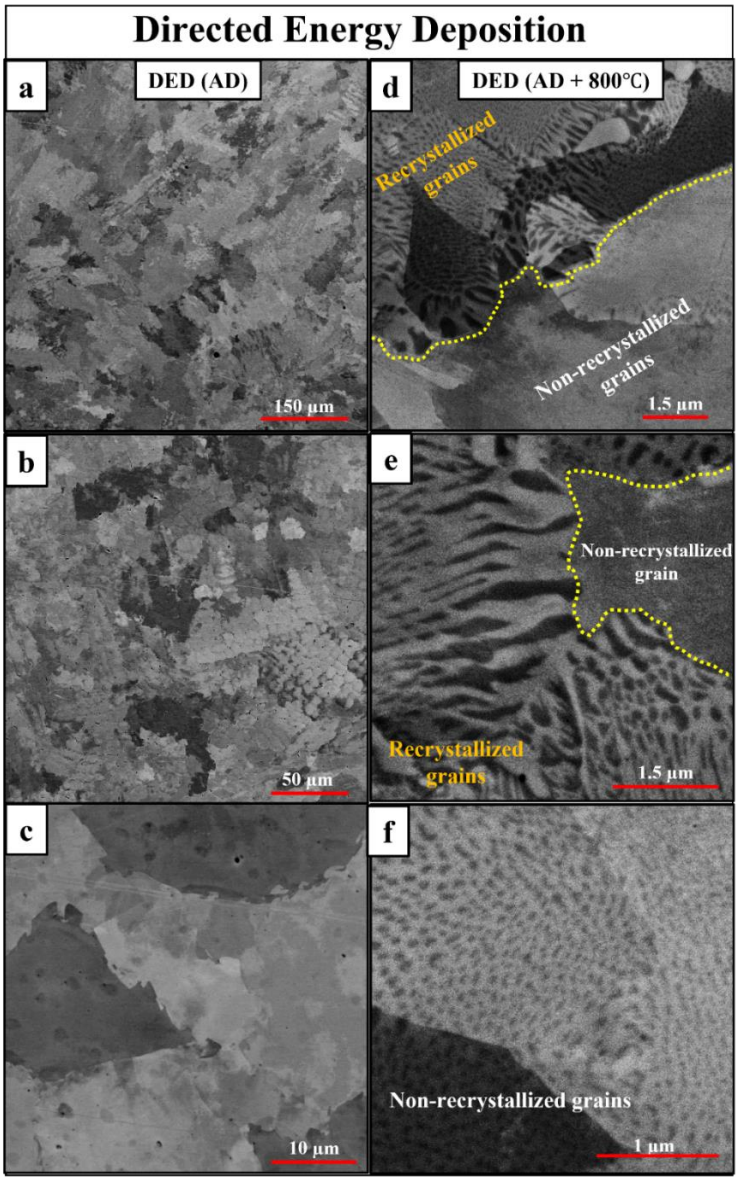

Figure 3. Low-, medium-, and high-magnification SEM backscatter images for (a–c) DED(AD) and (d–f) DED(HT or AD+800°C) specimens of the DED-processed $Al_{0.3}Ti_{0.2}Co_{0.7}CrFeNi_{1.7}$ HEA.

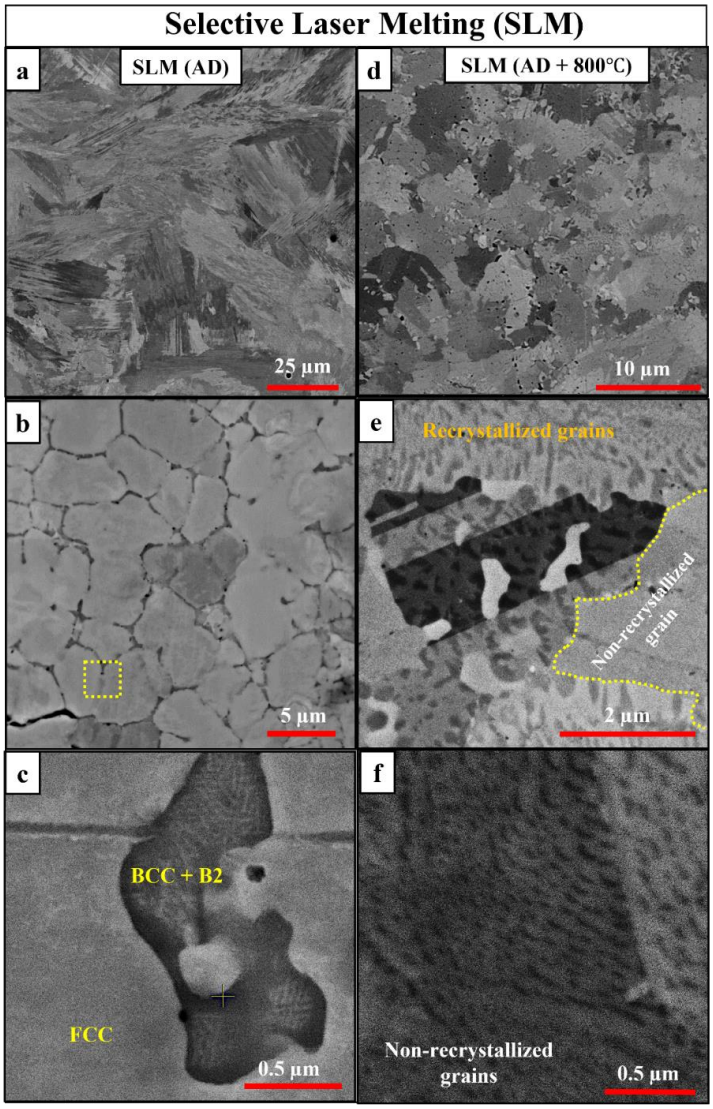

Figure 4. Low-, medium-, and high-magnification SEM backscatter images for (a–c) SLM(AD) and (d–f) SLM(HT or AD+800°C) specimens of the SLM-processed $Al_{0.3}Ti_{0.2}Co_{0.7}CrFeNi_{1.7}$ HEA.

In short, the AD specimens of DED- and SLM-processed HEAs exhibited a predominantly single-phase FCC microstructure with a negligible fraction of $L1_2$ precipitates. Although the SLM(AD) specimen revealed a B2+BCC microstructure in the intercellular regions between solidification cells, it is shown to have an insignificant effect on the mechanical properties owing to its low phase fraction and large separation distances [29]. On the other hand, both heat-treated conditions, SLM(HT) and DED(HT), exhibited hierarchically heterogeneous microstructures at multiple length scales, finer recrystallized FCC grains with rod-like $L1_2$ precipitates, and coarser non-recrystallized FCC grains with equiaxed/spherical $L1_2$ precipitates.

Table 9. Nanoindentation hardness (in GPa) for all four conditions of AM-processed $Al_{0.3}Ti_{0.2}Co_{0.7}CrFeNi_{1.7}$ HEA.

AM method	Condition	RT	250°C	500°C	% Loss
DED	AD	4.157 ± 0.287	3.763 ± 0.212	3.197 ± 0.233	23.13 ↓
	AD+800°C (HT)	4.710 ± 0.123	4.663 ± 0.183	4.387 ± 0.153	6.5 ↓
SLM	AD	4.116 ± 0.145	3.569 ± 0.171	3.560 ± 0.121	13.3 ↓
	AD+800°C (HT)	4.654 ± 0.171	4.494 ± 0.132	4.427 ± 0.104	4.9 ↓

The nanoindentation tests were performed at three different temperatures, RT, 250°C, and 500°C for all four AM-processed HEA conditions. The resultant hardness versus temperature plots are presented in Figure 5, and the corresponding hardness values are listed in Table 9. The percent loss (reduction) in hardness between RT and 500°C is calculated for all four conditions using the following equation:

$$\%\ \text{loss (reduction)} = \frac{\text{Hardness(RT)} - \text{Hardness(500°C)}}{\text{Hardness(RT)}} \quad (1)$$

The calculated values are listed in the last column of Table 9. The heat-treated conditions [DED(HT) and SLM(HT)] exhibited remarkably higher hardness values (>4.3 GPa) at all three temperatures compared to the as-deposited conditions. This increase in the hardness can be attributed to the significantly higher phase fraction of $L1_2$ precipitates in the heat-treated specimens as opposed to the much lower fractions of precipitates observed in the AD specimens. The anticipated decrease in the hardness with an increase in the temperature from RT to 500°C is observed for all four conditions, as shown in Figure 5. However, the percent reduction in the hardness for the AD specimens [23.1% for DED(AD) and 13.3% for the SLM(AD)] is substantially higher than that for the heat-treated specimens [6.5% for DED(HT) and 4.9% for SLM(HT)]. This large difference in percent reduction in the hardness can be mainly attributed to two factors: (i) relieving stored residual stresses in the AD specimens during the high-temperature testing and (ii) the softer single-phase FCC microstructure compared to the harder hierarchical multiphase microstructures in the heat-treated specimens. It should be emphasized that the lower values of percent reduction in hardness with an increase in temperature in the heat-treated specimens further ***signify the stability of the hierarchically heterogeneous microstructures at elevated temperatures***.

While both DED and SLM AD conditions showed nearly identical hardness values at RT, the SLM(AD) specimen showed a significantly higher hardness than that of the DED(AD) specimen at elevated temperatures, especially at 500°C [Figure 5(c)]. However, the heat-treated specimens, DED(HT) and SLM(HT), showed practically overlapping performance at all three temperatures, as shown in Figure 5(d). The load versus displacement (*P*–*h*) curves obtained from the nanoindentation tests for all four specimens are presented in Figure 6. Serrated yielding behavior, also known as the Portevin–Le Chatelier (PLC) effect, is observed in the loading portion of the *P*–*h* curves for the DED(AD) and SLM(AD) specimens tested at 500°C, as shown in Figure 6(c). These perturbations or discontinuities indicate the mechanical instability of the microstructure during the deformation process. The serrated yielding behavior in metals or alloys is commonly associated with the activation of a heterogenous dislocation source and its multiplication under loading [221]. However, Schuh's review [222] on "Nanoindentation studies of materials" additionally points out that phase transformations that occur during the nanoindentation process could also result in serrated yielding or the PLC effect [223]. Therefore,

microstructural characterization of the DED(AD) and SLM(AD) specimens was performed post-nanoindentation (at 500°C), and the resultant SEM backscatter images are presented in Figure 7(a, b) and Figure 7(c, d), respectively. Features resembling $L1_2$ precipitates are present in both specimens, demonstrating the possibility of dynamic precipitation of the $L1_2$ phase within the FCC matrix during the nanoindentation testing at 500°C. Moreover, the phase fraction versus temperature prediction for this HEA ($Al_{0.3}Ti_{0.2}Co_{0.7}CrFeNi_{1.7}$) presented in Figure 8 indicates that there is almost 40% $L1_2$ phase at 500°C. It is envisaged that dynamic precipitation pins the mobile dislocations, locally restoring hardness during deformation [224,225] Therefore, the serrated yielding observed in the DED(AD) and SLM(AD) specimens during nanoindentation loading (at 500°C) could be mainly due to the precipitation of the $L1_2$ phase within the FCC matrix.

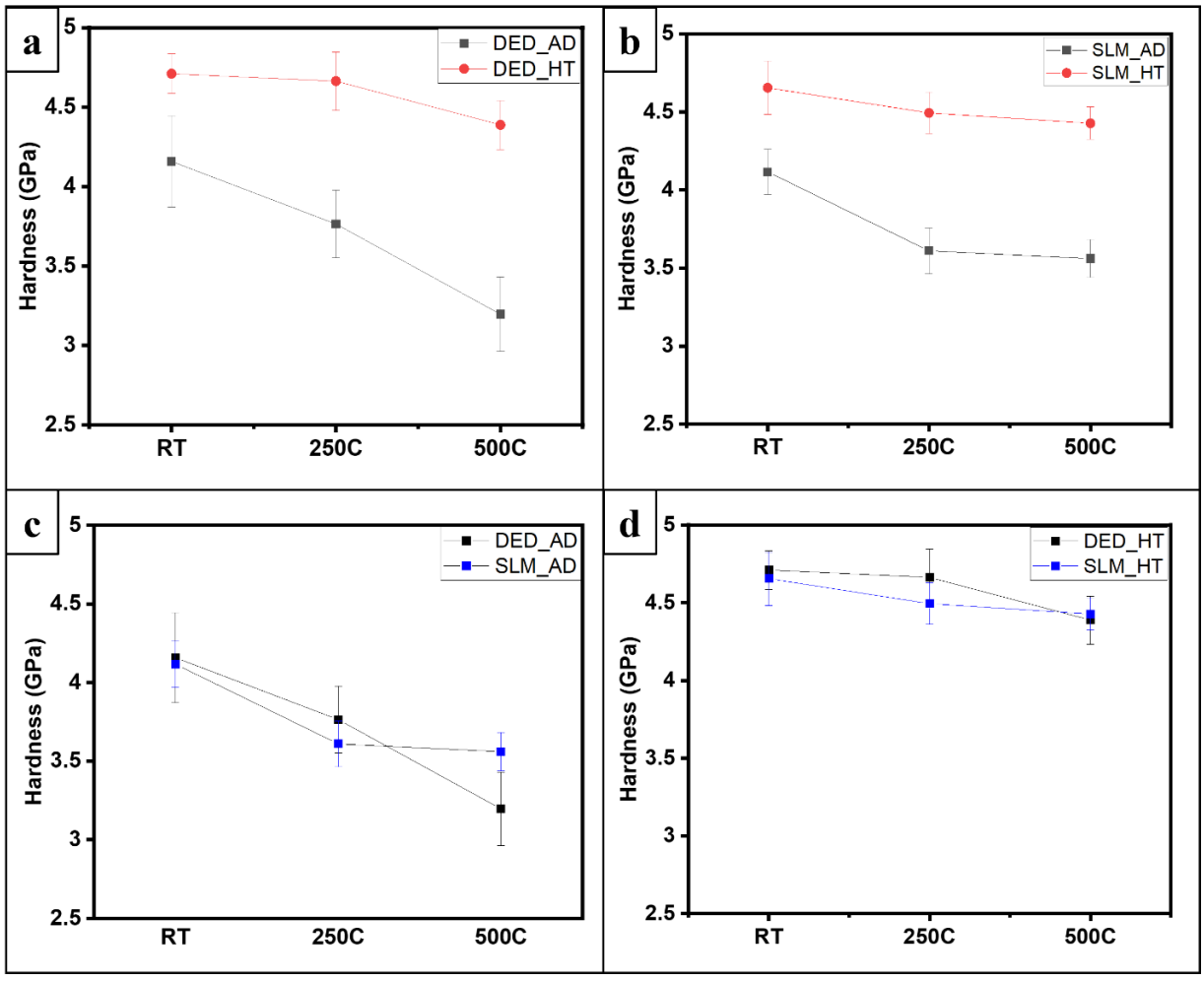

Figure 5. Hardness versus temperature plots comparing (a) DED(AD) and DED(HT) specimens, (b) SLM(AD) and SLM(HT) specimens, (c) DED(AD) and SLM(AD) specimens, and (d) DED(HT) and SLM(HT) specimens of the AM-processed $Al_{0.3}Ti_{0.2}Co_{0.7}CrFeNi_{1.7}$ HEA.

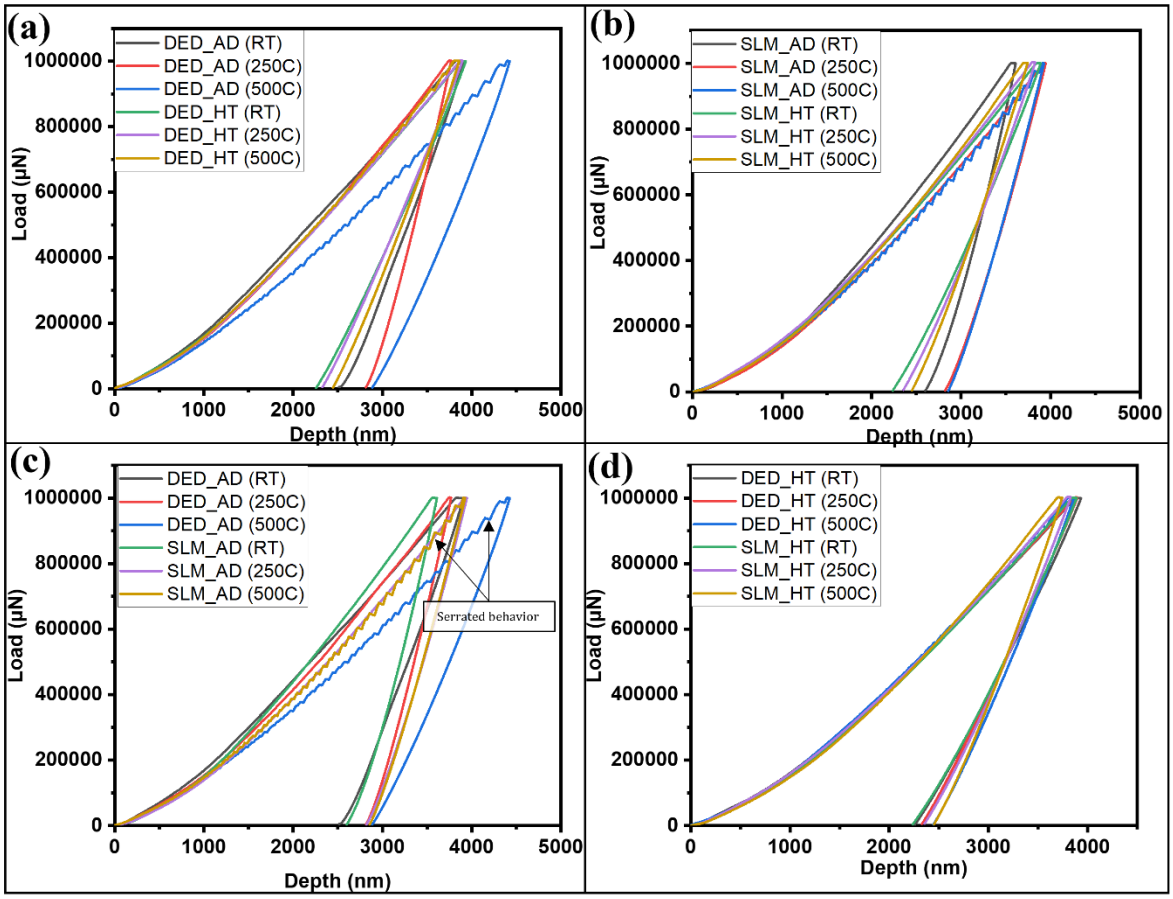

Figure 6. Representative load versus displacement (*P–h*) curves as a function of temperature comparing (a) DED(AD) and DED(HT) specimens, (b) SLM(AD) and SLM(HT) specimens, (c) DED(AD) and SLM(AD) specimens, and (d) DED(HT) and SLM(HT) specimens of the $Al_{0.3}Ti_{0.2}Co_{0.7}CrFeNi_{1.7}$ HEA.

It should be noted that the same serrated behavior is not observed for the SLM(AD) or DED(AD) specimens tested at RT or 250°C [Figure 6(c)]. The phase fraction versus temperature plot in Figure 8 reveals no significant change in the $L1_2$ phase fraction for temperatures below 500°C. Therefore, it is intuitive that sluggish diffusion at lower temperatures makes $L1_2$ precipitation kinetically unfavorable. Hence, no serrations are observed in the *P–h* curves for the DED(AD) and SLM(AD) specimens tested at RT and 250°C. Similarly, the *P–h* curves in Figure 6(d) for the DED(HT) and SLM(HT) specimens did not reveal any signs of serrated yielding during nanoindentation, which ***again illustrates the stability of the hierarchically heterogeneous microstructures during deformation at elevated temperatures.***

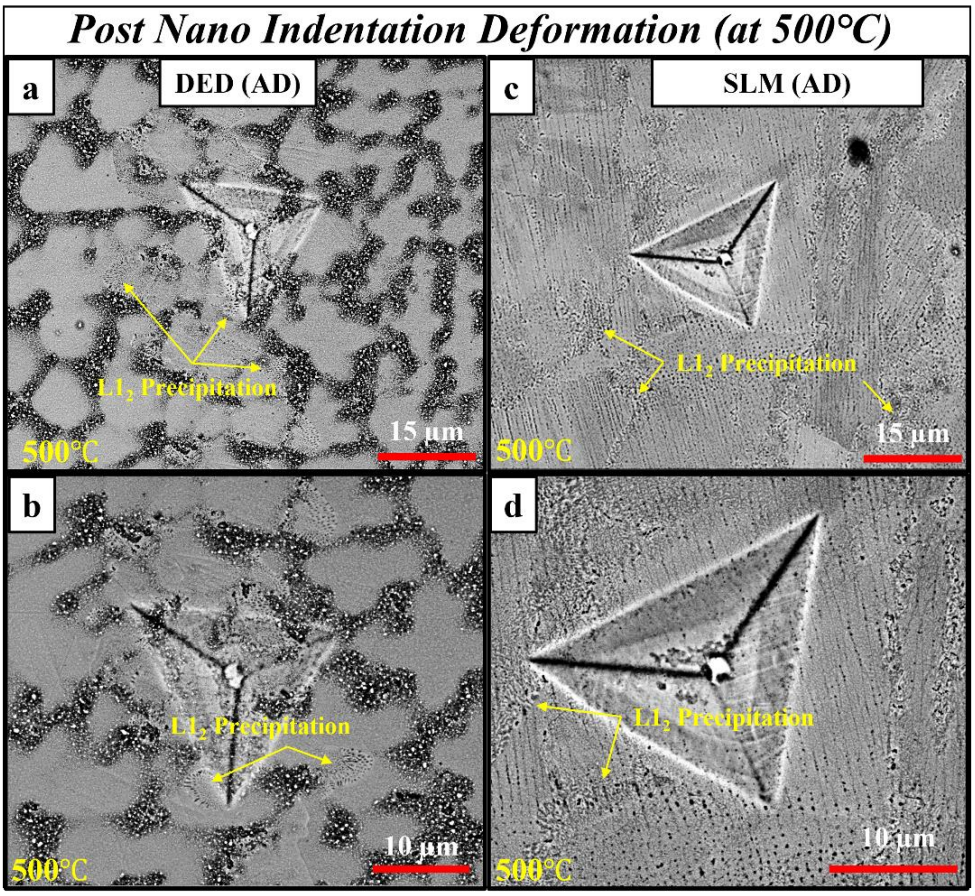

Figure 7. SEM backscatter images revealing $L1_2$ precipitation post-nanoindentation deformation at 500°C for (a, b) DED(AD) and (c, d) SLM(AD) specimens of the AM-processed HEA.

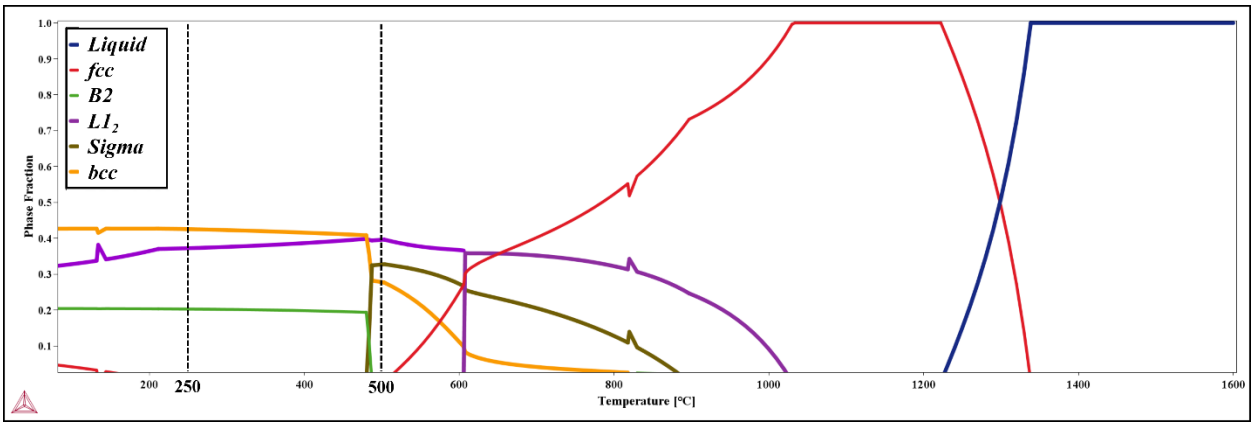

Figure 8. Phase fraction versus temperature plot for the $Al_{0.3}Ti_{0.2}Co_{0.7}CrFeNi_{1.7}$ HEA generated using Thermo-Calc software.

Further, an SEM analysis of the AR cylindrical bars of the HEA has been performed to evaluate the initial microstructure before FSLD processing. The low-magnification optical image in Figure 9(a) reveals the presence of pores close to the center of the ingot. The different colored square

boxes in the optical image represent the regions from which SEM backscatter images were obtained. The low-magnification SEM backscatter images revealing the grain structure are presented in Figure 9(b–f). The microstructure appears to be typical of a cast specimen with long columnar grains elongated along the radial direction. In addition, features resembling solidification cells are observed in the columnar grains. High-magnification SEM images were acquired for Regions 1 and 2 in Figure 9(a), and the resultant images are presented in Figure 10(a–c) and Figure 10(d–f), respectively. These SEM images reveal coarse grains of a secondary BCC phase sparsely distributed along the boundaries of FCC columnar grains. Furthermore, both FCC and BCC regions exhibit nanoscale precipitates likely to be $L1_2$ and B2, respectively. To confirm the phases present in the microstructure, EBSD scans were performed, and the resultant IPF and phase maps are shown in Figure 11(a) and Figure 11(b), respectively. The phase map confirms the presence of FCC and BCC phases in the microstructure. However, the nanoscale precipitates within these regions are (i) too fine to be resolved by SEM-EBSD and (ii) EBSD cannot distinguish between FCC/$L1_2$ and BCC/B2 because of the similarities in lattice structures. However, similar microstructures have been observed in the SLM- and DED-processed specimens of the same HEA (Figure 4), where the presence of B2 in the BCC phase and $L1_2$ in the FCC phase has been established via transmission electron microscopy (TEM) [29, 219].

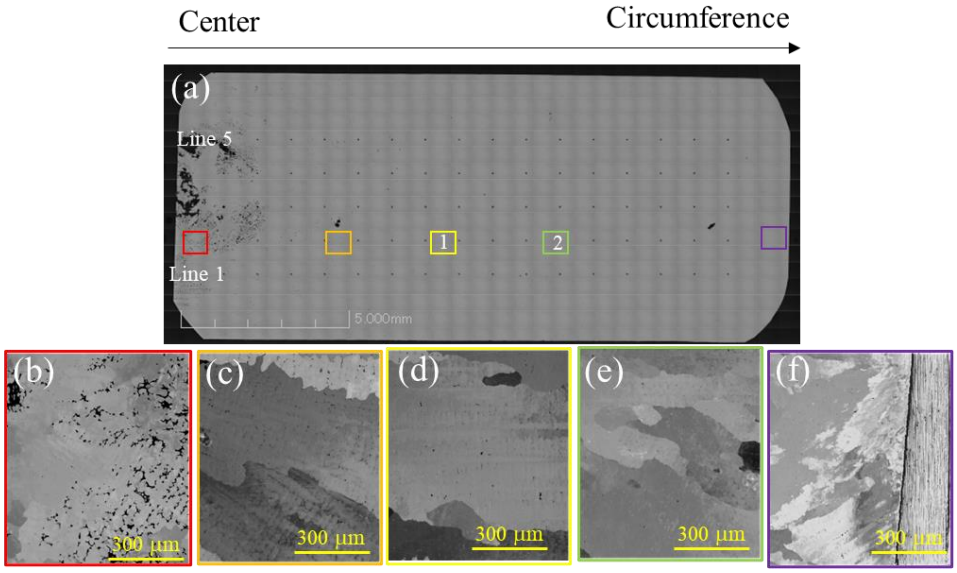

Figure 9. (a) Optical image and (b–f) SEM backscatter images revealing the microstructure of the AR $Al_{0.3}Ti_{0.2}Co_{0.7}CrFeNi_{1.7}$ HEA along the radial direction.

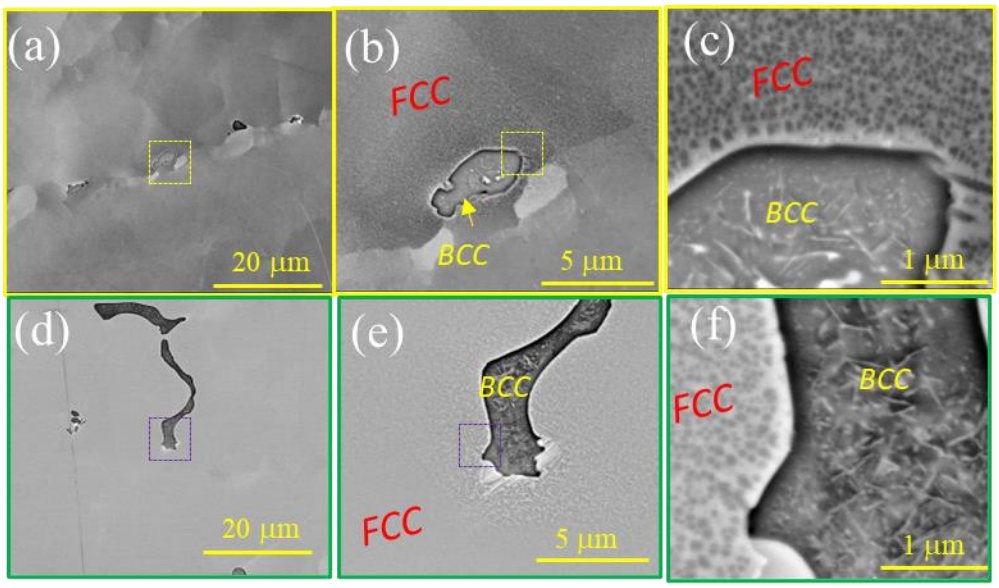

Figure 10. High-magnification SEM backscatter images obtained from (a–c) Region 1 and (d–f) Region 2 in Figure 9(a).

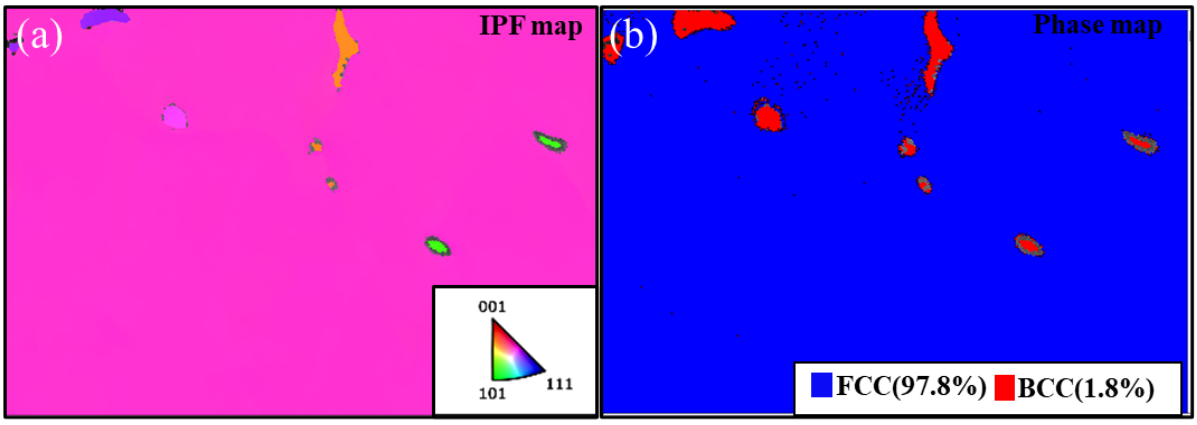

Figure 11. (a) IPF and (b) phase map obtained from an AR specimen of the $Al_{0.3}Ti_{0.2}Co_{0.7}CrFeNi_{1.7}$ HEA.

Microhardness measurements were carried out along the radial direction of the AR cylindrical bars of the HEA. The hardness values corresponding to the indents observed in Figure 9(a) are plotted in Figure 12. The hardness appears to not change spatially, indicating an identical microstructure throughout the specimen. The average hardness of the HEA in the AR condition is measured to be 352 HV.

We identified three key parameters that determine FSLD quality: rotation rate, traverse speed, and forging force. To optimize the deposition process, we varied these parameters systematically. To expedite parameter development, we tested two sets of parameters for each friction surfacing run. The specific parameters are detailed in Table 10. Additionally, critical machine data—including the forging force, rotation rate, traverse velocity, and torque—were recorded and are presented in Figure 13.

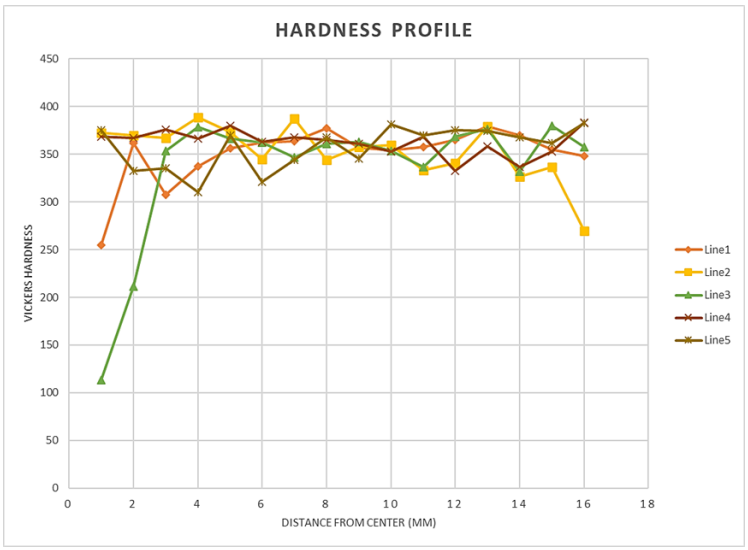

Figure 12. Hardness values plotted along the radial direction of the AR HEA.

Table 10. Critical parameters for the FSLD runs conducted in this study.

Run #	*Traverse RPM*	*Traverse Rate (mm/min)*	*Force (kN)*
2024-04-25-0004	500	100; 200	25
2024-04-25-0005	750	100	45; 70
2024-04-25-0006	750	100	70; 95
2024-04-25-0007	500; 350	100	75

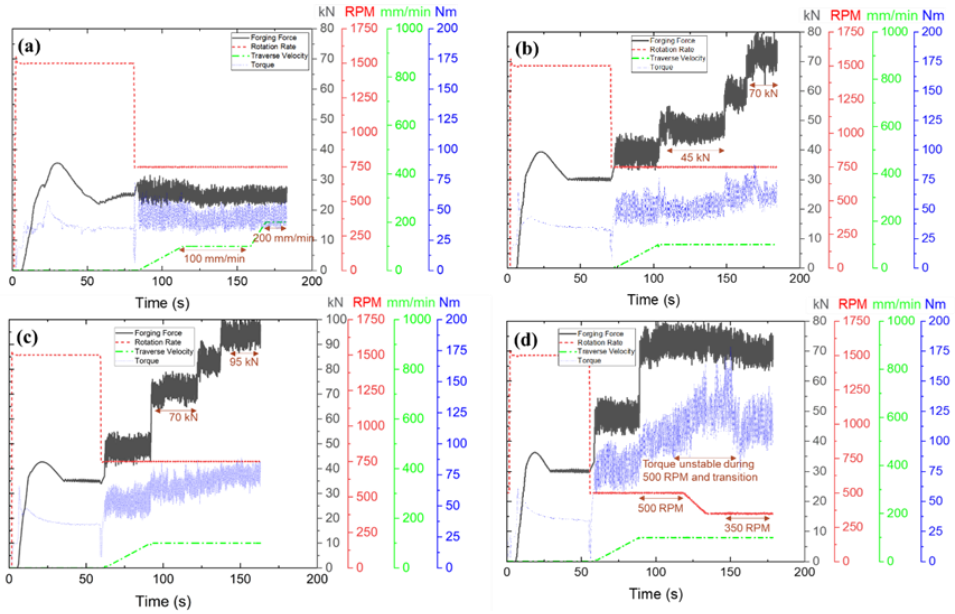

Figure 13. Machine data for various FSLD processes for Run Numbers (a) 2024-04-25-0004, (b) 2024-04-25-0005, (c) 2024-04-25-0006, and (d) 2024-04-25-0007.

Figure 14 displays the surface appearance for each run. It reveals that various defects, such as narrow tracks, thin deposition, and surface imperfections, occur when the parameters are not optimized. The process parameters and associated defects are summarized in Table 11. Notably, a lower rotation rate appears to be beneficial for the deposition process. Additionally, cross sections of selected specimens processed with the conditions in Table 11 highlight the defects of narrow tracks and thin deposition, as shown in Figure 15.

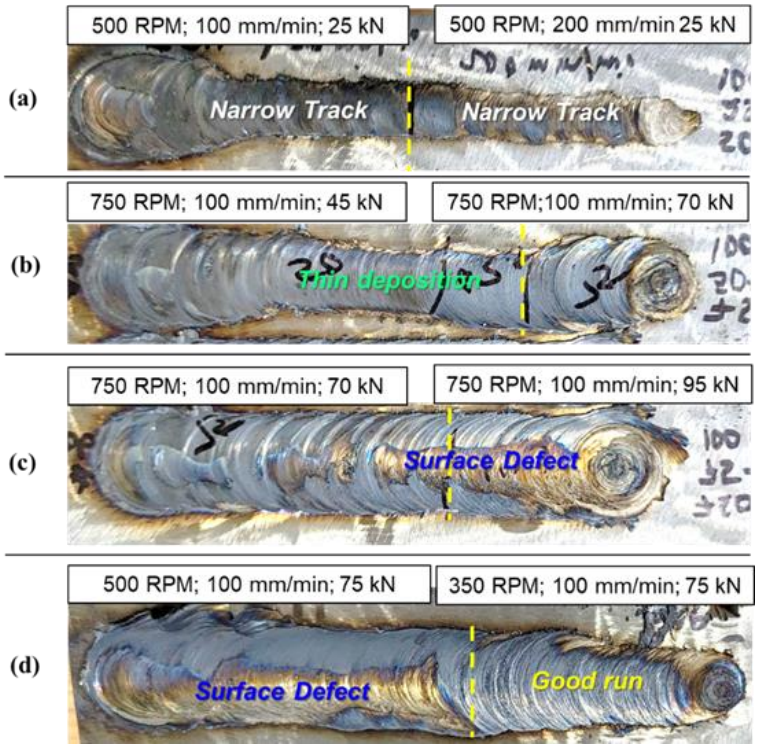

Figure 14. Appearance of the surfaces of FSLD-processed specimens for Run Numbers (a) 2024-04-25-0004, (b) 2024-04-25-0005, (c) 2024-04-25-0006, and (d) 2024-04-25-0007.

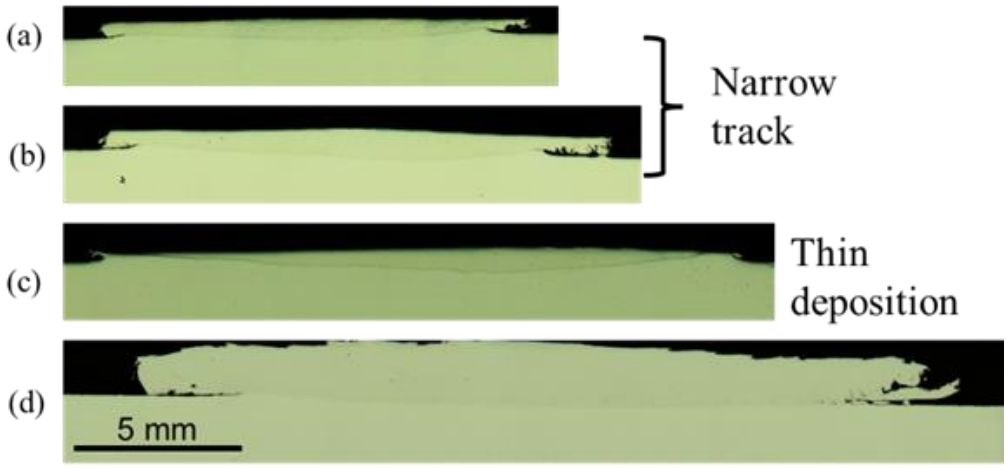

Figure 15. Cross-section OM images: (a) Condition 2, (b) Condition 1, (c) Condition 3, and (d) Condition 8.

Table 11. Critical parameters for the runs conducted in this study and their related defects.

Run #	*Condition*	*Traverse RPM*	*Traverse Rate (mm/min)*	*Force (kN)*	*Defect type*
2024-04-25-0004	1	500	100	25	Narrow track
	2	500	200	25	
2024-04-25-0005	3	750	100	45	Thin deposition
	4	750	100	70	
2024-04-25-0006	5	750	100	70	Surface defect
	6	750	100	95	
2024-04-25-0006	7	500	100	75	
	8	350	100	75	No defects

Among the different processing conditions, Condition 8 resulted in a nearly perfect deposit without any defects; hence, SEM characterization was performed to evaluate the change in the microstructure due to FSLD processing. The SEM backscatter images for Condition 8 are presented in Figure 16. Several cracks are observed along with presence of oxide-like particles at the substrate–HEA interface. Unlike the bottom, the number density of oxide particles significantly increases in the top region. The middle region of the deposit appears to be clear of any defects or oxides. The overall microstructure of the FSLD deposit appears to be significantly refined because the average grain size due to FSLD processing is lower than 2 µm. Furthermore, the multiphase (FCC+$L1_2$+BCC+B2) microstructure of the AR specimen appears to be completely transformed to a single-phase FCC microstructure. However, nanoscale precipitates of $L1_2$ phase that are too fine to be resolved by SEM may be present in the FCC phase. Only a TEM analysis needs to be performed to validate the same. The average hardness of the middle region of the deposit is measured to be 327 HV. It must be noted that the AR HEA comprising a multiphase microstructure is 352 HV. The FSLD-processed specimen, despite its nearly single-phase microstructure, has a marginally lower hardness. This emphasizes the impact of grain refinement facilitated by FSLD processing on the mechanical properties. A post-heat-treatment to precipitate the $L1_2$ phase can significantly enhance the mechanical properties of the FSLD-processed HEA.

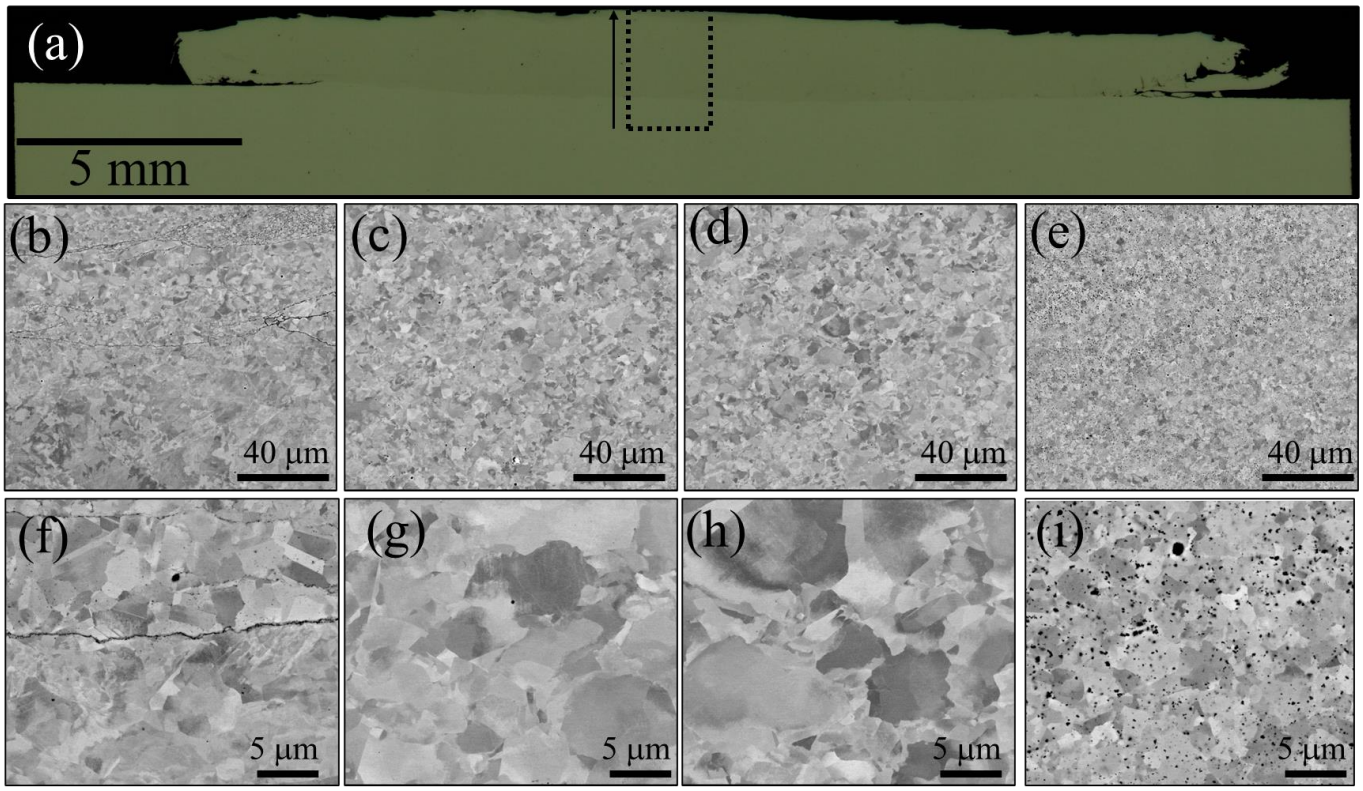

Figure 16. (a) Optical image of the transverse section of an FSLD-processed HEA for Condition 8. (b–e) Low- and (f–g) high-magnification SEM backscatter images obtained along the build height from the region marked in (a).

4.1.4 Summary

In summary, the temperature-dependent (from RT to 500°C) nanoindentation behavior of the DED- and SLM-processed $Al_{0.3}Ti_{0.2}Co_{0.7}CrFeNi_{1.7}$ HEA was investigated in the AD and one-step annealed conditions in this study. The hierarchically heterogeneous microstructures obtained via simple one-step annealing of the DED- and SLM-processed HEA exhibited significantly better performance than the nearly homogeneous microstructures in the AD state. The one-step annealed specimens revealed a less than 6.6% reduction in hardness at 500°C compared to that at RT, while the AD specimens showed a greater than 18% reduction in hardness between RT and 500°C. The one-step annealed specimens also exhibited a significantly higher hardness than the AD specimens owing to their multiphase (FCC+$L1_2$) microstructures with a substantial fraction of ordered $L1_2$ precipitates. Furthermore, serrated yielding (PLC effect) indicative of microstructural instability was observed during nanoindentation deformation (at 500°C) for both SLM- and DED-processed specimens but not after one-step annealing. Overall, the nanoindentation results demonstrate the stability of these hierarchically heterogeneous microstructures developed via single-step annealing, exploiting the residual stresses in the AM-processed $Al_{0.3}Ti_{0.2}Co_{0.7}CrFeNi_{1.7}$ HEA.

In contrast, FSLD processing of this HEA was challenging because of its multiphase microstructure in the AR state. Hence, a meticulous process parameter optimization study was performed. Further, detailed microstructural characterization using SEM was carried out to analyze the differences in the microstructure due to FSLD processing. FSLD processing led to homogenization of this HEA, resulting in the formation of a single-phase FCC microstructure.

Despite the single-phase character, the FSLD-processed HEA exhibited a significantly high hardness of 325 HV, providing scope for further enhancement of the hardness via heat treatments and process parameter optimization.

The results presented in this study indicate strong potential for applications of this HEA in high-temperature nuclear reactors.

4.2 Down-Selected HEA: $Al_{10}Cr_{12}Fe_{35}Mn_{23}Ni_{20}$

4.2.1 Background and Summary of Experimental Work

According to an NRC report titled “Use of High Entropy Alloys (HEAs) in Future Nuclear Applications” published in January 2023, three HEAs ($Al_{0.3}Cu_{0.5}CrFeNi_2$, $Al_5Cr_{12}Fe_{35}Mn_{28}Ni_{20}$, and $Al_{10}Cr_{12}Fe_{35}Mn_{23}Ni_{20}$) exhibited enhanced structural and functional properties over the code certified materials. Further, the report identifies AlCuCrFeNi and AlCrFeMnNi HEAs as compositional areas of interest for future studies. Among these three HEAs, $Al_{10}Cr_{12}Fe_{35}Mn_{23}Ni_{20}$ has the highest YS and ultimate tensile strength (UTS) and therefore has been chosen for experimental work in the current work package. A manuscript titled “Additive Friction Surface Layering of Triple-Phase $Al_{10}Cr_{12}Fe_{35}Mn_{23}Ni_{20}$ High Entropy Alloy: Microstructural Evolution and Process Optimization” has been prepared for submission to the journal *Additive Manufacturing*. A summary of the experimental findings from this study is as follows.

Cast rods of this HEA were procured from Sophisticated Alloys, Inc., and FSLD processing was performed to produce single and multilayer deposits. A detailed process parameter–property optimization study was performed by depositing several single layers of this HEA by varying the forging force (*F*) and traverse speed (*Tr*). Further, a multilayer deposit was successfully fabricated using the optimized processing conditions (*F* = 40 kN, *Tr* = 200 mm/min), demonstrating the potential for FSLD to fabricate tall specimens. A detailed microstructural evaluation of AR and FSLD-processed specimens was carried out using SEM, EBSD, EDS, and TEM. The AR HEA exhibited a coarser triple-phase FCC+BCC+B2 microstructure with a soft FCC matrix phase, a hard BCC dendritic phase, and a harder B2 phase as precipitates within the hard BCC dendrites. Thus, all three phases pursued drastically different microstructural evolution pathways during FSLD processing. The FCC matrix underwent continuous dynamic recrystallization, forming finer equiaxed grains due to shearing deformation. At the same time, the BCC dendrites fractured into several finer fragments, and in some regions, these BCC fragments tended to grow, changing their morphology from arbitrary to hourglass-like. Among the three phases, B2 is the only phase that likely dissolved during processing and reprecipitated as finer precipitates in the BCC fragments during continuous cooling post-FSLD. In the manuscript, these complex mechanisms are clearly illustrated using a schematic. The microstructure of the triple-phase HEA changed significantly with the changes in the processing conditions, providing scope for tuning the process parameters further to attain desired microstructures and mechanical properties.

To conclude, in addition to the significant enhancement in the hardness (from 177 HV to 278 HV), FSLD processing also led to substantially finer grains/precipitates, which increase the number of interfaces, potentially enhancing the sink strength of this HEA, making it an ideal candidate for future nuclear applications.

4.3 Graded High Entropy Alloys

4.3.1 Background

In nuclear reactor environments, where the materials are subjected to thermal and mechanical stresses, corrosion, diffusion and irradiation, the development of advanced coatings may prevent these materials from these degradation mechanisms. Novel materials and the associated advanced manufacturing techniques for coatings along with advanced characterization are required for improving the performance of these coatings. FeCoCrNi-based HEAs can present a single-phase FCC structure that demonstrates superior irradiation resistance compared to multiphase and BCC structures. Previous studies have revealed that there are significant challenges in manufacturing single-phase HEAs with conventional casting methods.

This work utilizes DED AM as a development technology for coating materials that allows the fabrication of graded HEAs. LENS DED is uniquely suited to tailor material properties and compositions to a specific application and features high control over the processing parameters that allows for microstructural and as-built optimization. The DED method can control the flow of powders during fabrication, resulting in a component with a gradual variation of chemistry along the build direction, i.e., a compositionally graded material. This compositional variation also alters the inherent microstructure with changes in the phase fraction, mechanical properties, etc. Hence, properly designed coatings that benefit from the spatial variation in properties can be developed.

4.3.2 Materials and Methods

The compositionally graded HEA was fabricated using the DED method in an Optomec® LENS MR-7 system at Idaho National Laboratory (INL) as part of an INL Laboratory Directed Research and Development (LDRD) program (2019-2021). The three alloy powders for mixing were 70Co30Cr (commercially known as Stellite 21), 316L SS, and IN 718 alloy, and specimens with 10 layers of compositions were fabricated to create graded materials.

In INL's LDRD program, the microstructures of graded sections of materials were characterized using SEM, and compositional changes across the build were determined using EDS [226]. Nanoindentation was performed across the build direction to identify trends along complex sample compositions. Bulk cross sections were assessed for successful fusion and lack of macroscopic defects (unmelted particles, separation of layers, etc.) [227]. However, microscopic inhomogeneous regions including unmelted powders and agglomerated elements (e.g., CoCr) were observed in optical and SEM images. The motivation of this work is to understand the details of such regions and adjacent HEA regions using TEM. A thorough understanding of the chemistry of such regions and the formation mechanisms will help to optimize printing parameters (adjust hatch spacing, energy density, potentially dynamic process parameter adjustment) to increase homogeneity and performance [228].

A Helios Hydra Plasma focused ion beam (FIB) was used to prepare the TEM lamella. A JEOL Grand Arm scanning transmission electron microscope with a Schottky FEG operating at 300 keV was used for nanoscale characterization of samples' microstructures. High-angle annular dark-field TEM/scanning TEM (STEM) imaging was used to analyze the samples. High-resolution elemental maps were also acquired using X-ray energy dispersive spectrometry in the STEM mode.

4.3.3 Results and Discussion

Figure 17(a) shows a schematic of the graded HEA sample fabricated by DED using three different off-the-shelf powders on 316L alloy substate. The schematic shows the build layers with thicknesses in the range of 0.3–0.5 mm. The contents of the CoCr, IN 718, and 316L powders vary along the build direction with each layer. Figure 17(b) shows a photograph of the graded sample on the top of the substrate, as marked by the yellow dashed line. Figure 17(c) shows an optical image of the substrate and the graded material, and the layers of deposition are visible by the image contrast. Microscopic pores that are commonly observed in AM materials are also visible. Figure 17(d) shows the chemical maps generated by EDS during SEM that clearly show the compositional variations of the primary elements—Fe, Co, and Cr—along the build direction. Figure 17(e) shows an enlarged optical image of the region marked in the fifth box of Figure 17(c). This area contains a possibly unmelted agglomeration of an Fe-rich region. Further, a TEM lamella was prepared in the region indicated by the green box for nanoscale analysis of the interface of the HEA and the unmelted region.

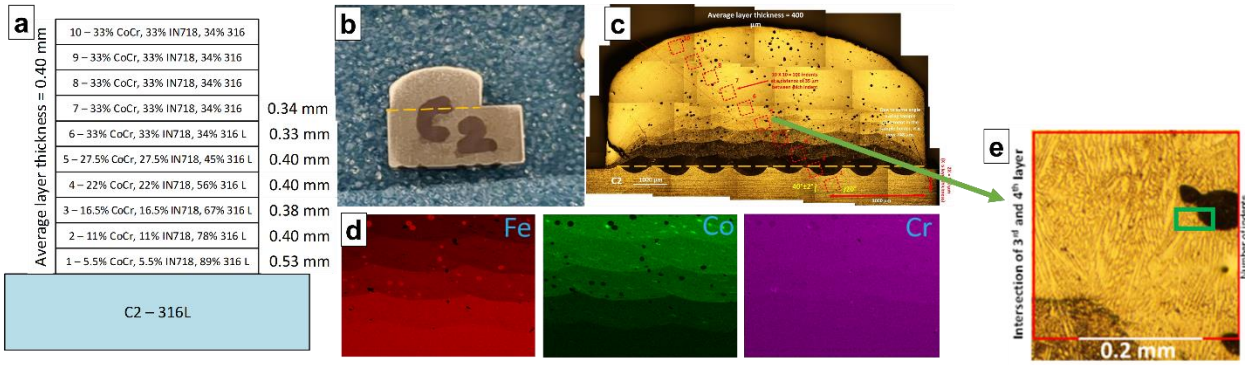

Figure 17. (a) Schematic of the compositionally graded HEA on a 316L substrate using DED; (b) fabricated graded material on the substrate, marked by the yellow dashed line; (c) optical image of the graded material; (d) SEM images showing the continuous variation of Fe, Co, and Cr with deposition thickness; and (e) enlarged optical image showing the area of interest and the region marked as “5” in (c). The approximate area of the TEM lift-out has been marked in the green box.

Figure 18(a) shows the pre-final FIB lift-out, where the interface between the unmelted region and the HEA region is clearly visible and has been marked by the red dashed line. Figure 18(b) shows an STEM image of the region where the small precipitates on both sides of interface are visible. Figure 18(c) shows the chemical map generated by EDS during TEM that clearly shows the Co compositional variation across these two regions. Apart from Co, Fe appears to be higher in the unmelted region. Thus, it is possible that it can be unmelted 316L powder. Similarly, Figure 18(d–g) show the chemical maps of Fe, Ti, Cr, and Ni respectively. One of the precipitates in the HEA region has been identified as Ti-rich in Figure 18(e), while the unmelted part has Cr-rich precipitates in Figure 18(f).

Figure 19 focuses on the HEA region to highlight the chemistry of the precipitate phase. The precipitate on the HEA side is further studied and was identified as Ti oxide based on the strong presence of Ti and O, as shown in Figure 19(c–d). Ti has been reported to form oxides readily during powder processing. However, whether the oxide was already present in the powder used or formed during processing has not been determined. Only one oxide particles is observed in

the TEM lamella, so it can be believed that the volume fraction of such oxide inclusions is very low.

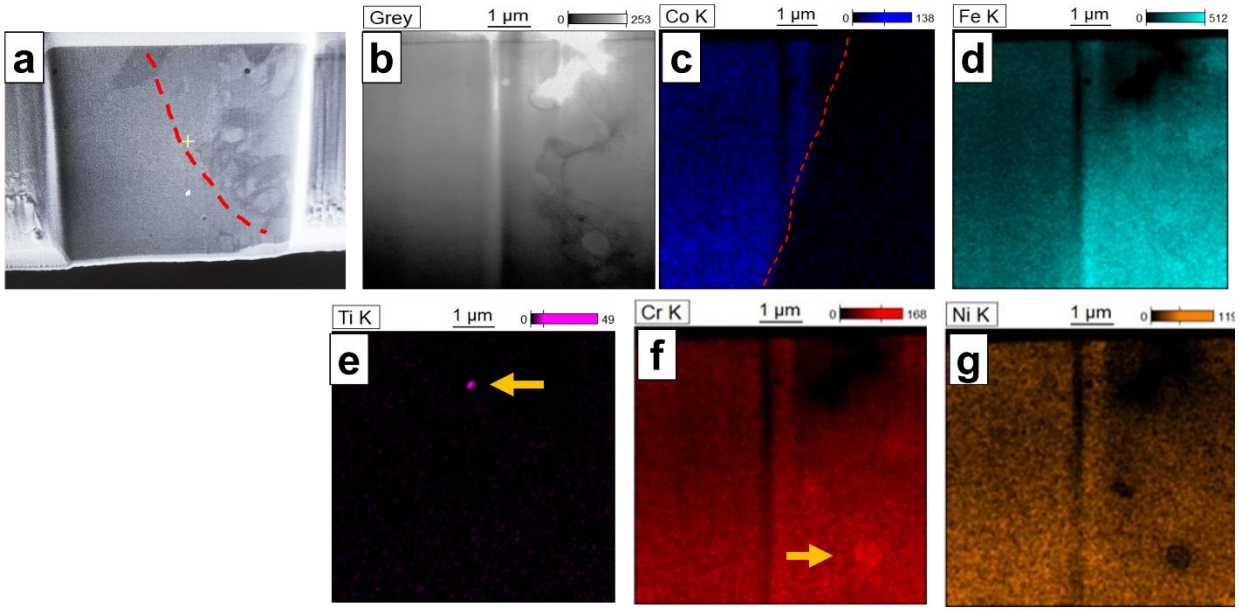

Figure 18. (a) FIB lift-out showing the area of interest and the unmelted steel powder on the left side, (b) STEM image showing the same area of interest with the interface between the HEA and the unmelted steel powder particle, and (c) Co elemental map showing the interface between the two phases. The Ti map in (e) shows the Ti-rich region in the HEA region, and (f) shows the Cr-rich region in the unmelted steel powder particle.

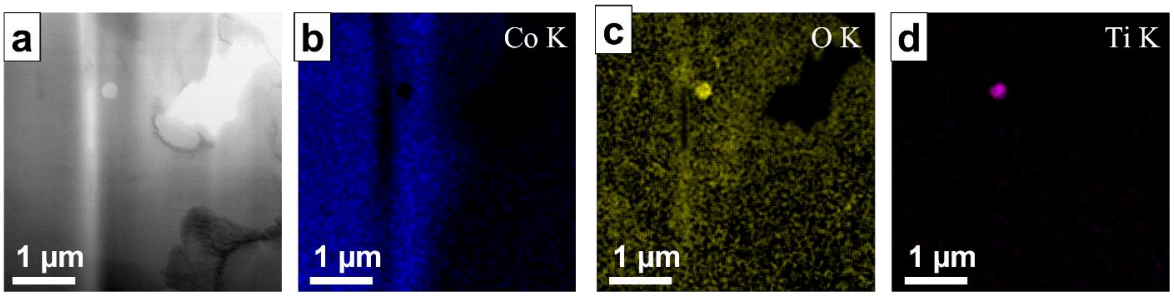

Figure 19. (a) STEM image showing the morphology of the Ti oxide precipitate in the HEA region. The chemical maps of the HEA region highlight the presence of Ti and O in the form of precipitates in (b–d).

Similarly, Figure 20 shows the unmelted region that was analyzed to identify the composition of the precipitates present in this region. Figure 20(a) shows a spherical precipitate, and Figure 20(b–e) show chemical maps of the region. The precipitate appears to be strongly rich in Cr.

Figure 21(a) shows an SEM image of the HEA region that shows the formation of dendritic and interdendritic regions during the solidification process. The interdendritic regions appear to be mostly a continuous channel, but there are some regions where they appear to be discontinuous. This is possibly due to the projection of the interdendritic channels running within the sample, which are not captured in these two-dimensional images. The same dendritic and

interdendritic regions have been observed in the HEA region during TEM, as shown in Figure 21(b). The chemical maps in Figure 21(c–g) show that the interdendritic regions are mostly enriched with Nb. This also corresponds to the brighter chemical contrast of interdendritic regions, as seen in Figure 21(a).

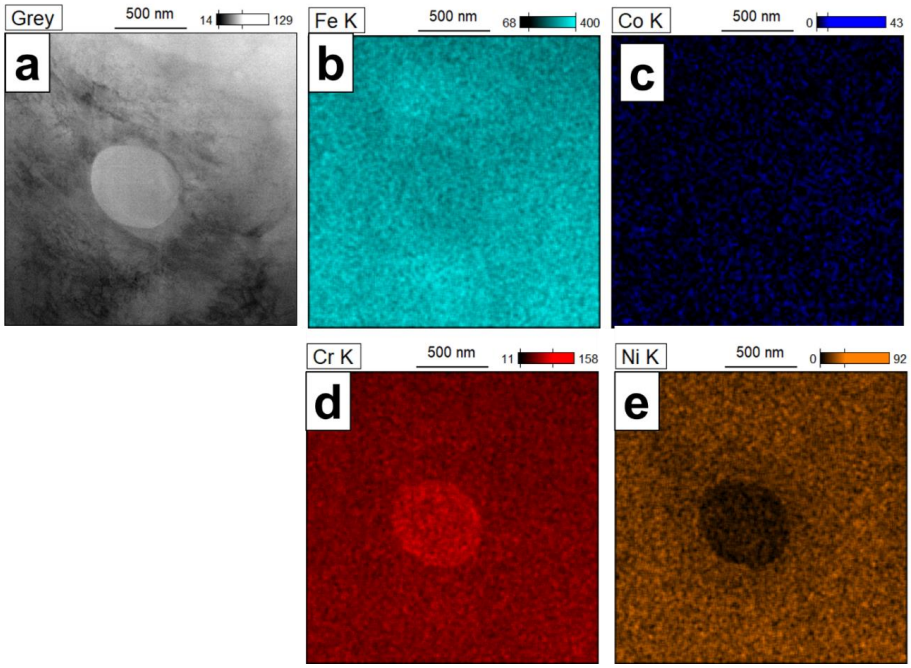

Figure 20. (a) STEM image showing the morphology of the Cr-rich particle in the unmelted steel. (b–d) Elemental distributions in the Cr-rich region.

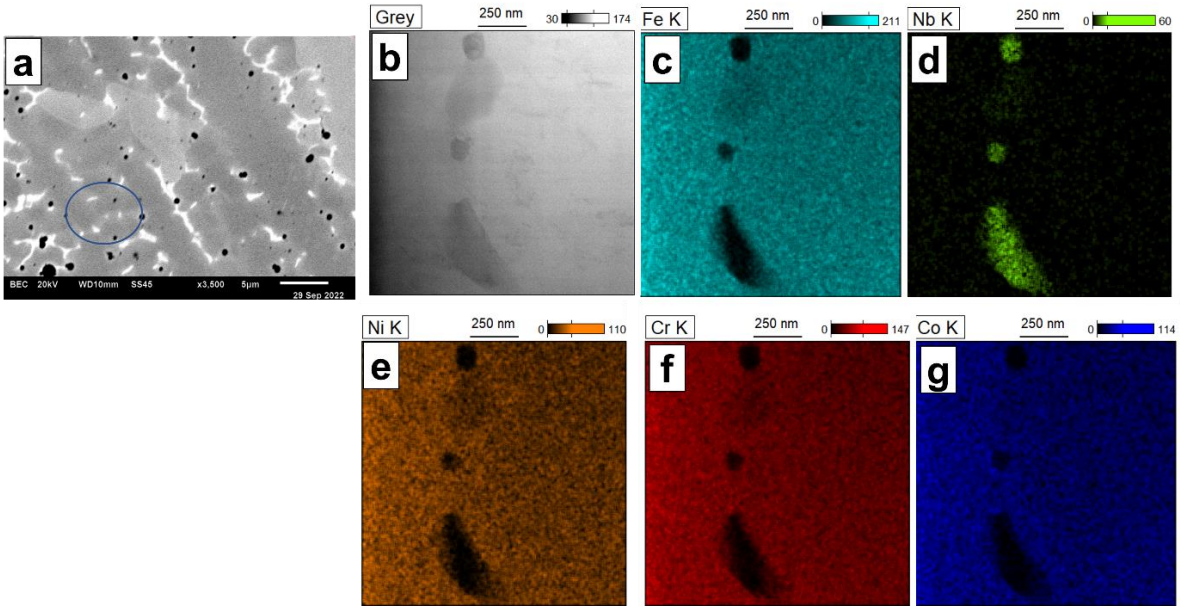

Figure 21. (a–b) SEM and STEM images showing the dendritic and interdendritic region formation in the HEA region. (c–g) Chemical maps obtained with STEM-EDS showing the strong presence of Nb and the absence of Fe, Ni, Cr, and Co in the interdendritic regions.

4.3.4 Summary

Novel DED-fabricated HEAs with graded compositions using off-the-shelf common alloy powders has been studied using advanced microscopy. The main findings are as follows:

a) The composition in each build layer appears to be quite homogeneous. The HEA seems to form dendritic and interdendritic regions mainly due to the presence of certain elements, such as Nb.

b) The HEA still contains some unmelted powders, possibly 316L. The unmelted region has been examined, and it contained nanoscale Cr-rich precipitates.

c) The HEA region also contains a small fraction of Ti oxide precipitates.

Although a microstructural examination confirms the successful fabrication of graded materials, further optimization of the process parameters is needed to reduce the porosity in the microstructure and undesired brittle intermetallic phases.

5.0 Research Outcomes

- The work performed under this work package has been presented in talks at the following conferences:
  - International Conference on Additive Manufacturing (ICAM) 2023, Washington, DC, October 30–November 3, 2023
    - Mohan Sai Kiran Kumar Yadav Nartu, Isabella van Rooyen, Rajarshi Banerjee, HEAs for Nuclear Energy Applications and Potential Advanced Manufacturing Methods
  - 3rd World Congress on High Entropy Alloys (HEA 2023), Pittsburgh, PA, November 12–15, 2023
    - Subhashish Meher, Mohan Nartu, Chinthaka Silva, Isabella van Rooyen, Calvin Downey, Luis Nunez, Michael Maughan, Yogesh Sighla, Development of High Entropy Alloy Based Coatings via Directed Energy Deposition (DED) Additive Manufacturing for Nuclear Applications
  - Materials in Nuclear Energy Systems (MiNES 2023), New Orleans, LA, December 10–14, 2023
    - Mohan Sai Kiran Kumar Yadav Nartu, Isabella van Rooyen, Shristy Jha, Advika Chesetti, Sundeep Mukherjee, Rajarshi Banerjee, Engineering Heterogeneous Microstructures in Additively Manufactured $Al_{0.3}Ti_{0.2}Co_{0.7}CrFeNi_{1.7}$ High Entropy Alloy for Potential Nuclear Applications
- **Publications:**
  - Mohan Sai Kiran Kumar Yadav Nartu, Shristy Jha, Advika Chesetti, Sundeep Mukherjee, Isabella van Rooyen, and Rajarshi Banerjee, Microstructure and Temperature Dependent Indentation Response of Additively Manufactured Precipitation-Strengthened Al0.3Ti0.2Co0.7CrFeNi1.7 High Entropy Alloy, TMS journal *JOM*, December 2023 edition
  - Mohan Sai Kiran Kumar Yadav Nartu, David Garcia, Subhashish Meher, Tianhao Wang, Jorge F Dos Santos, and Isabella van Rooyen, Additive Friction Surface Layering of Triple-Phase Al10Cr12Fe35Mn23Ni20 High Entropy Alloy: Microstructural Evolution and Process Optimization, Submitted to journal *Additive Manufacturing.*
  - Calvin M. Downey, Luis Nuñez III, Yogesh Singla, Subhashish Meher, Chinthaka Silva, Michael Maughan, Isabella J. van Rooyen, Indrajit Charit, Fabrication and Characterization of Powder DED Additive Manufactured CoCrFeNi Multi-principal Element Alloy Utilizing Commercial Alloys, To be submitted to *Journal of Materials Processing*

6.0 Preliminary Decision Matrix Ratings of the Two Down-Selected HEAs

Based on the literature review, the preliminary experiments performed, and engineering rationale, a preliminary rating of the two down-selected alloys was performed and is summarized in Table 12 with the associated justification below in the text. The $Al_{10}Cr_{12}Fe_{35}Mn_{23}Ni_{20}$ HEA performed marginally better than the $Al_{0.3}Ti_{0.2}Co_{0.7}CrFeNi_{1.7}$ HEA, with a rating of 63 versus 55.5.

Table 12. Preliminary decision matrix ratings.

	Criteria	$Al_{0.3}Ti_{0.2}Co_{0.7}CrFeNi_{1.7}$	$Al_{10}Cr_{12}Fe_{35}Mn_{23}Ni_{20}$
Application Space	Applicability to Different Reactor Types	3	5
	Other Industry Experience	3	3
	Data Availability	0	0
	Code & Standards Availability	0	0
	Component Versatility	2	2
Environmental Compatibility	Radiation Resistance	0	0
	Elemental Transmutation	0	0
	High-Temperature Oxidation Resistance	0	0
	Neutronics Compatibility	0	0
	Coolant Compatibility & Corrosion Resistance	0	0
Physical & Mechanical Properties	Thermal Conductivity	0	0
	Thermal Capacity	0	0
	Tensile Properties	5	5
	Creep Performance	0	0
	Fatigue	0	0
	Fracture Toughness	0	3
	Microstructural Dependency	5	5
	Scope for Microstructural Enhancement	5	5
Manufacturability	Reproducibility/Consistency	4	4
	Process Complexity	3.5	4
	Cost	3	3
	Scalability	5	5
	Production Method TRL	1	1
	Raw Material Supply	3	5

Criteria	$Al_{0.3}Ti_{0.2}Co_{0.7}CrFeNi_{1.7}$	$Al_{10}Cr_{12}Fe_{35}Mn_{23}Ni_{20}$
Flexibility of Manufacturing	5	5
Conventional Machining	3	3
Near Net Shaping (Complexity of Shape)	5	5
Overall Scores	55.5	63

6.1 Justification of Ratings

6.1.1 $Al_{0.3}Ti_{0.2}Co_{0.7}CrFeNi_{1.7}$

The $Al_{0.3}Ti_{0.2}Co_{0.7}CrFeNi_{1.7}$ HEA was given a score of 55.5 out of a possible 135 based on the decision criteria matrix. Most of the criteria scored "0," as this HEA is recently developed and has no data reported for those criteria. However, some of the criteria have been assigned a score based on the limited data available in the literature. The justification for the assigned scores is provided below.

Applicability to Different Reactor Types (3/5)

The mechanical and functional properties of the $Al_{0.3}Ti_{0.2}Co_{0.7}CrFeNi_{1.7}$ HEA can be significantly tuned to withstand the environments in several reactors. Moreover, this HEA is believed to retain its structural integrity up to 1100°C. Since there is no experimental data available on the application of this HEA in any reactors yet, a score of 3 can been assigned based on intuition.

Other Industry Experience (3/5)

HEAs are typically suitable for structural applications; hence, widespread use in various other industries is envisaged. Since there are no reports investigating the other industry applications, a score of 3 has been assigned.

Component Versatility (2/5)

This HEA has application as a fuel cladding material requiring good structural integrity. Other applications may be possible after determining this HEA's properties such as corrosion, irradiation resistance, etc. Therefore, only a score of 2 has been assigned.

Tensile Properties (5/5)

This HEA is reported to exhibit a yield strength of ~1630 MPa and a good tensile ductility of ~15% at RT, which are significantly higher than most SSs. This HEA is expected to have high-temperature stability up to ~1100°C; hence, a score of 5 has been assigned for the tensile properties.

Microstructural Dependency (5/5)

The mechanical and functional properties of this HEA are greatly dependent on the underlying microstructure; therefore, a score of 5 has been assigned.

Scope for Microstructural Enhancement (5/5)

Since this HEA's properties can be significantly tuned, a score of 5 has been assigned.

Reproducibility/Consistency (4/5)

This HEA has only been manufactured via casting, DED, SLM, and FSLD so far. Although Casting is highly reproducible and consistent, the other three AM techniques may not be and need further validation. Therefore, a score of 4 has been assigned.

Process Complexity (3.5/5)

This HEA can be easily manufactured via casting or AM. Laser AM involves a preprocessing step to produce good quality spherical powders, which are chiefly made via an atomization process. Moreover, this HEA is challenges to process via FSLD because of its multiphase microstructure. Therefore, a score of 3.5 is assigned.

Cost (3/5)

Since this HEA is not commercially produced yet, a score of 3 has been assigned, as the cost would be comparable to any SSs produced commercially today.

Scalability (5/5)

The scalability for this HEA is only limited by the type of processing technique employed, and no specific issues pertaining to its composition are foreseen; therefore, a score of 5 can be assigned.

Production Level TRL (1/5)

This HEA is not yet commercially produced, and only a handful of research articles can be found. Therefore, a score of 1 has been assigned.

Raw Material Supply (3/5)

The raw material supply for casting this HEA should be no different from any SS. However, for AM, the availability of HEA powders can be highly challenging. Therefore, a score of 3 has been assigned.

Flexibility of Manufacturing (5/5)

This HEA can be manufactured via all bulk manufacturing techniques; hence, a score of 5 has been assigned.

Conventional Machining (3/5)

A part manufactured via casting requires significant post-processing but only requires minimal post processing when fabricated via AM. Therefore, an average score of 3 has been assigned.

Near Net Shaping (Complexity of Shape) (5/5)

The fabrication of this HEA is not limited by the complexity of the design.

6.1.2 $Al_{10}Cr_{12}Fe_{35}Mn_{23}Ni_{20}$

The $Al_{10}Cr_{12}Fe_{35}Mn_{23}Ni_{20}$ HEA was given a score of 63 out of a possible 135 based on the decision criteria matrix. Most of criteria scored "0," as this HEA is recently developed and has no data reported for those criteria. However, some of the criteria have been assigned a score based on the limited data available in the literature. The justification for the assigned scores is provided below.

Applicability to Different Reactor Types (5/5)

The $Al_{10}Cr_{12}Fe_{35}Mn_{23}Ni_{20}$ HEA is free from cobalt; moreover, the properties can be greatly tuned to withstand the environments in several reactors. Although there are no experimental data available on the application of this HEA in any reactors yet, the NRC report strongly recommends this HEA for future nuclear applications because of its enhanced mechanical properties and microstructural benefits; therefore, a score of 5 has been assigned.

Other Industry Experience (3/5)

HEAs are typically suitable for structural applications; hence, widespread use in various other industries is envisaged. Since there are no reports investigating other industry applications for this HEA, a score of 3 has been assigned.

Component Versatility (2/5)

This HEA has application as a fuel cladding material requiring good structural integrity. Other applications may be possible after determining this HEA's properties such as corrosion, irradiation resistance, etc. Therefore, only a score of 2 has been assigned.

Tensile Properties (5/5)

In the cold-rolled state, this HEA is reported to exhibit a yield strength of ~1400 MPa and a decent tensile ductility of ~5.83% at room temperature, which are significantly higher than most code-certified materials. Hence, a score of 5 has been assigned for the tensile properties.

Fracture Toughness (3/5)

The fracture toughness of this HEA in the cold-rolled state is ~79 MPa$\sqrt{m}$, which is slightly lower than other code-certified materials; therefore, a score of 3 has been assigned.

Microstructural Dependency (5/5)

The mechanical and functional properties of this HEA are greatly dependent on the underlying microstructure; therefore, a score of 5 has been assigned.

Scope for Microstructural Enhancement (5/5)

Since this HEA's properties can be significantly tuned, a score of 5 has been assigned.

Reproducibility/Consistency (4/5)

This HEA has been manufactured via casting and FSLD. While casting is highly reproducible and consistent, FSLD processing with some process-parameter optimization was also largely

successful. However, because of the requirement of process optimization for bulk manufacturing methods such as FSLD, a score of 4 has been assigned.

Process Complexity (4/5)

This HEA can be easily manufactured via casting without any preprocessing required. The FSLD processing conducted as a part of this study also showed promising results, albeit with some process parameter optimization. Therefore, a score of 4 is assigned.

Cost (3/5)

Since this HEA is not commercially produced yet, a score of 3 has been assigned, as the cost would be comparable to any SS produced commercially today.

Scalability (5/5)

The scalability for this HEA is only limited by the type of processing technique employed, and no specific issues pertaining to its composition are foreseen; therefore, a score of 5 can be assigned.

Production Level TRL (1/5)

This HEA is not yet commercially produced, and only a handful of research articles can be found. Therefore, a score of 1 has been assigned.

Raw Material Supply (5/5)

The raw material supply for casting of this HEA should be no different from any SS. Therefore, a score of 5 has been assigned.

Flexibility of Manufacturing (5/5)

This HEA can be manufactured via all bulk manufacturing techniques; hence, a score of 5 has been assigned.

Conventional Machining (3/5)

A part manufactured via casting requires significant post-processing but only requires minimal post-processing when fabricated via AM. Therefore, an average score of 3 has been assigned.

Near Net Shaping (Complexity of Shape) (5/5)

The fabrication of this HEA is not limited by the complexity of the design.

7.0 Conclusion and Recommendations

The HEA classification used in this review and the elaborate literature survey presented in this report provide insights into the processing, microstructure, and properties of several reported HEAs targeting different applications. Based on the literature survey, six HEAs were identified as promising for the nuclear industry, focusing on high-temperature properties, with Co as an alloying element in two of these alloys [$(Ni_2Co_2FeCr)_{92}Al_4Nb_4$, $Al_{0.3}Ti_{0.2}Co_{0.7}CrFeNi_{1.7}$]. GRX-810, developed by NASA, shows creep performance 2–3 orders of magnitude better than that of the current high-temperature alloys and is best classified as a medium entropy alloy or an ODS alloy because of the presence of Y_2O_3 particles; therefore, we recommend pursuing this material as part of a different AMMT work package. Although the decision matrix is not yet fully developed for the six candidate HEAs, the literature survey provides technical justification to down-select two HEAs ($Al_{0.3}Ti_{0.2}Co_{0.7}CrFeNi_{1.7}$ and $Al_{10}Cr_{12}Fe_{35}Mn_{23}Ni_{20}$) for detailed experimental work under this work package. This work package also investigated an advanced processing route for fabricating functionally graded HEAs using DED and off-the-shelf metal alloy powders. This advanced processing methodology for functionally graded HEAs would open avenues for rapidly assessing new HEA compositions at significantly cheaper costs.

Most of the HEA research used arc (73%) and vacuum (15%) melting processes as a fabrication method, with only 11% of the papers reviewed using laser-based AM processes. Solid-state manufacturing processes were only reported in less than 5% of the instances. The literature survey shows the opportunity to explore solid-phase processes as a manufacturing technique because of the grain refinement and decreased segregation properties during these processes. Therefore, FSLD processing has been performed on the two down-selected HEAs ($Al_{0.3}Ti_{0.2}Co_{0.7}CrFeNi_{1.7}$ and $Al_{10}Cr_{12}Fe_{35}Mn_{23}Ni_{20}$) because of its unique processing conditions, which result in finer microstructures with compositionally homogenous grains that would potentially enhance their mechanical properties. In addition, the effect of solid-phase processing on the mechanical properties of these HEAs can also provide valuable information and potentially more economical routes to HEA adoption to the market. Therefore, it is recommended that depositing a functionally graded alloy onto an HEA as a final coating be explored to determine the impact on the interlayers and interface properties.

The temperature-dependent (from RT to 500°C) nanoindentation behavior of the DED- and SLM-processed $Al_{0.3}Ti_{0.2}Co_{0.7}CrFeNi_{1.7}$ HEA was investigated in the AD and one-step annealed conditions for this study. The hierarchically heterogeneous microstructures obtained via simple one-step annealing of the DED- and SLM-processed HEAs exhibited significantly better performance than the nearly homogeneous microstructures in the AD state. The one-step annealed specimens revealed a less than 6.6% reduction in hardness at 500°C compared to that at RT, while the AD specimens showed a greater than 18% reduction in hardness between RT and 500°C. The one-step annealed specimens also exhibited a significantly higher hardness than the as-deposited specimens owing to their multiphase (FCC+$L1_2$) microstructures with a substantial fraction of ordered $L1_2$ precipitates. Furthermore, serrated yielding (PLC effect) indicative of microstructural instability was observed during nanoindentation deformation (at 500°C) for both SLM- and DED-processed specimens but not after one-step annealing. Overall, the nanoindentation results indicate the stability of these hierarchically heterogeneous microstructures developed via single-step annealing, exploiting the residual stresses in the AM-processed $Al_{0.3}Ti_{0.2}Co_{0.7}CrFeNi_{1.7}$ HEA. Overall, the presented results are promising. However, applying this HEA in high-temperature nuclear reactors would require a more detailed assessment of other properties. This HEA is expected to have high-temperature stability up to ~1100°C.

In contrast, FSLD processing of this HEA was challenging because of its multiphase microstructure in the AR state. Hence, a meticulous process parameter optimization study was performed to process this HEA. Further, detailed microstructural characterization using SEM was carried out to analyze the differences in the microstructure due to FSLD processing. FSLD processing led to the homogenization of this HEA, resulting in the formation of a single-phase FCC microstructure. Despite the single-phase character, the FSLD-processed HEA exhibited a significantly high hardness of 325 HV, providing scope for further enhancement of the hardness via heat treatments and process parameter optimization.

Similar to $Al_{0.3}Ti_{0.2}Co_{0.7}CrFeNi_{1.7}$, cast rods of the $Al_{10}Cr_{12}Fe_{35}Mn_{23}Ni_{20}$ HEA procured from Sophisticated Alloys, Inc., were processed using FSLD to produce single and multilayer deposits of the $Al_{10}Cr_{12}Fe_{35}Mn_{23}Ni_{20}$ HEA. A detailed process parameter–property optimization study was performed by depositing several single layers of the HEA by varying the forging force (*F*) and traverse speed (*Tr*). Further, a multilayer deposit was successfully fabricated using the optimized processing conditions (*F* = 40 kN, *Tr* = 200 mm/min), demonstrating the potential for FSLD to fabricate tall specimens. A detailed microstructural evaluation of the AR and FSLD-processed specimens was carried out using SEM, EBSD, EDS, and TEM. The AR specimen exhibited a coarser triple-phase FCC+BCC+B2 microstructure with a soft FCC matrix phase, a hard BCC dendritic phase, and a harder B2 phase as precipitates within the hard BCC dendrites. Thus, all three phases pursued drastically different microstructural evolution pathways during FSLD processing. The FCC matrix underwent continuous dynamic recrystallization, forming finer equiaxed grains due to shearing deformation. At the same time, the BCC dendrites fractured into several finer fragments, and in some regions, these BCC fragments tended to grow, changing their morphology from arbitrary to hourglass-like. Among the three phases, B2 is the only phase that likely dissolved during processing and reprecipitated as finer precipitates in the BCC fragments during continuous cooling post-FSLD. In a manuscript submitted to *Additive Manufacturing*, these complex mechanisms are clearly illustrated using a schematic. The microstructure of the triple-phase HEA changed significantly with the changes in the processing conditions, providing scope for tuning the process parameters to attain the desired microstructures and mechanical properties. To conclude, in addition to the significant enhancement in the hardness (from 177 HV to 278 HV), FSLD processing led to substantially finer grains/precipitates, which increase the number of interfaces, potentially enhancing the sink strength of the $Al_{10}Cr_{12}Fe_{35}Mn_{23}Ni_{20}$ HEA, making it an ideal candidate for future nuclear applications.

The microstructures of compositionally graded HEAs fabricated via the DED technique using off-the-shelf common alloy powders have been characterized. The results reveal homogenous compositions in each build layer. However, the graded HEAs formed dendritic and interdendritic microstructures mainly because of the presence of heavier elements such as Nb. Few regions contained unmelted 316 L powders with sparsely distributed nanoscale Cr-rich precipitates. Additionally, Ti oxide particles were observed in the HEA matrix. While the microstructural examination indicates the successful fabrication of graded materials, further investigation is needed to optimize the process parameters to reduce porosity and undesired brittle intermetallic phases and ensure complete melting of the metal alloy powders.

Based on the literature review, the preliminary experiments performed, and engineering rationale, a preliminary rating of the two down-selected alloys was performed. The $Al_{10}Cr_{12}Fe_{35}Mn_{23}Ni_{20}$ HEA performed marginally better than the $Al_{0.3}Ti_{0.2}Co_{0.7}CrFeNi_{1.7}$ HEA, with a rating of 63 versus 55.5.

8.0 References

1. E. J. Pickering, A. W. Carruthers, P. J. Barron, S. C. Middleburgh, D. E. J. Armstrong, and A. S. Gandy, Entropy 2021, Vol. 23, Page 98 **23**, 98 (2021).
2. O. El-Atwani, N. Li, M. Li, A. Devaraj, J. K. S. Baldwin, M. M. Schneider, D. Sobieraj, J. S. Wróbel, D. Nguyen-Manh, S. A. Maloy, and E. Martinez, Sci Adv **5**, (2019).
3. A. S. Gandy, B. Jim, G. Coe, D. Patel, L. Hardwick, S. Akhmadaliev, N. Reeves-McLaren, and R. Goodall, Front Mater **6**, (2019).
4. A. Ayyagari, R. Salloom, S. Muskeri, and S. Mukherjee, Materialia (Oxf) **4**, 99 (2018).
5. O. A. Waseem and H. J. Ryu, Sci Rep **7**, (2017).
6. T. Nagase, S. Anada, P. Rack, J. Noh, H. Y.- Intermetallics, 26 (2012) 122–130.
7. T. Nagase, S. Anada, P. Rack, J. Noh, H. Y.- Intermetallics, 38 (2013), 70
8. S. Q. Xia, X. Yang, T. F. Yang, S. Liu, and Y. Zhang, JOM **67**, 2340 (2015).
9. T. Nagase, P. Rack, J. Noh, T. E.- Intermetallics, and undefined 2015, Elsevier (n.d.).
10. S. Xia, W. Zhen, T. Yang, Y. Z.-J. of I. and S. Research, and undefined 2015, Elsevier (n.d.).
11. S. Middleburgh, … D. K.-R. S. open, and undefined 2015, Royalsocietypublishing.Org **2**, (2015).
12. D. J. M. King, P. A. Burr, E. G. Obbard, and S. C. Middleburgh, Journal of Nuclear Materials **488**, 70 (2017).
13. P. Agrawal, S. Gupta, A. Dhal, R. Prabhakaran, L. Shao, and R. S. Mishra, Journal of Nuclear Materials **574**, 154217 (2023).
14. A. Kareer, J. C. Waite, B. Li, A. Couet, D. E. J. Armstrong, and A. J. Wilkinson, Journal of Nuclear Materials **526**, 151744 (2019).
15. B. Kombaiah, Y. Zhou, K. Jin, A. Manzoor, J. D. Poplawsky, J. A. Aguiar, H. Bei, D. S. Aidhy, P. D. Edmondson, and Y. Zhang, ACS Appl Mater Interfaces **15**, 3912 (2023).
16. B. Gwalani, S. Dasari, A. Sharma, V. Soni, S. Shukla, A. Jagetia, P. Agrawal, R. S. Mishra, and R. Banerjee, Acta Mater **219**, 117234 (2021).
17. Y. Zhao, Z. Chen, K. Yan, S. Naseem, W. Le, H. Zhang, and W. Lu, Materials Science and Engineering: A **838**, 142759 (2022).
18. S. Dasari, A. Jagetia, Y. J. Chang, V. Soni, B. Gwalani, S. Gorsse, A. C. Yeh, and R. Banerjee, J Alloys Compd **830**, 154707 (2020).
19. O. Oyelola, P. Crawforth, R. M'Saoubi, and A. T. Clare, Addit Manuf **24**, 20 (2018).
20. V. Chaudhary, N. M. Sai Kiran Kumar Yadav, S. A. Mantri, S. Dasari, A. Jagetia, R. V Ramanujan, and R. Banerjee, J Alloys Compd **823**, 153817 (2020).
21. W. Liu and J. N. DuPont, Scr Mater **48**, 1337 (2003).
22. D. D. Lima, S. A. Mantri, C. V Mikler, R. Contieri, C. J. Yannetta, K. N. Campo, E. S. Lopes, M. J. Styles, T. Borkar, R. Caram, and R. Banerjee, Mater Des **130**, 8 (2017).
23. M. S. K. K. Y. Nartu, A. Jagetia, V. Chaudhary, S. A. Mantri, E. Ivanov, N. B. Dahotre, R. V Ramanujan, and R. Banerjee, Scr Mater **187**, 30 (2020).
24. M. S. K. K. Y. Nartu, T. Alam, S. Dasari, S. A. Mantri, S. Gorsse, H. Siller, N. Dahotre, and R. Banerjee, Materialia (Oxf) **9**, 100522 (2020).
25. V. Chaudhary, M. S. K. K. Y. Nartu, S. Dasari, S. M. Varahabhatla, A. Sharma, M. Radhakrishnan, S. A. Mantri, S. Gorsse, N. B. Dahotre, R. V Ramanujan, and R. Banerjee, Scr Mater **224**, 115149 (2023).
26. M. S. K. K. Y. Nartu, D. Flannery, S. Mazumder, S. A. Mantri, S. S. Joshi, A. V. Ayyagari, B. McWilliams, K. Cho, N. B. Dahotre, and R. Banerjee, JOM 1 (2021).
27. M. S. K. K. Y. Nartu, S. Sharma, S. A. Mantri, S. S. Joshi, M. V. Pantawane, S. Mazumder, N. B. Dahotre, and R. Banerjee, in *Additive Manufacturing in Biomedical Applications* (ASM International, 2022), pp. 130–159.

28. M. S. K. K. Y. Nartu, A. Chesetti, S. Dasari, A. Sharma, S. A. Mantri, N. B. Dahotre, and R. Banerjee, Materials Science and Engineering: A **849**, 143505 (2022).
29. A. Chesetti, S. Banerjee, S. Dasari, S. M. Varahabhatla, A. Sharma, S. A. Mantri, M. S. K. K. Y. Nartu, N. Dahotre, and R. Banerjee, Additive Manufacturing Letters **6**, 100140 (2023).
30. C. Schneider-Maunoury, L. Weiss, P. Acquier, D. Boisselier, and P. Laheurte, Addit Manuf **17**, 55 (2017).
31. A. Gupta and M. Talha, Progress in Aerospace Sciences **79**, 1 (2015).
32. A. Sola, D. Bellucci, and V. Cannillo, Biotechnol Adv **34**, 504 (2016).
33. B. Saleh, J. Jiang, R. Fathi, T. Al-hababi, Q. Xu, L. Wang, D. Song, and A. Ma, Compos B Eng **201**, 108376 (2020).
34. V. Chaudhary, M. S. K. K. Y. Nartu, S. Dasari, S. M. Varahabhatla, A. Sharma, M. Radhakrishnan, S. A. Mantri, S. Gorsse, N. B. Dahotre, R. V. Ramanujan, and R. Banerjee, Scr Mater **224**, 115149 (2023).
35. M. Radhakrishnan, M. McKinstry, V. Chaudhary, M. S. K. K. Y. Nartu, K. V. M. Krishna, R. V. Ramanujan, R. Banerjee, and N. B. Dahotre, Scr Mater **226**, 115269 (2023).
36. X. Li, T. Wang, X. Ma, N. Overman, S. Whalen, D. Herling, and K. Kappagantula, J Manuf Process **80**, 108 (2022).
37. J. W. Yeh, S. K. Chen, S. J. Lin, J. Y. Gan, T. S. Chin, T. T. Shun, C. H. Tsau, and S. Y. Chang, Adv Eng Mater **6**, 299 (2004).
38. B. Gwalani, S. Gorsse, D. Choudhuri, Y. Zheng, R. S. Mishra, and R. Banerjee, Scr Mater **162**, 18 (2019).
39. S. Yadav, S. Sarkar, A. Aggarwal, A. Kumar, and K. Biswas, Wear **410–411**, 93 (2018).
40. K. R. Lim, K. S. Lee, J. S. Lee, J. Y. Kim, H. J. Chang, and Y. S. Na, J Alloys Compd **728**, 1235 (2017).
41. M. A. [Sandia N. Lab. (SNL-N. Melia Albuquerque, NM (United States)], J. D. [Sandia N. Lab. (SNL-N. Carroll Albuquerque, NM (United States)], S. R. [Sandia N. Lab. (SNL-N. Whetten Albuquerque, NM (United States)], S. N. [The O. S. Univ. Esmaeely Columbus, OH (United States)], J. [The O. S. Univ. Locke Columbus, OH (United States)], E. [Ames Lab. and I. S. Univ. White Ames, IA (United States)], I. [Ames Lab. and I. S. Univ. Anderson Ames, IA (United States)], M. [Sandia N. Lab. (SNL-N. Chandross Albuquerque, NM (United States)], J. R. [Sandia N. Lab. (SNL-N. Michael Albuquerque, NM (United States)], N. [Sandia N. Lab. (SNL-N. Argibay Albuquerque, NM (United States)], E. J. [Sandia N. Lab. (SNL-N. Schindelholz Albuquerque, NM (United States)], and A. B. [Sandia N. Lab. (SNL-N. Kustas Albuquerque, NM (United States)], (2019).
42. K. Kuwabara, H. Shiratori, T. Fujieda, K. Yamanaka, Y. Koizumi, and A. Chiba, Addit Manuf **23**, 264 (2018).
43. Y. Fan, Y. Zhang, H. Guan, H. Suo, and L. He, Rare Metal Materials and Engineering **42**, 1127 (2013).
44. V. Shivam, J. Basu, V. K. Pandey, Y. Shadangi, and N. K. Mukhopadhyay, Advanced Powder Technology **29**, 2221 (2018).
45. Z. Fu, W. Chen, H. Wen, Z. Chen, and E. J. Lavernia, J Alloys Compd **646**, 175 (2015).
46. C. Sun, P. Li, S. Xi, Y. Zhou, S. Li, and X. Yang, Materials Science and Engineering: A **728**, 144 (2018).
47. Z. Fu, W. Chen, H. Wen, D. Zhang, Z. Chen, B. Zheng, Y. Zhou, and E. J. Lavernia, Acta Mater **107**, 59 (2016).
48. Z. Tang, O. N. Senkov, C. M. Parish, C. Zhang, F. Zhang, L. J. Santodonato, G. Wang, G. Zhao, F. Yang, and P. K. Liaw, Materials Science and Engineering: A **647**, 229 (2015).
49. S. Mohanty, N. P. Gurao, P. Padaikathan, and K. Biswas, Mater Charact **129**, 127 (2017).
50. A. Emamifar, B. Sadeghi, P. Cavaliere, and H. Ziaei, Https://Doi.Org/10.1080/00325899.2019.1576389 **62**, 61 (2019).

51. N. Eißmann, B. Klöden, T. Weißgärber, and B. Kieback, Https://Doi.Org/10.1080/00325899.2017.1318480 **60**, 184 (2017).
52. A. I. Yurkova, V. V. Cherniavsky, V. Bolbut, M. Krüger, and I. Bogomol, J Alloys Compd **786**, 139 (2019).
53. P. Agrawal, R. S. Haridas, P. Agrawal, and R. S. Mishra, Addit Manuf **60**, 103282 (2022).
54. L. Hou, J. Hui, Y. Yao, J. Chen, and J. Liu, Vacuum **164**, 212 (2019).
55. S. Singh, N. Wanderka, B. S. Murty, U. Glatzel, and J. Banhart, Acta Mater **59**, 182 (2011).
56. Y. Liu, Y. Zhang, H. Zhang, N. Wang, X. Chen, H. Zhang, and Y. Li, J Alloys Compd **694**, 869 (2017).
57. D. G. Kim, Y. H. Jo, J. M. Park, W. M. Choi, H. S. Kim, B. J. Lee, S. S. Sohn, and S. Lee, J Alloys Compd **812**, 152111 (2020).
58. É. Fazakas, J. Q. Wang, V. Zadorozhnyy, D. V. Louzguine-Luzgin, and L. K. Varga, Materials and Corrosion **65**, 691 (2014).
59. Y. Du, Y. Lu, T. Wang, T. Li, and G. Zhang, Procedia Eng **27**, 1129 (2012).
60. Z. Yao, (2016).
61. S. qin Xia, Z. Wang, T. fei Yang, and Y. Zhang, Journal of Iron and Steel Research, International **22**, 879 (2015).
62. S. Q. Xia, X. Yang, T. F. Yang, S. Liu, and Y. Zhang, JOM **67**, 2340 (2015).
63. S. Shen, F. Chen, X. Tang, J. Lin, G. Ge, and J. Liu, Journal of Nuclear Materials **540**, 152380 (2020).
64. S. Xia, M. C. Gao, T. Yang, P. K. Liaw, and Y. Zhang, Journal of Nuclear Materials **480**, 100 (2016).
65. H. Zheng, R. Chen, G. Qin, X. Li, Y. Su, H. Ding, J. Guo, and H. Fu, J Alloys Compd **787**, 1023 (2019).
66. H. Zheng, R. Chen, G. Qin, X. Li, Y. Su, H. Ding, J. Guo, and H. Fu, J Mater Sci Technol **38**, 19 (2020).
67. S. T. Mileiko, S. A. Firstov, N. A. Novokhatskaya, V. F. Gorban, and N. P. Krapivka, Compos Part A Appl Sci Manuf **76**, 131 (2015).
68. Y. Yu, F. He, Z. Qiao, Z. Wang, W. Liu, and J. Yang, J Alloys Compd **775**, 1376 (2019).
69. F. He, Z. Wang, P. Cheng, Q. Wang, J. Li, Y. Dang, J. Wang, and C. T. Liu, J Alloys Compd **656**, 284 (2016).
70. S. Deepak Kumar, J. Ghose, and A. Mandal, Sustainable Engineering Products and Manufacturing Technologies 25 (2019).
71. G. T. Gray, V. Livescu, P. A. Rigg, C. P. Trujillo, C. M. Cady, S. R. Chen, J. S. Carpenter, T. J. Lienert, and S. J. Fensin, Acta Mater **138**, 140 (2017).
72. M. S. K. K. Y. Nartu, S. Dasari, A. Sharma, S. A. Mantri, S. Sharma, M. V. Pantawane, B. McWilliams, K. Cho, N. B. Dahotre, and R. Banerjee, Materials Science and Engineering: A **821**, 141627 (2021).
73. P. Wang, P. Huang, F. L. Ng, W. J. Sin, S. Lu, M. L. S. Nai, Z. L. Dong, and J. Wei, Mater Des **168**, 107576 (2019).
74. V. V. Popov, A. Katz-Demyanetz, A. Koptyug, and M. Bamberger, Heliyon **5**, e01188 (2019).
75. K. Kuwabara, H. Shiratori, T. Fujieda, K. Yamanaka, Y. Koizumi, and A. Chiba, Addit Manuf **23**, 264 (2018).
76. T. Fujieda, H. Shiratori, K. Kuwabara, M. Hirota, T. Kato, K. Yamanaka, Y. Koizumi, A. Chiba, and S. Watanabe, Mater Lett **189**, 148 (2017).
77. R. Li, P. Niu, T. Yuan, P. Cao, C. Chen, and K. Zhou, J Alloys Compd **746**, 125 (2018).
78. D. Lin, L. Xu, H. Jing, Y. Han, L. Zhao, and F. Minami, Addit Manuf **32**, 101058 (2020).
79. S. Luo, P. Gao, H. Yu, J. Yang, Z. Wang, and X. Zeng, J Alloys Compd **771**, 387 (2019).
80. X. Zhang, Y. Tong, Y. Hu, X. Liang, Y. Chen, K. Wang, M. Zhang, and J. Xu, Lubricants 2022, Vol. 10, Page 344 **10**, 344 (2022).

81. Md. R. U. Ahsan, G.-J. Seo, X. Fan, P. K. Liaw, S. Motaman, C. Haase, and D. B. Kim, J Manuf Process **68**, 1314 (2021).
82. K. A. Osintsev, S. V. Konovalov, V. E. Gromov, Y. F. Ivanov, and I. A. Panchenko, Mater Lett **312**, 131675 (2022).
83. D. K. Misra, C. Shang, T. Niendorf, K. Osintsev, S. Konovalov, D. Zaguliaev, Y. Ivanov, V. Gromov, and I. Panchenko, Metals 2022, Vol. 12, Page 197 **12**, 197 (2022).
84. C. S. Wu, P. H. Tsai, C. M. Kuo, and C. W. Tsai, Entropy 2018, Vol. 20, Page 967 **20**, 967 (2018).
85. P. Singh, A. Marshal, A. V. Smirnov, A. Sharma, G. Balasubramanian, K. G. Pradeep, and D. D. Johnson, Phys Rev Mater **3**, 075002 (2019).
86. S. M. Na, P. K. Lambert, H. Kim, J. Paglione, and N. J. Jones, AIP Adv **9**, 35010 (2019).
87. J. C. Rao, H. Y. Diao, V. Ocelík, D. Vainchtein, C. Zhang, C. Kuo, Z. Tang, W. Guo, J. D. Poplawsky, Y. Zhou, P. K. Liaw, and J. T. M. De Hosson, Acta Mater **131**, 206 (2017).
88. H. Y. Yasuda, K. Shigeno, and T. Nagase, Scr Mater **108**, 80 (2015).
89. F. Peyrouzet, D. Hachet, R. Soulas, C. Navone, S. Godet, and S. Gorsse, JOM **71**, 3443 (2019).
90. S. Dasari, A. Jagetia, Y. J. Chang, V. Soni, B. Gwalani, S. Gorsse, A. C. Yeh, and R. Banerjee, J Alloys Compd **830**, 154707 (2020).
91. L. Liu, P. Lazor, and X. Li, Https://Doi.Org/10.1080/08957959.2019.1653865 **39**, 533 (2019).
92. M. V. Karpets, O. S. Makarenko, V. F. Gorban', M. O. Krapivka, O. A. Rokitska, and S. Y. Makarenko, Powder Metallurgy and Metal Ceramics **55**, 361 (2016).
93. N. Zhou, S. Jiang, T. Huang, M. Qin, T. Hu, and J. Luo, Sci Bull (Beijing) **64**, 856 (2019).
94. P. K. Sarswat, S. Sarkar, A. Murali, W. Huang, W. Tan, and M. L. Free, Appl Surf Sci **476**, 242 (2019).
95. Z. Wang, I. Baker, Z. Cai, S. Chen, J. D. Poplawsky, and W. Guo, Acta Mater **120**, 228 (2016).
96. N. Liu, C. Chen, I. Chang, P. Zhou, and X. Wang, Materials 2018, Vol. 11, Page 1290 **11**, 1290 (2018).
97. P. Singh, A. Marshal, A. V. Smirnov, A. Sharma, G. Balasubramanian, K. G. Pradeep, and D. D. Johnson, Phys Rev Mater **3**, 075002 (2019).
98. P. Asghari-Rad, P. Sathiyamoorthi, J. W. Bae, J. Moon, J. M. Park, A. Zargaran, and H. S. Kim, Materials Science and Engineering: A **744**, 610 (2019).
99. Q. Ding, Y. Zhang, X. Chen, X. Fu, D. Chen, S. Chen, L. Gu, F. Wei, H. Bei, Y. Gao, M. Wen, J. Li, Z. Zhang, T. Zhu, R. O. Ritchie, and Q. Yu, Nature 2019 574:7777 **574**, 223 (2019).
100. K. Guruvidyathri, B. S. Murty, J. W. Yeh, and K. C. Hari Kumar, J Alloys Compd **768**, 358 (2018).
101. D. G. Kim, Y. H. Jo, J. M. Park, W. M. Choi, H. S. Kim, B. J. Lee, S. S. Sohn, and S. Lee, J Alloys Compd **812**, 152111 (2020).
102. Z. Wu, H. Bei, F. Otto, G. M. Pharr, and E. P. George, Intermetallics (Barking) **46**, 131 (2014).
103. S. Sohn, Y. Liu, J. Liu, P. Gong, S. Prades-Rodel, A. Blatter, B. E. Scanley, C. C. Broadbridge, and J. Schroers, Scr Mater **126**, 29 (2017).
104. T. Nagase, A. Shibata, M. Matsumuro, M. Takemura, and S. Semboshi, Mater Des **181**, 107900 (2019).
105. K. Sarlar, A. Tekgül, and I. Kucuk, Current Applied Physics **20**, 18 (2020).
106. S. Gou, M. Gao, Y. Shi, S. Li, Y. Fang, X. Chen, H. Chen, W. Yin, J. Liu, Z. Lei, and H. Wang, Acta Mater **248**, 118781 (2023).
107. V. T. Nguyen, M. Qian, Z. Shi, T. Song, L. Huang, and J. Zou, Materials Science and Engineering: A **742**, 762 (2019).
108. Y. Yuan, Y. Wu, X. Tong, H. Zhang, H. Wang, X. J. Liu, L. Ma, H. L. Suo, and Z. P. Lu, Acta Mater **125**, 481 (2017).

109. J. W. Qiao, M. L. Bao, Y. J. Zhao, H. J. Yang, Y. C. Wu, Y. Zhang, J. A. Hawk, and M. C. Gao, J Appl Phys **124**, 195101 (2018).
110. M. Feuerbacher, M. Heidelmann, and C. Thomas, Http://Mc.Manuscriptcentral.Com/Tmrl **3**, 1 (2015).
111. A. Takeuchi, K. Amiya, T. Wada, K. Yubuta, and W. Zhang, JOM **66**, 1984 (2014).
112. J. W. Qiao, M. L. Bao, Y. J. Zhao, H. J. Yang, Y. C. Wu, Y. Zhang, J. A. Hawk, and M. C. Gao, J Appl Phys **124**, 195101 (2018).
113. Y. J. Zhao, J. W. Qiao, S. G. Ma, M. C. Gao, H. J. Yang, M. W. Chen, and Y. Zhang, Mater Des **96**, 10 (2016).
114. S. Y. Chen, X. Yang, K. A. Dahmen, P. K. Liaw, and Y. Zhang, Entropy 2014, Vol. 16, Pages 870-884 **16**, 870 (2014).
115. O. N. Senkov, S. V. Senkova, and C. Woodward, Acta Mater **68**, 214 (2014).
116. D. D. Zhang, J. Y. Zhang, J. Kuang, G. Liu, and J. Sun, Acta Mater **220**, 117288 (2021).
117. O. N. Senkov, S. V. Senkova, D. B. Miracle, and C. Woodward, Materials Science and Engineering: A **565**, 51 (2013).
118. H. Chen, A. Kauffmann, S. Seils, T. Boll, C. H. Liebscher, I. Harding, K. S. Kumar, D. V. Szabó, S. Schlabach, S. Kauffmann-Weiss, F. Müller, B. Gorr, H. J. Christ, and M. Heilmaier, Acta Mater **176**, 123 (2019).
119. Y. Wu, J. Si, D. Lin, T. Wang, W. Y. Wang, Y. Wang, Z. K. Liu, and X. Hui, Materials Science and Engineering: A **724**, 249 (2018).
120. O. N. Senkov, C. Woodward, and D. B. Miracle, JOM **66**, 2030 (2014).
121. P. Lu, J. E. Saal, G. B. Olson, T. Li, O. J. Swanson, G. S. Frankel, A. Y. Gerard, K. F. Quiambao, and J. R. Scully, Scr Mater **153**, 19 (2018).
122. A. Raturi, J. Aditya C, N. P. Gurao, and K. Biswas, J Alloys Compd **806**, 587 (2019).
123. Y. Lu, H. Huang, X. Gao, C. Ren, J. Gao, H. Zhang, S. Zheng, Q. Jin, Y. Zhao, C. Lu, T. Wang, and T. Li, J Mater Sci Technol **35**, 369 (2019).
124. S. Marik, K. Motla, M. Varghese, K. P. Sajilesh, D. Singh, Y. Breard, P. Boullay, and R. P. Singh, Phys Rev Mater **3**, 060602 (2019).
125. S. Marik, M. Varghese, K. P. Sajilesh, D. Singh, and R. P. Singh, J Alloys Compd **769**, 1059 (2018).
126. Y. S. Lee and R. J. Cava, Physica C: Superconductivity and Its Applications **566**, 1353520 (2019).
127. J. Moon, J. M. Park, J. W. Bae, H. S. Do, B. J. Lee, and H. S. Kim, Acta Mater **193**, 71 (2020).
128. S. Son, J. Moon, H. Kwon, P. Asghari Rad, H. Kato, and H. S. Kim, Metals 2021, Vol. 11, Page 238 **11**, 238 (2021).
129. K. B. Zhang, Z. Y. Fu, J. Y. Zhang, J. Shi, W. M. Wang, H. Wang, Y. C. Wang, and Q. J. Zhang, J Alloys Compd **502**, 295 (2010).
130. M. H. Tsai, H. Yuan, G. Cheng, W. Xu, W. W. Jian, M. H. Chuang, C. C. Juan, A. C. Yeh, S. J. Lin, and Y. Zhu, Intermetallics (Barking) **33**, 81 (2013).
131. E. Jumaev, S. H. Hong, J. T. Kim, H. J. Park, Y. S. Kim, S. C. Mun, J. Y. Park, G. Song, J. K. Lee, B. H. Min, T. Lee, and K. B. Kim, J Alloys Compd **777**, 828 (2019).
132. P. Edalati, A. Mohammadi, M. Ketabchi, and K. Edalati, J Alloys Compd **884**, 161101 (2021).
133. K. Baba, N. Ishizu, T. Nishizaki, and J. Kitagawa, Materials 2021, Vol. 14, Page 2877 **14**, 2877 (2021).
134. Z. Tang, T. Yuan, C. W. Tsai, J. W. Yeh, C. D. Lundin, and P. K. Liaw, Acta Mater **99**, 247 (2015).
135. Z. Li and D. Raabe, Mater Chem Phys **210**, 29 (2018).
136. Q. Wang, L. Zeng, T. Gao, H. Du, and X. Liu, J Mater Sci Technol **87**, 29 (2021).

137. H. Ren, R. R. Chen, X. F. Gao, T. Liu, G. Qin, S. P. Wu, and J. J. Guo, J Alloys Compd **929**, 167374 (2022).
138. C. W. Lu, Y. S. Lu, Z. H. Lai, H. W. Yen, and Y. L. Lee, J Alloys Compd **842**, 155824 (2020).
139. S. Shuang, Y. Liang, C. Yu, al -, C. Huang, Y. Yao, and X. Peng, J Electrochem Soc **167**, 081506 (2020).
140. G. Perumal, H. S. Grewal, M. Pole, L. V. K. Reddy, S. Mukherjee, H. Singh, G. Manivasagam, and H. S. Arora, ACS Appl Bio Mater **3**, 1233 (2020).
141. Y. P. Cai, G. J. Wang, Y. J. Ma, Z. H. Cao, and X. K. Meng, Scr Mater **162**, 281 (2019).
142. P. Cui, Z. Bao, Y. Liu, F. Zhou, Z. Lai, Y. Zhou, and J. Zhu, Corros Sci **201**, 110276 (2022).
143. S. Xia, Z. Xia, D. Zhao, Y. Xie, X. Liu, and L. Wang, Fusion Engineering and Design **172**, 112792 (2021).
144. P. Edalati, A. Mohammadi, M. Ketabchi, and K. Edalati, J Alloys Compd **894**, 162413 (2022).
145. S. Sun, H. Liu, J. Hao, and H. Yang, J Alloys Compd **886**, 161251 (2021).
146. K. Patel, V. Hasannaeimi, M. Sadeghilaridjani, S. Muskeri, C. Mahajan, and S. Mukherjee, Entropy 2023, Vol. 25, Page 296 **25**, 296 (2023).
147. Y. Liu, J. Tu, C. hao Wang, J. ru Luo, L. peng Ding, P. huai Wang, and Z. ming Zhou, J Alloys Compd **858**, 157642 (2021).
148. P. Fu, H. Su, Z. Li, P. Dai, and Q. Tang, J Alloys Compd **921**, 166141 (2022).
149. S. S. Nene, K. Liu, S. Sinha, M. Frank, S. Williams, and R. S. Mishra, Materialia (Oxf) **9**, 100521 (2020).
150. S. Luo, C. Zhao, Y. Su, Q. Liu, and Z. Wang, Addit Manuf **31**, 100925 (2020).
151. L. Gu, N. Liang, Y. Liu, Y. Chen, J. Liu, Y. Sun, and Y. Zhao, Mater Lett **324**, 132676 (2022).
152. D. G. Shaysultanov, G. A. Salishchev, Y. V. Ivanisenko, S. V. Zherebtsov, M. A. Tikhonovsky, and N. D. Stepanov, J Alloys Compd **705**, 756 (2017).
153. H. Ren, R. R. Chen, X. F. Gao, T. Liu, G. Qin, S. P. Wu, and J. J. Guo, Materials Science and Engineering: A **862**, 144425 (2023).
154. O. N. Senkov, C. Woodward, and D. B. Miracle, JOM **66**, 2030 (2014).
155. B. Gwalani, S. Dasari, A. Sharma, V. Soni, S. Shukla, A. Jagetia, P. Agrawal, R. S. Mishra, and R. Banerjee, Acta Mater **219**, 117234 (2021).
156. A. Chesetti, S. Banerjee, S. Dasari, M. S. K. Nartu, S. M. Varahabhatla, A. Sharma, A. Ramakrishnan, D. Satko, S. Gorsse, A. Salem, and R. Banerjee, Scr Mater **225**, 115160 (2023).
157. K. Ming, X. Bi, and J. Wang, Int J Plast **100**, 177 (2018).
158. S. G. Ma and Y. Zhang, Materials Science and Engineering: A **532**, 480 (2012).
159. S. Dasari, A. Jagetia, Y. J. Chang, V. Soni, B. Gwalani, S. Gorsse, A. C. Yeh, and R. Banerjee, J Alloys Compd **830**, 154707 (2020).
160. S. Shukla, D. Choudhuri, T. Wang, K. Liu, R. Wheeler, S. Williams, B. Gwalani, and R. S. Mishra, Mater Res Lett **6**, 676 (2018).
161. Y. L. Zhao, T. Yang, Y. R. Li, L. Fan, B. Han, Z. B. Jiao, D. Chen, C. T. Liu, and J. J. Kai, Acta Mater **188**, 517 (2020).
162. K. Zhang, H. Wen, B. Zhao, X. Dong, and L. Zhang, Mater Charact **155**, 109792 (2019).
163. J. Peng, Z. Li, L. Fu, X. Ji, Z. Pang, and A. Shan, J Alloys Compd **803**, 491 (2019).
164. N. Gao, D. H. Lu, Y. Y. Zhao, X. W. Liu, G. H. Liu, Y. Wu, G. Liu, Z. T. Fan, Z. P. Lu, and E. P. George, J Alloys Compd **792**, 1028 (2019).
165. H. Cheng, W. Chen, X. Liu, Q. Tang, Y. Xie, and P. Dai, Materials Science and Engineering: A **719**, 192 (2018).
166. J. Chen, Z. Yao, X. Wang, Y. Lu, X. Wang, Y. Liu, and X. Fan, Mater Chem Phys **210**, 136 (2018).

167. L. B. Chen, R. Wei, K. Tang, J. Zhang, F. Jiang, L. He, and J. Sun, Materials Science and Engineering: A **716**, 150 (2018).
168. J. Y. Ko and S. I. Hong, J Alloys Compd **743**, 115 (2018).
169. Z. Li, Acta Mater **164**, 400 (2019).
170. L. Guo, X. Ou, S. Ni, Y. Liu, and M. Song, Materials Science and Engineering: A **746**, 356 (2019).
171. Z. Wang, I. Baker, W. Guo, and J. D. Poplawsky, Acta Mater **126**, 346 (2017).
172. Y. Ma, X. Liu, W. Dong, R. Li, Y. Zhang, Y. Lu, P. Yu, and G. Li, Materials Science and Engineering: A **792**, 139802 (2020).
173. R. Li, D. Kong, K. He, and C. Dong, Scr Mater **230**, 115401 (2023).
174. Y. L. Wang, L. Zhao, D. Wan, S. Guan, and K. C. Chan, Materials Science and Engineering: A **825**, 141871 (2021).
175. T. Fujieda, M. Chen, H. Shiratori, K. Kuwabara, K. Yamanaka, Y. Koizumi, A. Chiba, and S. Watanabe, Addit Manuf **25**, 412 (2019).
176. S. Gou, M. Gao, Y. Shi, S. Li, Y. Fang, X. Chen, H. Chen, W. Yin, J. Liu, Z. Lei, and H. Wang, Acta Mater **248**, 118781 (2023).
177. Y. K. Kim, K. Ram Lim, and K. A. Lee, Mater Des **227**, 111761 (2023).
178. T. M. Smith, C. A. Kantzos, N. A. Zarkevich, B. J. Harder, M. Heczko, P. R. Gradl, A. C. Thompson, M. J. Mills, T. P. Gabb, and J. W. Lawson, Nature 2023 617:7961 **617**, 513 (2023).
179. T. M. Smith, A. C. Thompson, T. P. Gabb, C. L. Bowman, and C. A. Kantzos, Scientific Reports 2020 10:1 **10**, 1 (2020).
180. J. Su, D. Raabe, and Z. Li, Acta Mater **163**, 40 (2019).
181. D. Wei, X. Li, J. Jiang, W. Heng, Y. Koizumi, W. M. Choi, B. J. Lee, H. S. Kim, H. Kato, and A. Chiba, Scr Mater **165**, 39 (2019).
182. Z. Yang, D. Yan, W. Lu, and Z. Li, Materials Science and Engineering: A **801**, 140441 (2021).
183. X. Wu, D. Mayweg, D. Ponge, and Z. Li, Materials Science and Engineering: A **802**, 140661 (2021).
184. R. Wei, K. Zhang, L. Chen, Z. Han, T. Wang, C. Chen, J. Jiang, T. Hu, and F. Li, J Mater Sci Technol **57**, 153 (2020).
185. D. D. Zhang, J. Y. Zhang, J. Kuang, G. Liu, and J. Sun, Acta Mater **220**, 117288 (2021).
186. Z. Li, C. C. Tasan, K. G. Pradeep, and D. Raabe, Acta Mater **131**, 323 (2017).
187. S. Chen, H. S. Oh, B. Gludovatz, S. J. Kim, E. S. Park, Z. Zhang, R. O. Ritchie, and Q. Yu, Nature Communications 2020 11:1 **11**, 1 (2020).
188. Y. Jung, K. Lee, S. J. Hong, J. K. Lee, J. Han, K. B. Kim, P. K. Liaw, C. Lee, and G. Song, J Alloys Compd **886**, 161187 (2021).
189. S. Lee, G. Choi, and K. Lee, Int J Refract Metals Hard Mater **100**, 105628 (2021).
190. L. Lilensten, J. P. Couzinié, J. Bourgon, L. Perrière, G. Dirras, F. Prima, and I. Guillot, Mater Res Lett **5**, 110 (2017).
191. L. Wang, C. Fu, Y. Wu, Q. Wang, X. Hui, and Y. Wang, Materials Science and Engineering: A **748**, 441 (2019).
192. V. T. Nguyen, M. Qian, Z. Shi, T. Song, L. Huang, and J. Zou, Materials Science and Engineering: A **742**, 762 (2019).
193. L. Wang, C. Fu, Y. Wu, R. Li, Y. Wang, and X. Hui, Materials Science and Engineering: A **763**, 138147 (2019).
194. P. Agrawal, S. Gupta, A. Dhal, R. Prabhakaran, L. Shao, and R. S. Mishra, Journal of Nuclear Materials **574**, 154217 (2023).
195. X. Xian, Z. Zhong, B. Zhang, K. Song, C. Chen, S. Wang, J. Cheng, and Y. Wu, Mater Des **121**, 229 (2017).
196. O. A. Waseem and H. J. Ryu, Scientific Reports 2017 7:1 **7**, 1 (2017).

197. A. Kareer, J. C. Waite, B. Li, A. Couet, D. E. J. Armstrong, and A. J. Wilkinson, Journal of Nuclear Materials **526**, 151744 (2019).
198. F. Granberg, K. Nordlund, M. W. Ullah, K. Jin, C. Lu, H. Bei, L. M. Wang, F. Djurabekova, W. J. Weber, and Y. Zhang, Phys Rev Lett **116**, 135504 (2016).
199. S. Q. Xia, X. Yang, T. F. Yang, S. Liu, and Y. Zhang, JOM **67**, 2340 (2015).
200. T. Egami, W. Guo, P. D. Rack, and T. Nagase, Metall Mater Trans A Phys Metall Mater Sci **45**, 180 (2014).
201. M. Sadeghilaridjani, A. Ayyagari, S. Muskeri, V. Hasannaeimi, R. Salloom, W. Y. Chen, and S. Mukherjee, Journal of Nuclear Materials **529**, 151955 (2020).
202. O. El-Atwani, N. Li, M. Li, A. Devaraj, J. K. S. Baldwin, M. M. Schneider, D. Sobieraj, J. S. Wróbel, D. Nguyen-Manh, S. A. Maloy, and E. Martinez, Sci Adv **5**, (2019).
203. R. Li, D. Kong, K. He, and C. Dong, Scr Mater **230**, 115401 (2023).
204. D. J. M. King, S. T. Y. Cheung, S. A. Humphry-Baker, C. Parkin, A. Couet, M. B. Cortie, G. R. Lumpkin, S. C. Middleburgh, and A. J. Knowles, Acta Mater **166**, 435 (2019).
205. C. Xiang, E. H. Han, Z. M. Zhang, H. M. Fu, J. Q. Wang, H. F. Zhang, and G. D. Hu, Intermetallics (Barking) **104**, 143 (2019).
206. Y. Lu, H. Huang, X. Gao, C. Ren, J. Gao, H. Zhang, S. Zheng, Q. Jin, Y. Zhao, C. Lu, T. Wang, and T. Li, J Mater Sci Technol **35**, 369 (2019).
207. Y. Zong, N. Hashimoto, and H. Oka, Nuclear Materials and Energy **31**, 101158 (2022).
208. C. Xiang, H. M. Fu, Z. M. Zhang, E. H. Han, H. F. Zhang, J. Q. Wang, and G. D. Hu, J Alloys Compd **818**, 153352 (2020).
209. D. Li, Y. Dong, Z. Zhang, Q. Zhang, S. Chen, N. Jia, H. Wang, B. Wang, K. Jin, Y. Xue, Y. Dou, X. He, W. Yang, L. Wang, and H. Cai, J Alloys Compd **877**, 160199 (2021).
210. K. K. Tseng, Y. C. Yang, C. C. Juan, T. S. Chin, C. W. Tsai, and J. W. Yeh, Sci China Technol Sci **61**, 184 (2018).
211. O. El Atwani, H. T. Vo, M. A. Tunes, C. Lee, A. Alvarado, N. Krienke, J. D. Poplawsky, A. A. Kohnert, J. Gigax, W. Y. Chen, M. Li, Y. Q. Wang, J. S. Wróbel, D. Nguyen-Manh, J. K. S. Baldwin, O. U. Tukac, E. Aydogan, S. Fensin, and E. Martinez, Nature Communications 2023 14:1 **14**, 1 (2023).
212. Y. Ma, Y. Zhang, Z. Zhang, L. Liu, and L. Sun, Intermetallics (Barking) **157**, 107872 (2023).
213. Y. Wang, S. Li, F. Chen, K. Yang, G. Ge, X. Tang, M. Fan, and P. Huang, J Alloys Compd **958**, 170373 (2023).
214. R. Martins, J. B. Correia, P. Czarkowski, R. Miklaszewski, A. Malaquias, R. Mateus, E. Alves, and M. Dias, Nucl Instrum Methods Phys Res B **538**, 212 (2023).
215. A. Hussain, S. A. Khan, S. K. Sharma, K. Sudarshan, S. K. Sharma, C. Singh, and P. K. Kulriya, Materials Science and Engineering: A **863**, 144523 (2023).
216. M. A. Tunes, S. Fritze, B. Osinger, P. Willenshofer, A. M. Alvarado, E. Martinez, A. S. Menon, P. Ström, G. Greaves, E. Lewin, U. Jansson, S. Pogatscher, T. A. Saleh, V. M. Vishnyakov, and O. El-Atwani, Acta Mater **250**, 118856 (2023).
217. J. Liu, X. An, J. Zhang, Q. Kong, Q. Li, H. Wang, W. Yao, and Q. Wang, Intermetallics (Barking) **153**, 107775 (2023).
218. O. N. Senkov, G. B. Wilks, J. M. Scott, and D. B. Miracle, Intermetallics (Barking) **19**, 698 (2011).
219. M. S. K. K. Y. Nartu, A. Chesetti, S. Dasari, A. Sharma, S. A. Mantri, N. B. Dahotre, and R. Banerjee, Materials Science and Engineering A **849**, (2022).
220. Mohan Sai Kiran Kumar Yadav Nartu, Shristy Jha, Advika Chesetti, Sundeep Mukherjee, Isabella Van Rooyen, and Rajarshi Banerjee, JOM (2023).
221. V. Kumar, A. Gupta, D. Lahiri, and K. Balani, J Phys D Appl Phys **46**, (2013).
222. C. A. Schuh, Materials Today **9**, 32 (2006).
223. J. Il Jang, M. J. Lance, S. Wen, T. Y. Tsui, and G. M. Pharr, Acta Mater **53**, 1759 (2005).
224. S. Banerjee and U. M. Naik, Acta Mater **44**, 3667 (1996).

225. D. Choudhuri, S. A. Mantri, T. Alam, S. Banerjee, and R. Banerjee, Scr Mater **124**, 15 (2016).
226. C. Downey, Development of Advanced Coating Technologies Using Powder-Blown Directed Energy Deposition (DED) Additive Manufacturing for Advanced Nuclear Reactor Applications, Master's Thesis, University of Idaho, 2023.
227. C. Downey, L. Nunez, J. Toman, M. Abdo, and I.J. van Rooyen TMS 2023 Conference Presentation, (2023).
228. C. Downey, I.J. Van Rooyen, L. Nunez - US Patent App. 18/069,023, 2023.

Pacific Northwest National Laboratory

902 Battelle Boulevard
P.O. Box 999
Richland, WA 99354
1-888-375-PNNL (7665)

www.pnnl.gov